Chem Soc Rev

REVIEW ARTICLE

View Article Online
View Journal | View Issue

Cite this: *Chem. Soc. Rev.*, 2025, **54**, 4531

Gains and losses in zinc-ion batteries by proton- and water-assisted reactions

Yauhen Aniskevich and Seung-Taek Myung *

Research on aqueous zinc-ion batteries (AZIBs) has expanded significantly over the last decade due to their promising performance, cost, and safety as well as environmentally friendly features. The use of aqueous electrolytes enables promising AZIB properties while simultaneously introducing undesired reactions and processes. This review focuses on fundamental and critical considerations of water-related equilibria and reactions in zinc-ion batteries. First, we examine Zn^{2+}/water ionic equilibria and their consequences for the chemistry of electrodes. Then, we focus on the mechanisms and kinetics of proton and Zn^{2+} insertion in host frameworks. Next, special attention is given to the water-related dissolution, deposition, and amorphization phenomena of transition-metal-based cathode materials. Finally, we highlight the role of water- and proton-assisted reactions through a systematic comparison of aqueous and nonaqueous zinc-ion batteries.

Received 29th October 2024

DOI: 10.1039/d4cs00810c

rsc.li/chem-soc-rev

1. Introduction

Rechargeable batteries are an essential part of modern society due to their applications in diverse areas, such as portable electronic devices, grid applications, and electric vehicles, which particularly require safety enhancement.[1,2] One of the core technologies is lithium-ion batteries (LIBs) as they offer high volumetric and gravimetric capacity and acceptable cyclability, although unexpected thermal runaway can lead to serious safety concerns. The limited reserves of resources such as lithium, nickel, and cobalt and the refining of these ores have raised several concerns in terms of sustainability and environmental issues. These difficulties have motivated researchers to explore alternative energy storage devices beyond lithium-based systems.[3–5]

Several post-lithium batteries have been introduced by adopting monovalent Na-ion,[6–8] K-ion,[9,10] or multivalent charge carriers,[5,11–13] such as Mg-ion,[14] Ca-ion,[15] Al-ion,[16] and Zn-ion batteries.[17–19] Monovalent systems may be paired with high-capacity carbon-based anode materials, typically hard carbon anodes.[20,21] Notably, multivalent metal-ion batteries mostly use metal anodes, which theoretically offer high volumetric capacities of the corresponding metals, providing an additional merit over safety (Fig. 1a).

Hybrid Materials Research Center, Department of Nanotechnology and Advanced Materials Engineering & Sejong Battery Institute, Sejong University, Seoul 05006, South Korea. E-mail: smyung@sejong.ac.kr

Yauhen Aniskevich

Yauhen Aniskevich earned his PhD in physical chemistry from Belarusian State University in Minsk, Belarus, in 2021. He is currently a postdoctoral researcher at the Department of Nano-engineering at Sejong University, South Korea. His research interests mainly focus on the study and development of post-lithium energy storage systems, including Na– and Zn-ion batteries, with an emphasis on electrode kinetics.

Seung-Taek Myung

Seung-Taek Myung is a DaeYang Distinguished Professor in the Department of Nanotechnology and Advanced Materials Engineering at Sejong University, South Korea. Before 2011, he was affiliated with VK (principal engineer), 3M (seinor engineer), and Iwate University (assistant professor). He received his PhD degree in Chemical Engineering from Iwate University, Japan, in 2003. His research focuses on electro-active materials and the corrosion of metallic current collectors for rechargeable Li-, Na-, K, and Zn-ion batteries.

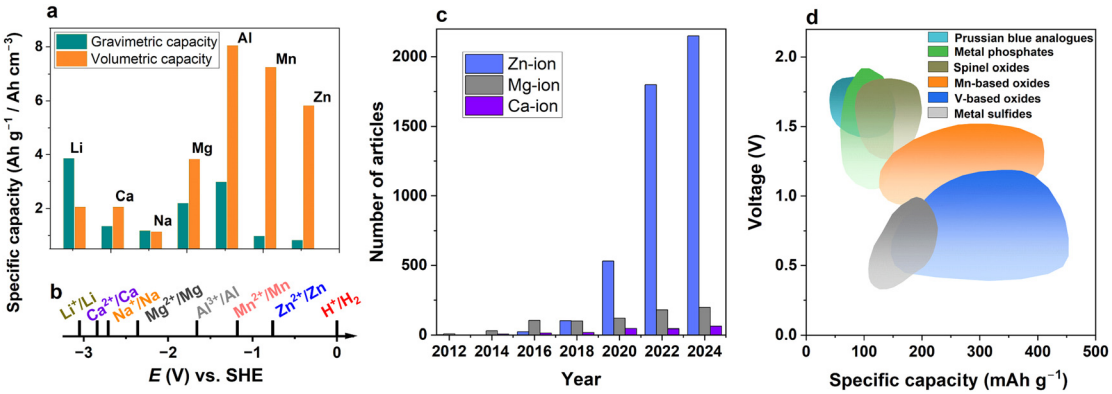

Fig. 1 Comparison of several ion storage systems. (a) Volumetric and gravimetric specific capacities of lithium, sodium, and some multivalent metals. (b) Standard reduction potentials of ions to corresponding metals. (c) Number of articles mentioning multivalent-ion battery in title, and (d) operation voltage *vs.* specific capacity for Zn-ion batteries.[18,22,23]

When comparing divalent metals, the standard potentials for Ca^{2+}/Ca and Mg^{2+}/Mg are relatively low (−2.84 V and −2.36 V *vs.* SHE respectively), indicating the viability of these systems for high-voltage applications (Fig. 1b). The standard potential of Zn^{2+} reduction is comparatively much higher (−0.76 V); hence, zinc-ion batteries (ZIBs) cannot compete with Ca-ion and Mg-ion batteries for high-voltage applications. In addition, these divalent ion reactions have sluggish kinetics in nonaqueous batteries.

However, the use of water-based electrolytes can mitigate these drawbacks for Zn batteries. Namely, the sluggish reaction becomes faster, and the Zn-metal electrode can be operated near the stability window of the electrolyte, where the pH values of electrolytes range from neutral to slightly acidic. This environment is not available for highly reactive calcium and magnesium metals. Thus, the chemical stability of zinc metals in aqueous solution allows the use of inexpensive water-soluble salts for the investigation of aqueous ZIBs (AZIBs). This explains the recent surge in research on AZIBs compared to the mentioned Ca-ion and Mg-ion systems (Fig. 1c). The achievement of high capacity is thought to be another reason that attracts interest in AZIBs (Fig. 1d). Therefore, AZIBs have a significant advantage over other divalent systems in aqueous solutions due to the participation of water in the electrochemical process.

The history of Zn-ion and Zn-metal batteries dates back to the 19th century with the invention of the Leclanché cell, a primary Zn|MnO_2 cell utilizing an ammonium chloride electrolyte (Fig. 2). This work and the subsequent development of alkaline-electrolyte-based cells have met the primary battery demand over the last century. The desire to design a system with similar affordable electrodes in a secondary, rechargeable manner is unsurprising. The first publication on MnO_2-based Zn-metal rechargeable non-alkaline batteries was the 1986 work by Yamamoto and Shoji which reported cyclability of up to 30 cycles in an aqueous $ZnSO_4$ solution.[24] A year later, in a pioneering work by Gocke and colleagues, the intercalation of Zn^{2+} was demonstrated in Chevrel

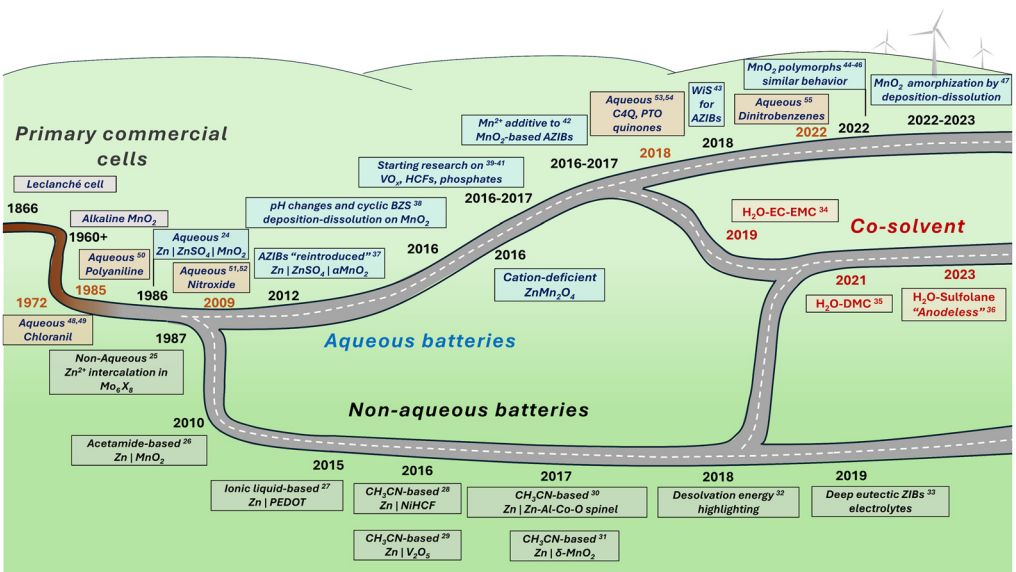

Fig. 2 History of research on zinc-ion batteries, including aqueous and non-aqueous systems.[24–55]

phases from a nonaqueous electrolyte.[25] Since then, only a few articles on ZIBs or Zn-intercalation were published until the 2010s, when research on ZIBs boomed, with the dominance of aqueous systems (Fig. 2).[26–55] Besides pure aqueous and nonaqueous ZIBs, mixed electrolytes have been used in recent years to achieve an appropriate balance between the fast kinetics and stability issues caused by water-related reactions. In addition, research on the redox reactions of organic compounds in Zn^{2+} electrolytes has been conducted since at least 1972, when the voltammetry of tetrachloro-1,4-benzoquinone (chloranil) was evaluated in aqueous $ZnCl_2$ along with calculations of theoretical energy density of the corresponding secondary battery.[48,49] After some time, studies on polyaniline[50] and nitroxide-containing polymers[51,52] emerged. As interest in zinc batteries grew, the search for new stable organic electrodes gained momentum. Notable examples include calix[4]quinone (C4Q)[53] and pyrene-4,5,9,10-tetraone (PTO),[54] along with many other oxygen- and nitrogen-based compounds, which offer promising properties for both stationary and miniaturized energy storage solutions.[55–57] As the number of ZIB studies has reached the thousands, it is difficult to discuss all achievements in a brief history note; other historical perspectives can be found in ZIB-related reviews elsewhere.[18,23]

The associated chemistry of AZIBs has often been considered as the classical rocking chair transport of Zn^{2+} ions between the anode (negative electrode) and cathode (positive host), often underestimating the role of water and its protolytic reactions, which can completely change the mechanism in comparison with non-aqueous batteries.[5,11,17,23,58] The paradigm has changed over the last few years. It is now clear that water-based electrochemical reactions are involved in the main process for charge compensation in various materials in AZIBs.[59,60] Recent literature and reviews explain the ambiguous role of H^+ in mildly acidic aqueous electrolytes during electrochemical reactions. Under certain conditions, the formation of H^+ is not favorable because the active material can be locally damaged by the generation and propagation of H^+, which results in a local acidic environment at the interface between the cathode and electrolyte.[58] Water reduction at Zn results in H_2 gas formation, which can in turn cause an explosion in the hermetically sealed cell, threatening the safety of AZIBs.[61,62] Nevertheless, the insertion of H^+ provided from Zn^{2+} aqueous equilibria boosts the capacity and kinetics of aqueous zinc cells.[63] This implies that the charge carrier Zn^{2+} is often not the main species contributing to the charge-compensation process in cathodes.[59,60,64] Additionally, Zn^{2+} participates in reactions leading to the production of layered basic zinc salts (hydroxide salts) on the surface of both electrodes, which eventually increases the cell impedance,[65] thereby degrading the electrode performance, and hence considered unfavorable or parasitic.[58] In addition, dendritic growth of metallic zinc is unavoidable,[61,66] and the process is facilitated by the consumption of H^+ ions and Zn^{2+} on the surface of the Zn anode.[67] Alkalization of the surface results in the propagation of Zn dendrites accompanied by passivation through the formation of $Zn(OH)_2$, ZnO, and Zn^0 moieties, reducing the cycle life of cells.[68]

In this review, we highlight the electrochemical reactions in aqueous Zn cells: (I) ionic equilibria that facilitate proton-coupled reactions, including basic salt formation; (II) the effect on kinetics for charge storage; (III) material transformation and "activation" by hydrogen ions (H^+(aq)) and water in both cathodic and anodic reactions; and IV) the suggested role of water and protons in AZIBs. Therefore, we first address ionic and electrochemical equilibria in aqueous zinc electrolytes and at the zinc | electrolyte interface; the discussion then expands to consider water-related reactions for cathodes, including intercalation and conversion reactions in aqueous and non-aqueous ZIBs.

2. Zn-H_2O chemistry in aqueous Zn^{2+} solutions

When the study of mildly acidic rechargeable zinc aqueous batteries first began, investigation of the reaction chemistry progressed mainly on the cathode materials using manganese and vanadium oxides to improve their electrode performance and examine the related phase transitions during charge storage.[69] In these studies, the mechanism of ion intercalation or compound conversion was studied in cells with a considerable excess of metallic Zn, masking the zinc electrode problems. In addition, the research on the properties of water as a solvent often did not advance beyond its high polarity and solvation ability, leaving behind its protolytic properties. As a result, the mainstream research studies underestimated the role of pH and H^+ in defining cell performance and the behavior of electrodes. In this section, we consider aqueous Zn(II) electrolytes and their ionic equilibria, whose consequences affect the use of Zn-metal anodes.

2.1. Aqueous Zn^{2+} ionic equilibria and the formation of basic zinc salts

Aqueous solutions of zinc salts were used for zinc plating before their introduction for AZIBs.[70–73] Water-based electrolytes are generally cost-effective and highly ionic conductive, with the resulting conductivity being similar to or better than that of nonaqueous electrolytes (Fig. 3a). In addition, the high conductivity beneficial for mass transport in aqueous solutions is achieved because of the large solubility of zinc salts. Moreover, aqueous electrolytes often exhibit more facile kinetics of zinc deposition/dissolution than their nonaqueous counterparts. Kundu *et al.*[32] showed that the activation energy for charge transfer at the $Zn|Zn^{2+}$ interface was almost 10 times lower for an aqueous solution than that for an acetonitrile-based one (Fig. 3b).

Water is a highly polar solvent that can dissolve many inorganic salts and provide unique solvation structures. It is also a very attractive solvent due to its low cost and versatility, making aqueous batteries more competitive than nonaqueous systems. Notwithstanding, its intrinsic high polarity and hydration character are not the only distinguishing features of aqueous electrolytes. Water is a protic solvent with a high autoprotolysis constant:

$$2H_2O \rightleftharpoons H_3O^+ + OH^- \quad (K_W = 1 \times 10^{-14}) \qquad (1)$$

H_3O^+(aq) – protonated form of water (hydronium ion, hydrated proton, H^+(aq)). In general, water molecules can easily donate, accept, or exchange protons.

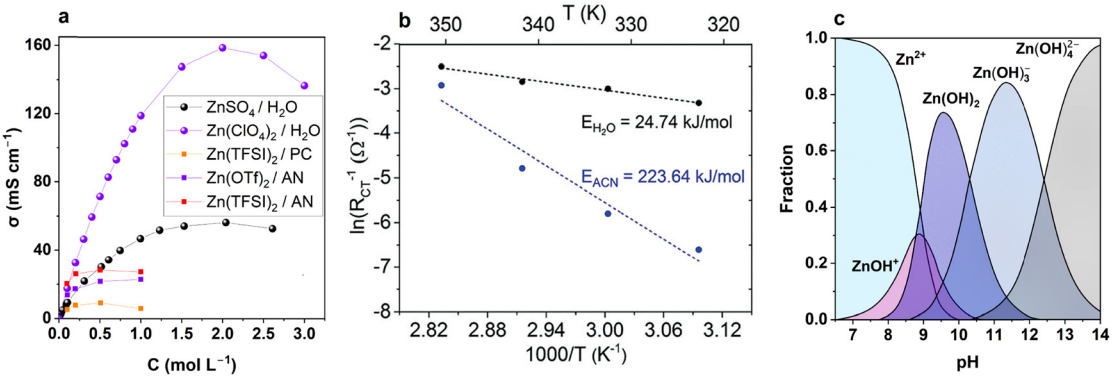

Fig. 3 Electrolytes for Zn-ion batteries. (a) Comparison of conductivity for some aqueous and nonaqueous electrolytes.[74–76] (b) Charge transfer activation energy at Zn metal interface in nonaqueous *vs.* aqueous zinc electrolyte. Reproduced from ref. 32 with permission from the Royal Society of Chemistry. Copyright 2018. (c) Distribution of Zn(II) hydroxo-complexes at infinite dilution at 298 K.[77]

Some of the most popular electrolytes in AZIB research are zinc sulfate ($ZnSO_4$) and zinc trifluoromethanesulfonate (zinc triflate, $Zn(CF_3SO_3)_2$, and $Zn(OTf)_2$), whereas zinc perchlorate, zinc nitrate, and zinc acetate are less often studied in the literature.[78] Many of these electrolytes are salts of strong acids, which negates anion protonation. However, the hydrated zinc ion, Zn_{aq}^{2+}, is a weak Brønsted acid that interacts with water, leading to mild acidity of the Zn^{2+}-related electrolyte:[77]

$$Zn^{2+} + 2H_2O \rightleftharpoons ZnOH^+ + H_3O^+ \quad (2)$$

The reported equilibrium constant for this process is $\approx 10^{-8}$–10^{-9},[77] resulting in pH values of ≈3.5–5 for commonly used zinc salt concentrations of 0.1 M to 3 M. Here, Zn^{2+} denotes the hexacoordinated aqua cation $Zn(H_2O)_6^{2+}$, which corresponds to the most stable ligand configuration in a water environment, whereas $ZnOH^+$ is also a simplified notation for the coordinated aqua cation ($Zn(H_2O)_5OH^+$).[79] Hereafter, Zn^{2+} and H^+ notation will be used to represent the aquacations throughout the work. The acidity of the zinc ion according to reaction (2) is crucial for AZIBs. Despite the equilibrium concentration of H_3O^+ (H^+) being 4–5 orders of magnitude lower than that of Zn^{2+} and the equilibrium $ZnOH^+$ concentration being low (Fig. 3c), the fast equilibrium can support the generation of protons if they are consumed in chemical or electrochemical reaction, *e.g.*, during intercalation of H^+ into cathode materials. Furthermore, the fast H^+ diffusion coefficient in water (9.3×10^{-5} cm^2 s^{-1} for H^+ *vs.* 0.7×10^{-5} cm^2 s^{-1} for Zn^{2+})[80] makes H^+ an important electroactive species in AZIBs and an active cation for charge storage in the cathode host along with or instead of Zn^{2+}.[11,17]

The hydrolysis of the Zn^{2+} cation has another effect at higher pH values. Traditionally, a Pourbaix diagram for the Zn–H_2O system depicts the formation of $Zn(OH)_2$ around neutral or slightly basic pH depending on the Zn^{2+} concentration (Fig. 4a). However, in the presence of anions, the formation of basic zinc salts (BZSs) becomes favorable as the pH of the zinc salt solution increases (Fig. 4b);[81–85] converting $Zn(NO_3)_2$ to $Zn_5(OH)_8(NO_3)_2{\cdot}2H_2O$,[83,85] $ZnSO_4$ to $Zn_4(OH)_6SO_4{\cdot}xH_2O$,[84] $ZnCl_2$ to $Zn_5(OH)_8Cl_2{\cdot}H_2O$,[82] and $Zn(OAc)_2$ to $Zn_5(OH)_8(CH_3CO_2)_2{\cdot}nH_2O$.[81] The other anions, such as triflate, can also form such basic salts.[65,86] Traditionally, many reviews and papers on ZIBs provide a Pourbaix diagram similar to that presented in Fig. 4a, whereas the basic salt area diagram more reasonably represents the actual behavior of the system.

The structure of most basic zinc salts is layered, with anions and water occupying the interlayer space (Fig. 4c). The amount of interlayer water can differ and is usually easily reduced, even upon mild drying. The chemistry of BZSs has been extensively studied aside from the field of batteries, particularly due to their ion exchange abilities.[95,96] Some of these basic salts can be used

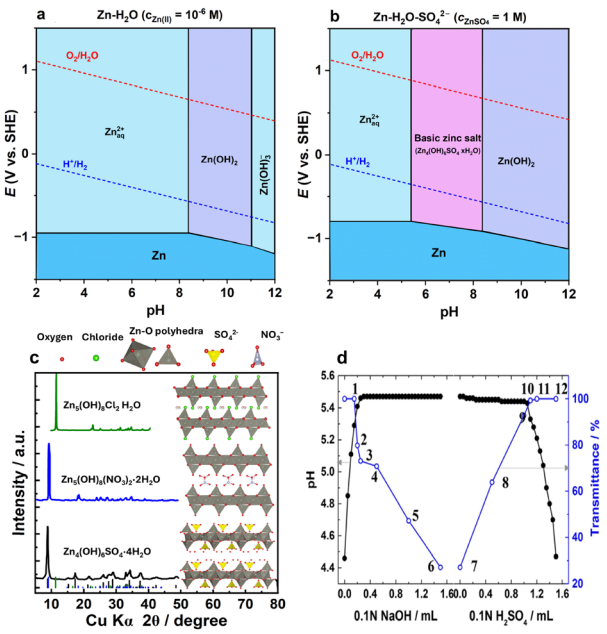

Fig. 4 Pourbaix diagrams and formation of basic salts in zinc electrolytes. (a) Pourbaix diagram for the Zn-H_2O system without consideration of anions, plotted using data from ref. 87 (b) Pourbaix diagram for the Zn–H_2O–SO_4^{2-} system calculated with respect to basic salt formation, plotted using data from ref. 87 and 88. (c) Typical layered zinc basic salts with their crystal structure and XRD patterns.[89–94] (d) Solution pH and transmittance upon NaOH and H_2SO_4 addition to $ZnSO_4$ solution. Reproduced with permission from ref. 38. Copyright 2016, John Wiley & Sons.

as catalysts[97] and for the synthesis of nano-sized oxide particles.[81,82,84]

The formation of these hydroxy salts is reversible—they can be obtained *via* direct precipitation by hydroxide addition to Zn^{2+} solution and, conversely, dissolved by acid treatment (Fig. 4d), as indicated in the equations below:[38]

$$4Zn^{2+} + SO_4^{2-} + 6OH^- + nH_2O = Zn_4(OH)_6SO_4{\cdot}nH_2O \downarrow \quad (3)$$

$$Zn_4(OH)_6SO_4{\cdot}nH_2O + 6H^+ = 4Zn^{2+} + SO_4^{2-} + (n + 6)H_2O \quad (4)$$

As the precipitation of the BZS is initiated below pH 7, it can also be rewritten in another form:

$$4Zn^{2+} + SO_4^{2-} + (n + 6)H_2O = Zn_4(OH)_6SO_4{\cdot}nH_2O + 6H^+ \quad (5)$$

The reversible chemistry of BZSs is also observed in AZIBs, where they form and dissolve at the electrode surface during discharge (reduction) and charge (oxidation) of the cathodes, respectively.[38,58,65] This phenomenon occurs when cathode materials store a significant amount of protons upon discharge and release them while charging, which is typical for many compounds used in ZIBs.[98,99] That is, the electrode serves as a source/sink of protons.

Fig. 5a presents a schematic diagram of the formation of BZSs at the interface between a cathode and an electrolyte. As mentioned above, BZS formation is preferred over $Zn(OH)_2$ deposition; therefore, the Pourbaix diagram should be constructed to account for this. Upon discharge (reduction) of the cathode, protons are consumed. A decrease in the aqueous proton concentration shifts the local pH to a higher value (Fig. 5b and c). When the surface pH of the electrode reaches that of BZS formation, the layered hydroxide salt begins to precipitate on the surface of the cathode depending on the solubility product of the corresponding basic zinc salt in the electrolyte (*e.g.*, reaction (3) for sulfate, $K_{sp} = 2.5 \times 10^{-56}$). Note that this reaction consumes hydroxide ions; thus, it acts as a buffer, and the pH near the electrode is stabilized at the pH of precipitation (Fig. 5d). Further reduction leads to the growth of the BZS and propagation of the pH gradient further into the solution bulk. Upon charging, the generation of protons (*e.g.*, by framework deprotonation) drives the dissolution of BZS. As long as the salt deposit is present, the pH change is delayed due to the buffering effect of the dissolution reaction (Fig. 5e and eqn (4)). After the complete dissolution of BZS, the pH decreases locally because no hydroxide deposit remains to neutralize protons (Fig. 5f).

The described reversible scenario refers to an isolated electrode without the effect of the zinc anode, such as when recording pH changes in a beaker cell. However, depending on the experimental conditions, various scenarios can be observed, including an extreme pH drop due to BZS delamination.[58,102] In addition, for small electrolyte volume cells, *e.g.*, coin and pouch configurations, the continuous Zn-metal corrosion would increase the pH and result in pH changes near the cathode, especially after long conditioning. Thus, a scheme such as that depicted in Fig. 5 aids in understanding the changes on a qualitative level. For a full understanding of a particular system, rigorous calculations should be performed as demonstrated, for instance, for the Zn–MnO_2 system.[103]

The precipitation of BZS on the electrode surface impacts the kinetics (Fig. 5g). The investigation of NaV_3O_8 in aqueous zinc triflate electrolyte indicated an increase in the interfacial charge-transfer resistance of 10–100 times upon the formation and growth of a basic triflate deposit.[65] The corresponding activation energy for charge transfer associated with the grown interphase was measured to be 48 kJ mol^{-1}, which is three times higher than that for charge transfer on the BZS "free" surface.[65]

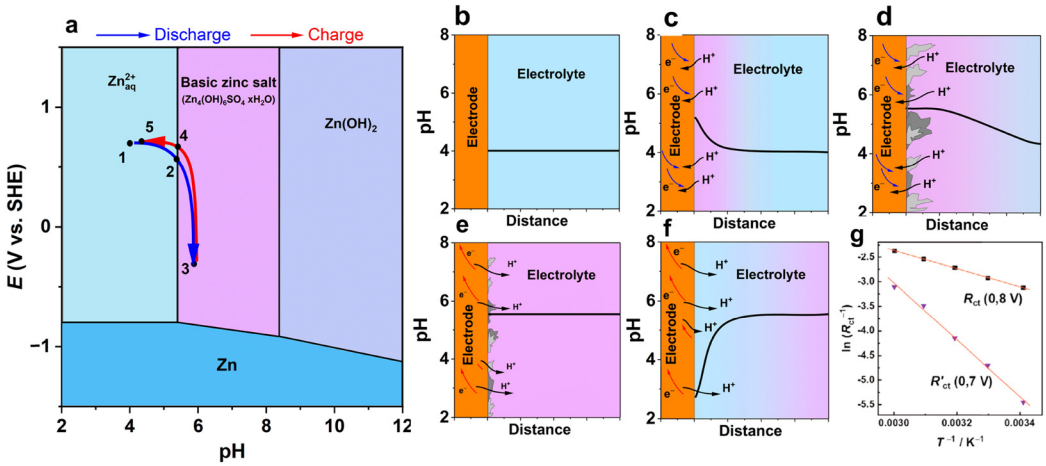

Fig. 5 A schematic diagram of pH variation at the interface between the cathode and Zn^{2+} electrolyte. (a) Pourbaix diagram for Zn-water system built taking into consideration formation of basic zinc sulfate for $c(ZnSO_4)$ = 1 M. Blue and red arrows indicate potential-pH coordinates at a cathode while moving through the diagram upon discharge and charge for an H^+-intercalating electrode; (b–f) represent pH variation at electrode | electrolyte interface at various states of discharge and formation/dissolution of BZS schematically plotted using systematization and observations of pH changes.[58,65,100–102] (g) Arrhenius plot for charge transfer resistance before (0.8 V) and after (0.7 V) precipitation of basic triflate on the NaV_3O_8 cathode. Reproduced with permission from ref. 65. Copyright 2020, John Wiley & Sons.

Table 1 Precipitation of basic zinc salts

		Precipitation pH in 1 M Zn(II) salt		
Basic salt	K_s	Calculated[a]	Experimental	Examples of BZS precipitates on cathodes in zinc batteries
$Zn_4(OH)_6SO_4{\cdot}xH_2O$	2.5×10^{-56} (ref. 88)	5.31	5.47 (ref. 38), 5.74 (ref. 102)	MnO_2,[104–106] $ZnMn_2O_4$,[107] NaV_3O_8,[108,109] V_2C MXene,[110] $A_xV_2O_5$,[111,112] VO_2[113,114]
$Zn_5(OH)_8Cl_2{\cdot}xH_2O$	8.2×10^{-76} (ref. 115)	5.04	—	$A_xV_2O_5$,[116,117] Zn–air,[118] VO_x[119]
$Zn_5(OH)_8(NO_3)_2{\cdot}xH_2O$	1.11×10^{-76} (ref. 83)	4.93	—	—
$Zn_5(OH)_8(CH_3CO_2)_2{\cdot}xH_2O$	—	—	≈7 (ref. 120)	MnO_2,[106] Thionin,[121] Zn-air[122]
Zn hydroxy triflate	—	—	5.2 (ref. 102), (2 M)	$A_xV_3O_8$,[65,100] $Na_3V_2(PO_4)_2F_3$,[86] $NH_4V_4O_{10}$,[123] VO_2,[124] MnO_2,[106]

[a] Calculated in this review using K_s values and activity coefficients.[125–127]

The pH of precipitation depends on the solubility product constant and usually lies between 5 and 6 (Table 1). An exception is zinc acetate electrolyte, which deviates from the trend due to the basic properties of the acetate anion (hydrolysis).

Most reports on basic salt precipitation cover the formation of $Zn_4(OH)_6SO_4{\cdot}xH_2O$ and basic triflate, and the different types of BZSs are summarized in Table 1. Most of the examples correspond to cathodes composed of vanadium and manganese oxides, which tend to accept H^+ upon reduction. Thus, a question arises regarding the extent to which such materials can accommodate Zn^{2+} (and not H^+) in the structure. This issue will be discussed in Section 3.

In summary, aqueous solutions of Zn(II) salts provide unique ionic equilibria. The acidity of $Zn(H_2O)_6^{2+}$ and the formation of BZSs correspond to a mildly acidic pH range, neither too low to cause strong acid etching of the materials nor too high to quickly passivate Zn, as occurs in alkaline electrolytes. More importantly, the formation of BZSs is fast and reversible. The hydrolysis of Zn^{2+} provides a stable supply of protons at the cathode during battery discharge while the deposited BZS neutralizes the protons during the charging process. At the same time, its deposition causes an increase in the surface impedance of both electrodes, which should always be considered whether studying the anode or cathode host.

2.2. Corrosion and deposition in Zn^{2+} aqueous solutions

According to the Zn–H_2O–X^{n-} (X^{n-}: anion) Pourbaix diagram (Fig. 4b), zinc metal (Zn^0) is thermodynamically unstable in contact with aqueous electrolyte at any pH. Depending on the pH, the products of the Zn reaction would be Zn^{2+}, zinc basic salts, or zinc hydroxide:

$$Zn + 2H^+ \rightarrow Zn^{2+} + H_2 \quad (6)$$

$$3Zn + Zn_{aq}^{2+} + SO_{4(aq)}^{2-} + (6 + n)H_2O \rightarrow Zn_4(OH)_6SO_4{\cdot}nH_2O + 3H_2 \quad (7)$$

$$Zn + 2H_2O \rightarrow Zn(OH)_2 + H_2 \quad (8)$$

At a longer timescale, the formation of zinc oxide is possible as a result of $Zn(OH)_2$ aging:

$$Zn(OH)_2 \rightarrow ZnO + H_2O \quad (9)$$

As a result, three important consequences for the use of zinc in Zn-metal batteries arise. First, prolonged contact of Zn with the electrolyte leads to a rise in pH from the initial value of 3–4 to 5–6, which is the pH of BZS precipitation (Table 1 and Fig. 4 and 6a). This finding implies that extended aging increases the pH of the electrolyte, which is higher than that of the fresh Zn^{2+} electrolyte, which spontaneously affects the surface state of the metallic Zn anode. Second, the abovementioned reactions (6)–(8) produce H_2 gas, threatening the safety of cells (Fig. 6b). Unfortunately, the formed H_2 bubbles adhere to the surface of the Zn anode, which in turn deteriorates cell performance caused by the uneven deposition of metallic Zn^0 during reduction. Further accumulation of the H_2 gas induces swelling or explosion of the cell. Third, the basic zinc salts and zinc hydroxide deposit as an inhomogeneous and loose film, inducing the formation of corrosion pits on the surface of the Zn anode.[58,128] A loose hydroxide deposit does not prevent corrosion, and its inhomogeneous formation predisposes zinc to unequal deposition. Thus, the zinc surface gradually corrodes, increasing the surface impedance (Fig. 6c) while simultaneously leading to the accumulation of BZS deposits on the surface.[128]

Reversible and homogeneous metal deposition is a key requirement for any battery with a metal electrode. Achieving these conditions has been a long-standing problem for zinc-metal batteries and the main obstacle to realizing commercial zinc-metal batteries. The main issue here is the formation of zinc dendrites, which can grow through a separator, causing an inner short-circuit and cell failure (Fig. 6d and e).

Although the dendrite problem is well known for non-aqueous batteries such as Li-metal batteries[131,132] or Na-metal batteries,[133,134] the presence of water significantly accelerates Zn dendrite formation through the aforementioned corrosion processes (reactions (6)–(9)). Corrosion during conditioning or a rest period creates an inhomogeneous surface. As a result, zinc is deposited at preferable sites, leading to inhomogeneous current distribution and a rough distribution of the grown metal (Fig. 6d and e). Upon subsequent oxidation, some of the grown zinc tips do not dissolve and act as new preferable sites for zinc deposition in the following cycles. The preferable deposition on tips, where the local potential stimulates faster metal growth, leads to dendrite growth and, after some time, to an inner short circuit. Furthermore, the freshly deposited zinc surface is also exposed to corrosion, which accelerates the rate of hydrogen evolution, dendrite formation, and, eventually, cell failure. These side reactions are sometimes referred to in the literature as the "vicious cycle"[61] or "domino effect".[62] Investigation of zinc

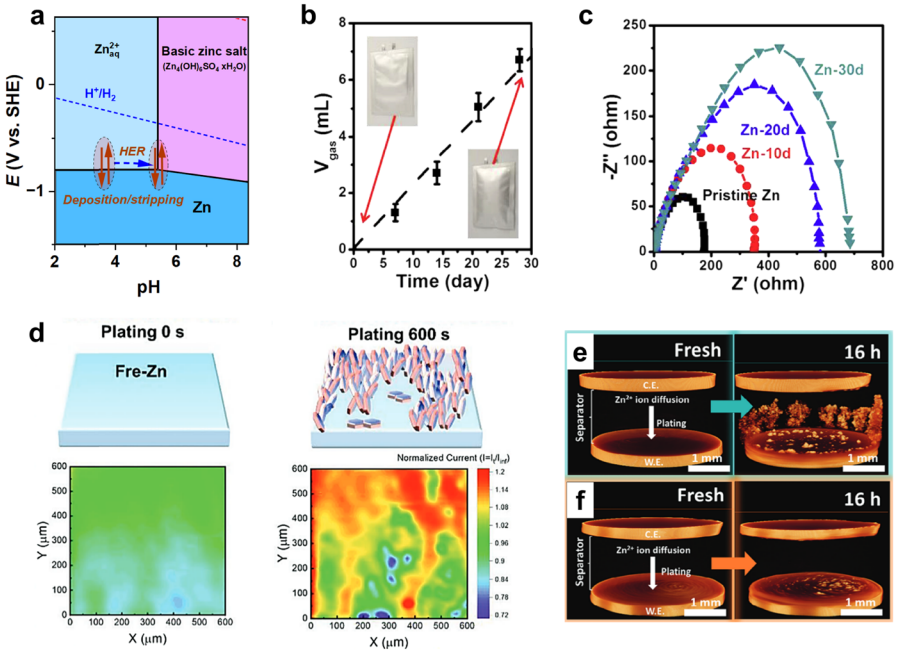

Fig. 6 Zn corrosion and deposition in aqueous Zn-electrolyte. (a) Pourbaix diagram for Zn-water system built considering formation of $Zn_4(OH)_6SO_4 \cdot nH_2O$. (b) Hydrogen evolution during rest time in a pouch cell (3 M $ZnSO_4$). Reproduced with permission from ref. 128. Copyright 2020, Elsevier. (c) Impedance spectra of Zn|Zn symmetrical cell by aging (3 M $ZnSO_4$). Reproduced with permission from ref. 128. Copyright 2020, Elsevier. (d) Scanning electrochemical microscopy feedback images of local current upon Zn deposition. Reproduced with permission from ref. 129. Copyright 2023, John Wiley & Sons. (e) Dendrite formation upon Zn electrodeposition on bare Zn surface and moderate deposition (f) on the gold sputtered surface. Reproduced with permission from ref. 130. Copyright 2023, John Wiley & Sons.

metal is interrelated with precise hydrogen quantification and understanding of pH changes, the hydrogen evolution reaction rate, and zinc deposition/dissolution. Therefore, further work is needed to minimize or eliminate hydrogen evolution and suppress dendrite growth.

The effect of pH and H_2 evolution on zinc-metal electrochemistry and zinc-battery performance was considered in recent studies.[98,135–141] Yang *et al.*[142] investigated the relationship between hydrogen evolution and the current efficiency for Zn deposition. Fig. 7a shows the improvement in the average current efficiency (ACE) from 76% to 99% by increasing the current density from 0.033 to 20 mA cm^{-2} at a limited areal capacity of 1.0 mA h cm^{-2}. Correspondingly, the hydrogen evolution reaction (HER) efficiency was reduced at higher current densities, resulting in a smooth Zn surface after zinc deposition.[142]

In a recent study, Roy *et al.*[140] utilized *in situ* electrochemical mass spectrometry (ECMS) for tracking hydrogen flux. As shown in Fig. 7b and c, an increase in the current density magnitude facilitates H_2 evolution. In the set of experiments, current densities of −0.5 mA cm^{-2}, −1.0 mA cm^{-2}, and −1.5 mA cm^{-2} lead to the generation of 2.05, 2.38, and 2.84 nmol H_2 over 600 s. At the same time, the HER efficiency dropped from 0.62% to 0.31%, indicating that zinc deposition intensifies faster than the HER rate under negative polarization. This finding agrees with the results of Yang *et al.*[142] who reported a low CE at low rates (Fig. 7a). Additionally, the hydrogen evolution for 3 h of resting period resulted in 5.16 nmol H_2, which cannot be neglected when compared with the gas generated during deposition.

The abovementioned studies strongly highlight the importance of zinc stability during long resting periods and its deposition efficiency under slow-charge conditions. One way to address the HER problem and control zinc deposition is to add pH buffer to the electrolyte, shifting and stabilizing the pH at more basic values than a pristine electrolyte. Such an approach has been used in various studies,[136,139,143–145] often by adding amines to Zn^{2+} aqueous electrolyte. Fig. 7d shows the effect of pyridine and imidazole additives on pH stabilization during zinc deposition and the HER rate by pH upshifting.[139] As a result, the corresponding coulombic efficiency (CE) and the cyclability of zinc were significantly enhanced by the effect of additives (Fig. 7e). It is worth mentioning that the ability of external buffers to upshift the pH is limited by the zinc salt used; namely, the resulting pH can be stabilized by forming BZS (Table 1) as the pH increases to the precipitation condition of BZS during the reaction. In addition, some functional molecule additives can suppress the HER through adsorption on the Zn surface or by altering the solvation structure.[141] Hence, a critical and comprehensive evaluation of how strongly adsorption, solvation, or buffering can inhibit the HER is critical in designing additives for AZIB electrolytes. Tribbia *et al.*[135] used an indium-based substrate to achieve dendrite-free zinc deposition. The measured hydrogen flux was found to be much lower for the indium substrate compared to that for the bare zinc, suggesting a correlation among hydrogen evolution, Zn deposition efficiency, and cyclability.

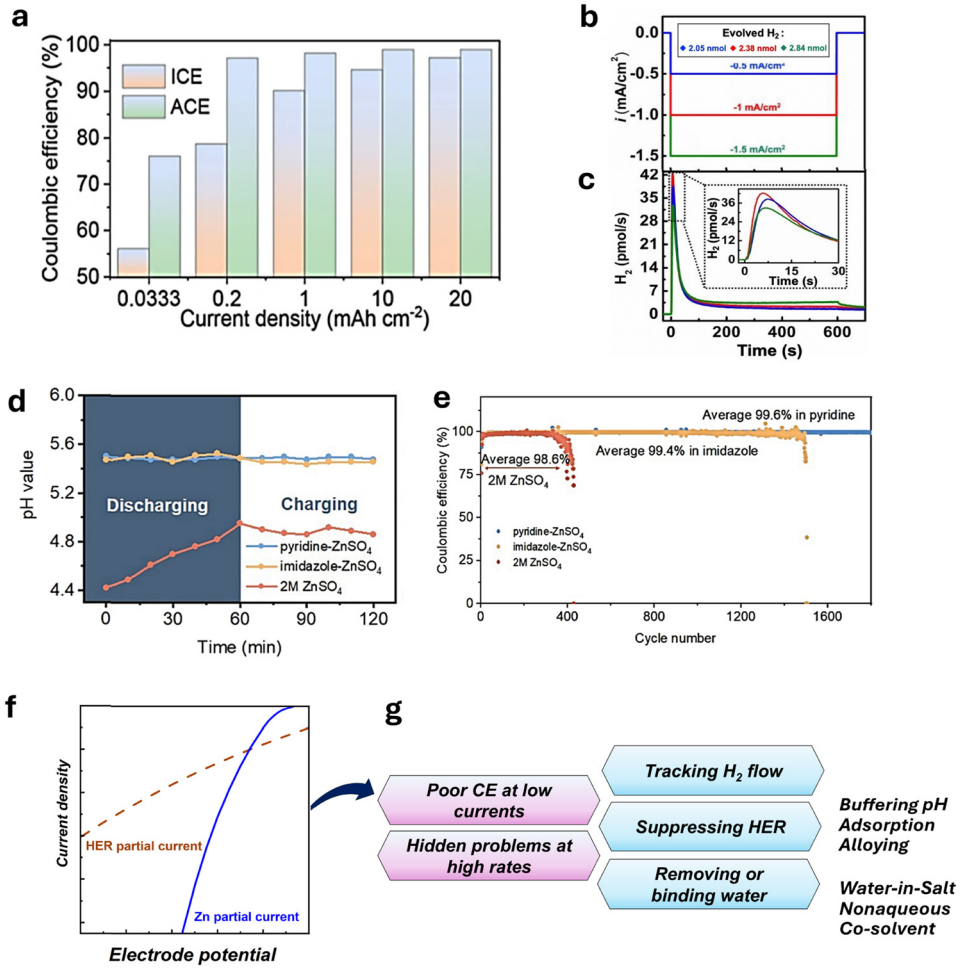

Fig. 7 Efficiency of Zn deposition and HER. (a) Zn plating/stripping efficiency depending on current density. Reproduced from ref. 142 with permission from the Royal Society of Chemistry. Copyright 2024. (b) Galvanostatic Zn deposition and (c), corresponding hydrogen evolution reaction (HER) rate. Reproduced with permission from ref. 140. Copyright 2024, John Wiley & Sons. (d) pH in Zn anode proximity by time in buffered and blank 2 M $ZnSO_4$ and (e), CE for Zn/Cu in 2 M buffered and blank 2 M $ZnSO_4$ Reproduced with permission from ref. 139. Copyright 2023, John Wiley & Sons. (f) Schematic ratio of Zn deposition and HER partial currents. (g) Highlighted problems and issues of the Zn anode.

Although buffering, adsorptive additives, and alloying show promising results in enhancing Zn-metal performance,[130,135,139,141] the slow H_2 evolution and Zn corrosion appear to be inevitable in common water-based electrolytes.[135,140,141] These findings imply that additives or surface-modification approaches can kinetically delay the HER, whereas, more importantly, the thermodynamic instability remains unresolved. Overcoming this issue is critical for practical-scale applications if AZIBs with high areal capacities (>2 mA h cm^{-2}) are subjected to long resting periods (hours, days, and weeks).[59] Switching the electrolyte to a nonaqueous system may be a solution to the problem; however, it is challenging to adopt nonaqueous Zn electrolytes due to their inferior salt solubilities, conductivities, and reaction kinetics, as considered in Fig. 3. More importantly, it should be considered that there are much fewer opportunities to find suitable cathode materials that warrant stable electrode performance in nonaqueous electrolyte.

Taking advantage of the benefits of both aqueous and nonaqueous systems, recent studies have explored the mixing of water and organic solvents over the last few years.[35,36,146,147] In such systems, the water activity is suppressed by interaction with an organic co-solvent. The water hence cannot cause considerable corrosion and HER, but there is a sufficient amount of water to enable fast interfacial charge transfer for zinc ions. For example, a mixture of dimethyl carbonate, zinc triflate, and water enhances the current efficiency and cyclability, which eventually prevents the formation of BZSs during cycling.[35] Nazar and colleagues[36] demonstrated efficient Zn plating/stripping in water-sulfolane electrolytes at an areal capacity of 4 mA h cm^{-2} and long-term full-cell performance in combination with vanadium oxide and iodine-based positive electrodes. In addition, highly concentrated solutions or even water-in-salt electrolytes are suitable for enhancing the current efficiency for zinc deposition/stripping.[148–150] Besides directly controlling water or proton activity, zinc deposition/stripping can be improved using various coatings, functional separators, and other approaches.[61,66,67]

Thus, there is no doubt that various approaches allow to manage the HER problem in zinc batteries in a certain way. Let's now consider how these approaches work on the micro

level; for this, we need to consider kinetics, interfacial, and solvation structures.

As the HER on Zn is thermodynamically barely avoidable, even at low water content, most methods focus on slowing down the reaction kinetics to inhibit the process. The HER usually proceeds *via* Volmer–Heyrovsky or Volmer–Tafel mechanisms. In both mechanisms, the first step involves the reduction of a solvated proton, which generates a hydrogen adatom on the active surface site. In the Volmer–Heyrovsky mechanism, this is followed by the reduction of the second H^+ at the same site. In contrast, the Volmer–Tafel mechanism involves the recombination of two adsorbed hydrogen adatoms, resulting in the formation of a hydrogen molecule (H_2).[151] During HER, hydrogen adsorption affects the reaction kinetics. Fig. 8a shows the dependency of HER exchange current density on metal–hydrogen bond energy.[152] The plot has a volcano-shape following the Sabatier principle, which states that an intermediate in heterogeneous catalysis should be bound neither too weekly nor too strongly for facile reaction. In contrast to the catalysis field, zinc metal battery research should focus on HER inhibition. As seen in Fig. 8a, zinc lies in a low HER activity area, which, in fact, allows usage of mildly aqueous electrolytes. Following this principle, alloying or covering zinc electrodes with HER inhibiting metals would slow down hydrogen evolution. For instance, an amalgamation of zinc was shown to suppress the HER on the zinc surface[153] as mercury is historically known for its extremely high HER overpotential. Alloys and coating with other metals that exhibit low affinity for hydrogen have been shown to reduce corrosion such as the indium,[135] indium–gallium–zinc alloy,[154] or lead coating.[155] A recent study also shows promising behavior of zinc–bismuth alloy, while usage of nickel results in an opposite effect, as nickel enhances HER catalysis (Fig. 8b).[156] Thus, the application of the electrocatalysis principles through zinc alloying appears to be promising in addressing aqueous zinc corrosion.

Even if slowed down, the prolonged contact of zinc atoms with H_2O molecules would lead to hydrogen evolution and corrosion. Moreover, upon deposition, hydrated zinc ions, $Zn(H_2O)_6^{2+}$, would release water molecules on fresh Zn surface upon desolvation.[161] This, in combination with zinc ion depletion and negative polarization, would result in an enhanced HER rate. Thus, various approaches are applied to minimize local water concentration at the zinc interface or to remove direct Zn|H_2O contact.

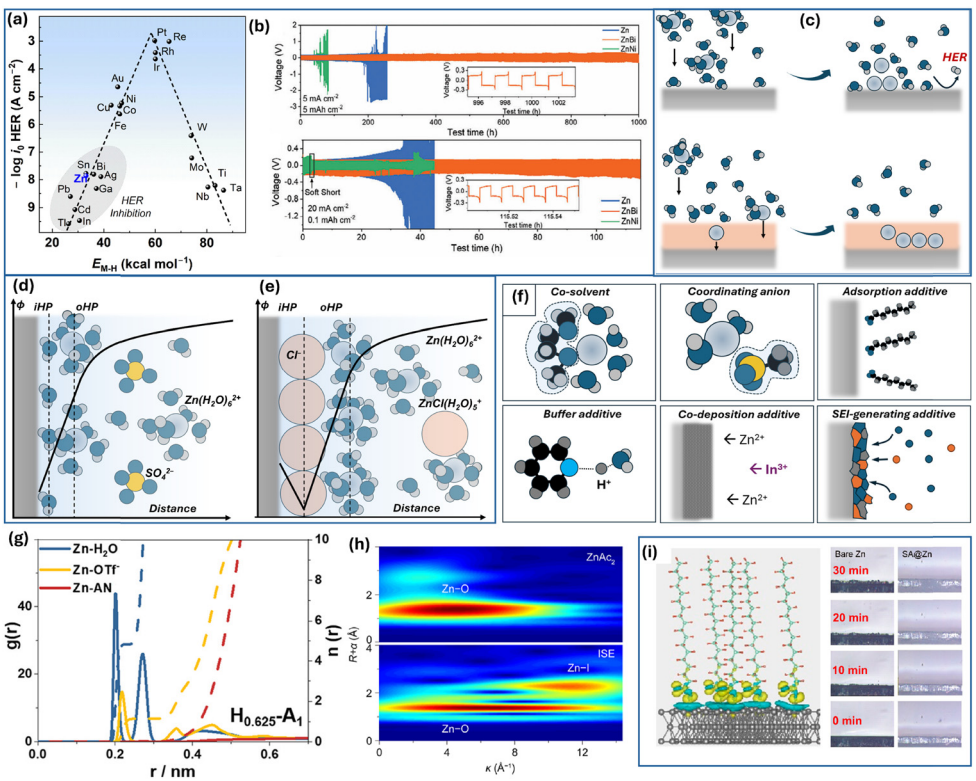

Fig. 8 Interface of Zn electrode and Zn^{2+} solvation. (a) Volcano plot of HER activity on metal electrodes (data are from ref. 152). (b) Cyclic performance of Zn, Zn–Bi, and Zn–Ni alloys in symmetrical cells with Zn^{2+}-electrolyte (Adapted with permission from ref. 156. Copyright 2024, John Wiley & Sons). (c) Schematic representation of "pre-desolvation" layer on the zinc surface. Scheme of the double layer structure for zinc electrode in contact with (d) zinc sulfate electrolyte and (e) zinc chloride electrolyte; based on ref. 157. (f) Various additives and modifications to electrolyte solution by their action principle. (g) The radial distribution function for zinc triflate in a H_2O–acetonitrile mixture. Adapted with permission from ref. 158, Copyright 2022, Elsevier). (h) Wavelet transform images of the EXAFS spectra for $Zn(OAc)_2$ and $Zn(OAc)_2$ + NH_4I mixed electrolyte (Adapted with permission from ref. 159, Copyright 2022, American Chemical Society). (i) Differential charge density for stearate adsorbed on the zinc surface and morphology of deposition at 10 mA cm^{-2} of bare and modified surface (Adapted with permission from ref. 160, Copyright 2023, American Chemical Society).

One way of preventing direct contact of zinc with H_2O molecules is the design of a zinc-ion conductor layer, which accepts zinc ions upon desolvation and assists in their transport to the growing Zn interface. This process helps minimize the area of zinc exposure to the electrolyte and, ideally, promotes a uniform zinc ion flux across the electrode surface (see Fig. 8c). For instance, thin layers of ZnF_2 have been shown to exhibit the desired ionic conductivity and transport properties.[162,163] The ZnF_2 layer, grown through HF-gas transport reaction by decomposition of NH_4F, was demonstrated to have an interstitial diffusion mechanism allowing transport to the zinc surface.[163] Having an open structure, metal hexacyanoferrates can act as suitable zinc ion transport layers.[164–166] For example, a $Zn_3[Fe(CN)_6]_2$ (ZnHCF)-modified separator can enhance cyclic stability.[166] It is likely, that the ZnHCF-layer moderated the Zn^{2+} flux by increasing the zinc transference number. Various metal–organic frameworks and covalent frameworks are other open-channel structures suitable for such layer design.[167–169] In recent work, a β-ketoenamine-linked fluorinated covalent organic framework was used to create a crystalline 2D layer on Zn.[169] The layer contained 1D fluorinated nanochannels, which facilitated hopping for zinc ions while preventing water infiltration, as suggested by the observed lower HER currents and higher Tafel slope. Various polymer-based films were demonstrated to regulate Zn deposition.[170–172] Interestingly, the immobilization of anions in the polyelectrolyte membrane allows increasing the Zn^{2+} transference number to 0.96, making the membrane layer almost exclusively Zn^{2+}-conductive and enabling uniform Zn deposition.[171]

Overall, designing Zn^{2+}-conductive layers is a viable approach to suppress corrosion and moderate deposition of zinc. It is crucial to analyze the mechanisms and estimate the ionic and electronic conductivity of these layers, as well as assess their structural integrity after prolonged cycling and susceptibility to cracks and zinc overgrowth.

Zinc deposition and water reduction are also sensitive to anion adsorption and double-layer structure. It is well-reported that $ZnCl_2$ allows more stable Zn stripping–deposition than $ZnSO_4$ or $Zn(ClO_4)_2$ and generates lower amount of passive films.[173] Although it can be ascribed to the solvation shell structure as Cl^- tends to substitute H_2O in the zinc coordination environment at high concentration, chloride ions are known for specific adsorption. In a recent study by Lai *et al.*, measurements of surface tension of a mercury drop in Zn(II) electrolytes and related analysis allowed recreating surface excesses of ions in the vicinity of the electrode.[157] The chloride showed specific adsorption behavior with the potential of zero charge being negatively shifted and dependent on electrolyte concentration compared to $ZnSO_4$ behavior. Chloride ions tend to occupy the inner Helmholtz plane, causing the attraction of Zn^{2+} (Fig. 8e). Thus, the interfacial vicinity is enriched with both Zn^{2+} and Cl^- in 1 M $ZnCl_2$ compared to 1 M $ZnSO_4$ (Fig. 8d and e). Thus, such double layer structure and higher local concentration of Zn^{2+} likely contribute to better Zn^{2+}/Zn kinetics.[157]

The deposition efficiency of zinc, the hydrogen evolution reaction, the double-layer structure, and the solvation shell of zinc ions are all closely interconnected. Consequently, various additives and electrolyte modifiers are actively being investigated (Fig. 8f). An effective approach involves the use of organic co-solvent additives. These co-solvents interact with water, modulating the hydrogen bonding network, weakening the bond between Zn^{2+} and H_2O, or altering the Zn^{2+} solvation shell by incorporating co-solvent molecules into the coordination sphere.[174] For instance, dimethoxyethane (DME) was shown to modify the solvation shell in a H_2O–DME mixed electrolyte.[175] Interestingly, the introduction of DME into the coordination environment also induced coordination between Zn^{2+} and $CF_3SO_3^-$. This likely altered SEI composition and structure creating a ZnF_2–ZnS-rich layer that contributed to more reversible behavior. Similar to DME, triethylene glycol (TEG) co-solvent acts as a bidentate chelating agent, reducing the number of H_2O in the first coordination sphere from 6 to 3 and promoting the incorporation of triflate anion into the coordination shell.[176] The SEI derived from this electrolyte was found to exhibit an organic–inorganic bilayer-like structure with a ZnF_2-rich inner layer. Zhao *et al.* demonstrated that the acetonitrile co-solvent modifies the hydrogen bond network and promotes the substitution of water by triflate anion in the solvation shell (Fig. 8g).[158] Notably, co-solvent does not necessarily participate in the first solvation shell. 2-Propanol, as a relatively weak ligand contributes to the outer solvation shell. Nevertheless, this modification facilitates stable zinc deposition with a preferential (101) orientation.[177] A recent study demonstrated that the 2,2,2-trifluoroethanol (TFEA) co-solvent weakens the tip effect of zinc deposition and effectively suppresses the dendrite growth. While TFEA does not participate in the inner solvation shell, it has been shown to disrupt the hydrogen bonding network, facilitating the incorporation of triflate anions into the inner coordination shell.[178] Overall, the co-solvent strategy appears to be one of the most promising approaches in ZIB development. In addition to its direct effects, such as reducing water activity and decreasing the number of water molecules in the Zn^{2+} coordination shell, co-solvents typically influence the SEI structure and, in many cases, mitigate the dissolution of cathode materials. Consequently, they contribute to enhanced cycling stability, functioning as multifunctional electrolyte components.

Similar to how the solvent affects the solvation shell, electrolyte can be modified by using different salts or anions. The effect of chloride on adsorption and coordination has been already mentioned above. Similarly, other halogen ions coordinate with zinc ions at high concentrations forming complexes such as $ZnI(H_2O)_5^+$ in a mixed zinc acetate–ammonium iodide electrolyte (Fig. 8h).[159] The addition of sodium tartrate as a dual-functional additive for absorption and solvation shell modification was shown to benefit (002) zinc growth and enable long-term stability.[179] The elimination of "free" water and decrease in the amount of solvated water is often achieved by WiS electrolytes, which at the same time becomes less conductive and more viscous.[148–150] To overcome this issue, a combination of cosmotropic and chaotropic anions could be effective in maintaining a sufficiently low water concentration while providing better conductivity and allowing long-term Zn deposition–stripping.[180] The use of coordinating anions like

acetate[181] also allows stable cycling with zinc concentrations being relatively low compared to those of WiS electrolytes. In addition, the combination of Zn^{2+} ions and acetate (CH_3COO^-) ions in the electrolyte helps buffer the acidity of Zn^{2+} and manage the high viscosity of concentrated $ZnCl_2$.[182]

Specific adsorption of some anions opens one more way to address Zn corrosion and side reactions. As verified by spectroscopic techniques and DFT calculations, the adsorption of dodecyl benzene sulfonate leads to an H_2O-poor double-layer structure.[183] It was also argued that such adsorbate contributed to the desolvation of zinc ions, which in turn allowed a long lifespan even in aqueous $ZnSO_4$. The water-repelling adsorbate layers were created in different studies by utilizing trace amounts of perfluorooctanoic acid,[184] phytic acid anions,[185] amino acids,[186] and fatty acids such as stearic acid[160] (Fig. 8i). Thus, the adsorption of individual ions and solvated structures such as $Zn(H_2O)_6^{2+}$ or $Zn(H_2O)_nCF_3SO_3^-$ (ref. 187) as well as local hydrogen bond dynamics[161] strongly affects the electrode kinetics of zinc deposition and HER.

Other electrolyte additives and modification strategies, including buffer,[143–145] co-deposition/alloying ions,[188–190] and functional species promoting *in situ* SEI layer formation,[191–193] are of high importance for suppressing side reactions on zinc.

Overall, the study on additives holds much promise for zinc-ion and zinc-metal batteries. As evident from the examples above, rare additives affect only one parameter. More often, simultaneous changes in various properties are observed: a co-solvent changing both the solvation shell and the growing SEI, along with an anion capable of adsorbing on the zinc surface and coordinating with Zn^{2+} ions. Such multifunctionality introduces problems of "correlation *vs.* causation" in finding the key factors responsible for performance enhancement. Therefore, careful research of the electrolyte and interface structure must be performed by using a combination of experimental (Raman, FTIR, EXAFS, NMR, and XPS) and theoretical (molecular dynamics and DFT-calculations) methods.

Considering all these points, mildly acidic aqueous Zn^{2+} electrolytes have enabled the rapid growth of ZIB research but appear to be insufficient for long-term performance, especially with high, commercial-related current densities and extensive zinc utilization. Hence, further development requires the strict suppression of the side reactions and control of water activity. For this reason, the application of mixed electrolytes, water-in-salt electrolytes, and functional additives and coatings is promising. At the same time, research on Zn anodes and Zn deposition should be conducted critically, with an appropriate estimation of the deposition/stripping CE (*e.g.*, by using the reservoir half-cell method[194,195]), without avoiding low current densities and resting times, and providing valid tracking of H_2 evolution.

3. Protons, water, and cathodes

According to the literature survey, the main topics covered for AZIBs are the crystal structure, polymorphs, defects, and electrode compositions, whereas the role of water, pH, and protolytic reaction have often been overlooked in explaining the reaction mechanism of AZIBs. In addition, the electrode performance and synthesis-based studies usually do not highlight structural investigation or activation phenomena after multiple charge–discharge cycles. Recent studies have revealed that charge compensation by Zn^{2+} insertion and/or extraction into/out of the host structure is not the main reaction responsible for the reversible capacity of many host materials, although Zn^{2+} is the main component of the aqueous electrolyte. That is, many materials are unable to store Zn^{2+} at a high extent and instead serve as hosts for protons provided by Zn^{2+}–H_2O ionic equilibria. In addition, the high reactivity of water and its ability to accept and donate protons allows various dissolution, redeposition, and amorphization reactions, making AZIBs distinct from nonaqueous batteries.

3.1. Scenarios of Zn^{2+} and H^+ intercalation

Various types of active materials act as intercalation hosts when (dis)charged in aqueous zinc electrolytes (Fig. 9). The reversible X-ray diffraction (XRD) peak shift is often observed as a clear indicator of the intercalation reaction. As the aqueous zinc electrolyte can donate protons (reactions (2) and (5)), many materials tend to adopt H^+ ions rather than Zn^{2+} ions when discharged or H^+/Zn^{2+} co-intercalation can occur.[11,18] BZS precipitation usually serves as an indicator of H^+ intercalation and is typically observed for manganese-oxide- and vanadium-oxide-based materials as BZS peaks emerge and vanish in a cyclic manner (Fig. 9b). In addition, intercalation of Zn^{2+} can proceed in different ways, depending on the participation of solvated water in intercalation (Fig. 10a and b). The domination of a particular mechanism is strongly affected by the type and structure of the electrode materials.

3.1.1. Desolvated Zn^{2+} intercalation. Intercalation of a charge carrier into the host structure *via* solid-state diffusion (Fig. 10a), when Zn^{2+} fully loses its solvation shell, is not a typical scenario for AZIBs, although it is common for metal-ion batteries such as Li-ion and Na-ion batteries. A basic explanation for this behavior is the high charge density of the multivalent ion, which inevitably slows down its transport in a periodic crystal structure due to the strong coulombic interactions with the host lattice.[5,12] These issues are typical for any multivalent battery and impede the development and implementation of such power sources.[5] Desolvation can be a limiting factor during electrochemical reactions with a high activation energy.[32] For these reasons, desolvated metal-ion intercalation is not the major mechanism observed in AZIBs and is mainly limited to some metal chalcogenides, oxide spinels, and metal hexacyanoferrates (Prussian blue analogues).

Molybdenum chalcogenides Mo_6X_8 (X = S, Se) known as Chevrel phases are well-known hosts for different ions due to their unique crystal structures. Their ability for electrochemical intercalation of zinc ions was demonstrated long before the resurgence of AZIB research.[25] It is known that their electrochemistry usually includes the stepwise formation of $ZnMo_6X_8$ and $Zn_2Mo_6X_8$ near 0.5 V and 0.3 V *vs.* Zn^{2+}/Zn, respectively for Mo_6S_8.[198,237] The limited specific capacity and low Zn intercalation potential have resulted in poor interest in practical applications; however, their unique structure makes them interesting materials for mechanistic studies.

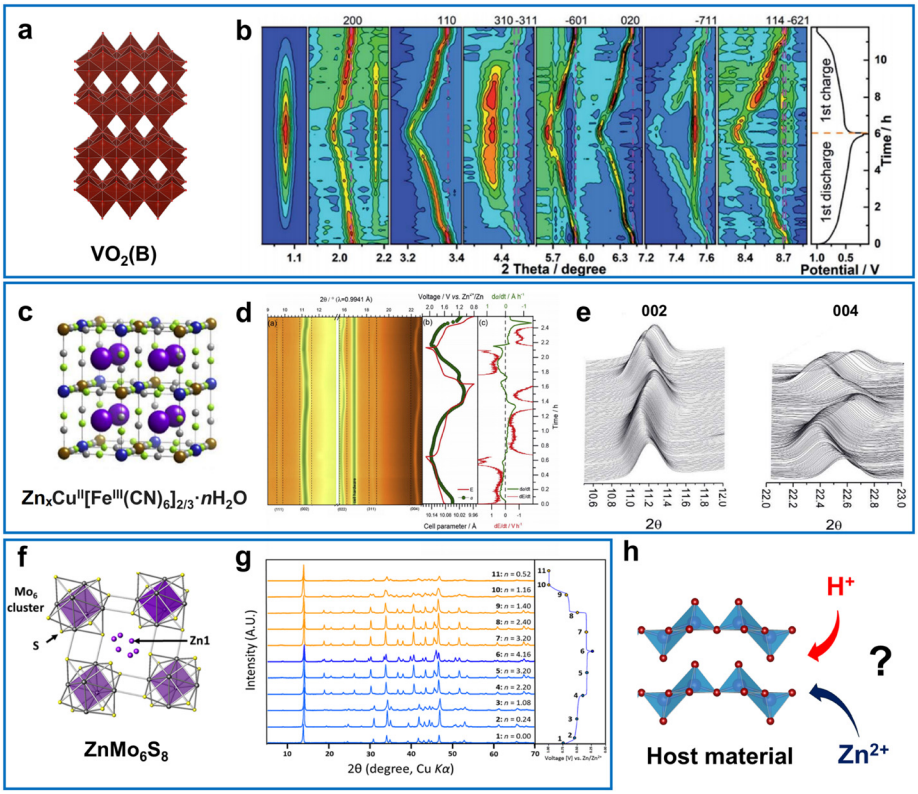

Fig. 9 Examples of intercalation-type host materials in aqueous Zn-metal batteries. (a) Crystal structure and (b), *operando* XRD for VO_2(B) in aqueous 1 M $ZnSO_4$. Reproduced from ref. 196 with permission from the Royal Society of Chemistry. Copyright 2020. (c) Crystal structure and (d) and (e) *operando* XRD for copper hexacyanoferrate in aqueous 1 M $ZnSO_4$ Reproduced with permission from ref. 197. Copyright 2017, Elsevier. (f) Crystal structure for $ZnMo_6S_8$ and (g), corresponding *ex situ* XRD after (dis)charges in 0.1 M $ZnSO_4$. Adapted with permission from ref. 198. Copyright 2016, American Chemical Society. (h) The ambiguity of guest ions for aqueous ZIBs.

Several studies have demonstrated that spinel oxides such as Zn–Al–Co[30] and Zn–Ni–Mn–Co[199] oxides serve as Zn intercalation cathodes in non-aqueous electrolytes. However, presumably due to the low current efficiency and the high potential of Co^{4+}/Co^{3+} and Ni^{4+}/Ni^{3+} redox, such compounds have not been examined in an aqueous environment. For aqueous systems, a highly stable battery based on Zn^{2+} intercalation has been reported for the cation-deficient $ZnMn_2O_4$ spinel.[215] However, good capacity was observed in nanocomposites with carbon, indicating the importance of the material preparation method, composition, and vacancy character for effective zinc-intercalation kinetics.

Metal hexacyanoferrates (MHCFs), often referred to as Prussian blue analogues, usually have a cubic or rhombohedral open structure with channels suitable for accepting multivalent ions.[238,239] Unlike metal oxides, the XRD patterns of MHCFs do not show feature of basic salt deposits (Fig. 9c–e), thus indicating the dominant Zn^{2+} insertion chemistry rather than H^+ storage. The specific capacity of MHCFs is usually below 100 mA h g^{-1}, activated by the iron redox, whereas the electrode performance is not so attractive due to the small capacity in Zn cells.[238–243]

Another class of materials with reported ability towards Zn^{2+} (de)intercalation is transition-metal phosphates, including NASICON-type vanadium phosphates.[244] The reversible intercalation chemistry of Zn^{2+} has been reported for $LiV_2(PO_4)_3$, which possesses high power density and high performance at low temperature.[245] The ability for Zn storage is not limited to vanadium phosphates only; a recent study reported that $Zn_2Fe(PO_4)_2$ undergoes reversible Zn^{2+} insertion/extraction in a nonaqueous electrolyte.[246] However, notably, such compounds, especially V-containing ones, tend to decompose in a water environment, resulting in H^+-affinitive vanadium oxides as decomposition products.[247] Conventional Zn^{2+}-ion intercalation is possible for various compounds mentioned above; however, it is not what generally allows facile kinetics, which makes research on aqueous ZIBs so popular. Proton insertion, the interaction of crystal water with zinc ions, and water co-intercalation are processes that enable high-rate performance and better kinetics in AZIBs.

3.1.2. Water co-intercalation and charge screening. The intercalation of Zn^{2+} ions is reported to proceed more feasibly when supported by structural water molecules in the host material (Fig. 10b). Such an effect is usually observed for layered compounds, which accommodate water between interlayers, such as $V_2O_5{\cdot}nH_2O$ or similar compositions,[248,249] produced by employing metal ions[249–252] or organic molecules and ions[253–255] as interlayer-stabilizing structures sometimes referred to as "pillars". The interlayer water aids in charge screening and hence decreases coulombic ion–lattice interactions. This is often called the "lubricating effect" as the resulting transport kinetics within a solid is highly enhanced. Other examples that have been reported to

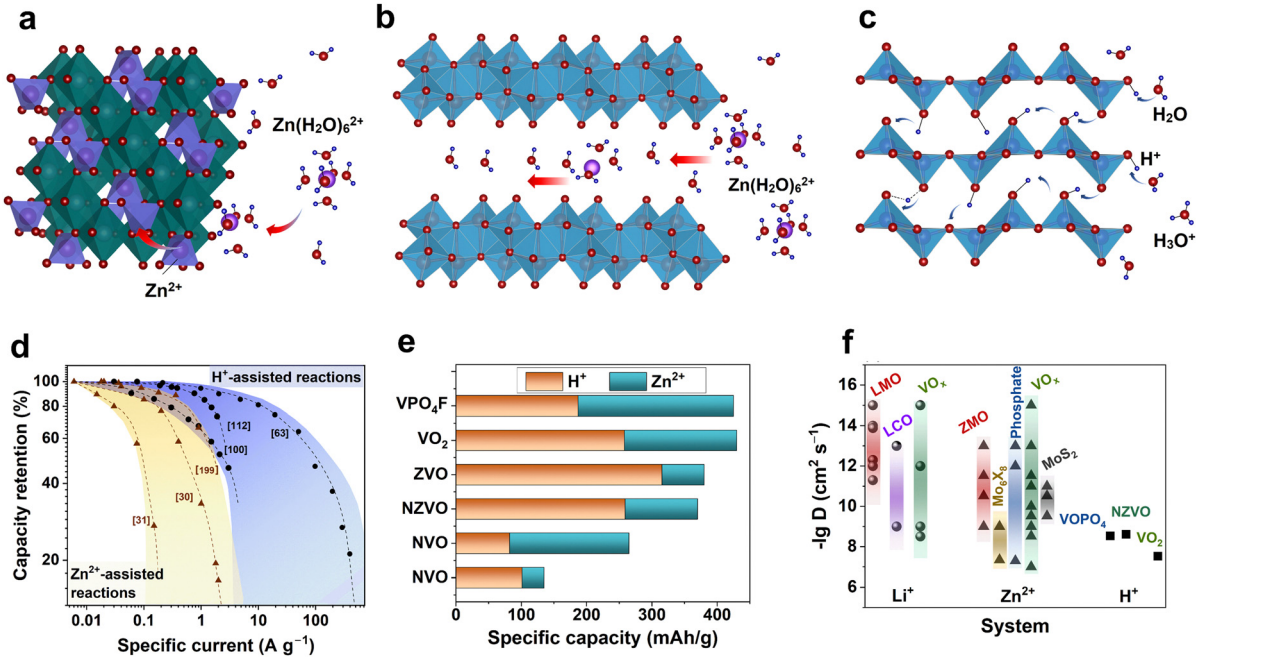

Fig. 10 Intercalation of Zn^{2+} and H^+ into host materials. Schematic illustrations of (a) Zn^{2+} intercalation accompanied by ion dehydration. (b) Zn^{2+} intercalation with participation of interlayered water acting as "charge screen". (c) H^+ insertion into metal oxide. (d) Rate capability of various systems relying on proton (Zn-metal aqueous battery) and zinc ion insertion (nonaqueous ZIBs).[30,31,63,100,112,199] (e) Contribution of Zn^{2+} and H^+ to specific capacity achieved from various materials.[25,63,108,200–203] ZVO – zinc vanadium oxide, NZVO – sodium zinc vanadium oxide, NVO – sodium vanadium oxide. (f) Comparison of reported diffusion coefficients for Li^+,[204–214] Zn^{2+},[107,215–234] and H^+ (ref. 63, 235 and 236) for various cathode materials. LMO – lithium manganese oxide, $Li_xMn_2O_4$, LCO – lithium cobalt, Li_xCoO_2, and ZMO – zinc manganese oxide, $Zn_xMn_2O_4$.

enable zinc intercalation by H_2O include interlayer-modified transition-metal disulfides and diselenides.[256–260] Indeed, hydrated MoS_2 demonstrated enhanced capacities and kinetics in aqueous zinc electrolytes, with this performance attributed to a water charge-screening effect or the effect of vacancies.[258,260] Another way to enlarge the MoS_2 layer and stimulate better performance is to introduce polymers such as poly(3,4-ethylenedioxythiophene) (PEDOT) or polyaniline.[256,259]

However, introducing interlayer organic molecules, especially redox-active molecules with basic functional groups such as $-NH_2$ results in high affinity for the H^+-assisted redox process, and, hence, H^+ rather than Zn^{2+} insertion for charge storage.

3.1.3. H^+ and H^+/Zn^{2+} co-insertion. As demonstrated earlier, the $Zn^{2+}/Zn(OH)^+$/BZS equilibrium explains the source of protons for cathode active materials. Proton insertion and H^+/Zn^{2+} co-insertion are considered as the typical charge-storage scenarios for vanadium oxides[261,262] such as VO_2[200,235] and various vanadates with the common formula $M_aV_xO_y$ (*e.g.*, NaV_3O_8 and or $K_2V_3O_8$), as illustrated in Fig. 10c.[63,100,109,201,263–265] However, the associated mechanism requires clarification and can vary depending on the experimental conditions; in addition, phase transformations and amorphization can occur during the initial several cycles.[100,109,265] A study on δ-$Ca_{0.34}V_2O_5$ using *operando* pH monitoring demonstrated co-intercalation of H^+ and Zn^{2+} with an exchange behavior, for which Zn^{2+} deintercalation progressed accompanied by *via* H^+ intercalation.[101] The fast kinetics of various vanadium (hydro)oxides can be a result of fast proton transport, rather than slow Zn^{2+} diffusion into the host structure. The H^+ (and OH^-) ions are known to have a much higher diffusion coefficient than most other ions in aqueous electrolytes due to a special Grotthuss chain-like hopping mechanism.[80] Similarly, if a sufficient amount of water molecules for the solvation of protons is present in the interlayer, it is possible that such fast kinetics could be the result of proton transport *via* fast hopping.[63] Generally H^+ insertion supports much faster (dis)charge rates in Zn-metal batteries that Zn^{2+} insertion (Fig. 10d).

In addition to the vanadium oxide family, polyanionic phosphates can accept H^+ instead of Zn^{2+}. For the $Na_3V_2(PO_4)_2F$ electrode, H^+ works as a guest ion rather that Zn^{2+}.[86] Similarly, reduction also proceeded *via* the co-insertion of Zn^{2+} and H^+ for VPO_4F.[202] This co-insertion reaction was also available in $Na_3V_2(PO_4)_2O_{1.6}F_{1.4}$ in a water-in-bisalt (WIBS) electrolyte.[266] These studies indicate that H^+ insertion occurs in V-containing frameworks among phosphate-based compounds and appears to be linked to the formation of V–O–H bonds.

Further understanding of the charge-storage mechanism in AZIBs requires identification of the inserted number of active ions and determination of how they contribute to the capacity. In other words, what amount of Zn^{2+} and H^+ is inserted into the host materials and how can these amounts be quantified? Several groups have attempted to quantify the H^+ and Zn^{2+} insertion contribution to the overall capacity (Fig. 10e).[63,108,200–203] The studies were performed using vanadium-based oxide and phosphate materials. Usually, the Zn content is measured in discharged samples after washing the byproduct, whereas the

remaining capacity is attributed to the inserted H^+. In work on $VOPO_4F$, in addition to conventional methods, a prompt-gamma neutron activation analysis was used as neutrons interact directly with a nucleus and can give the amount of inserted H^+.[202] According to the literature, the H^+ quantity in most of the studied vanadium compounds is significant, exceeding that of the inserted Zn^{2+} ions. That allows saying that such examples are rather hybrid-ion than Zn-ion batteries.

The reported Zn^{2+} diffusion coefficients are distributed over a broad range from 10^{-15} to 10^{-7} cm^2 s^{-1} (Fig. 10f). Note that the reported values are considerably higher than or comparable to those of Li^+ in nonaqueous LIBs. The Zn^{2+} diffusion accompanied by a two-electron reaction presents such an unexpectedly fast response in AZIBs. Taking into account the mass and charge density of Zn^{2+}, it is not possible to properly explain the reason for the fast diffusion of Zn^{2+} (as high as 10^{-7} cm^2 s^{-1}). Thus, it is most likely that such fast diffusivity can be attributed to the fast H^+ diffusion as Zn^{2+} diffusion progresses rather slowly ($\sim 10^{-11}$–$\sim 10^{-12}$ cm^2 s^{-1}) as measured in nonaqueous ZIBs.[267] Indeed, several studies have confirmed fast diffusion in the case of H^+ intercalation, as shown in Fig. 10f. This tendency clearly supports the charge-compensation process by H^+ and H^+/Zn^{2+} co-insertion in many AZIB materials.

3.1.4. Tracking H^+ (de)insertion. Because hydronium ions (aqueous protons) react with various cathode materials in mildly acidic aqueous electrolytes, monitoring the pH of the electrolyte can be used to trace H^+-related reactions. As pH is a function of H^+ activity, strong change in pH during electrochemical reaction represents a change in the aqueous proton concentration in electrolytes:

$$\mathrm{pH} = -\lg \gamma[\mathrm{H}^+], \tag{10}$$

where $[H^+]$ is the equilibrium concentration of hydronium ions and γ denotes the molar activity coefficient. Inversely, by setting various pH values (*e.g.*, using buffer) during cycling tests, the potential of H^+ (de)insertion in a host material (MO_x) would vary:

$$\mathrm{MO}_x + \mathrm{H}^+ + \mathrm{e}^- = \mathrm{HMO}_x \tag{11}$$

and

$$E = E^\circ + \frac{RT}{F} \ln \frac{\gamma[\mathrm{H}^+] a(\mathrm{MO}_x)}{a(\mathrm{HMO}_x)} \tag{12}$$

Here, E and E° are the electrode potential and standard electrode potential, respectively; $a(MO_x)$ represents the activity of the oxide MO_x; and $a(HMO_x)$ is the activity of the protonated (reduced) form. Eqn (12) is a generalized form of the potential–composition dependence for a solid-state electrochemical reaction involving protons. This equation allows us to check that the reaction of the electrode materials is associated with protons in two directions: measuring changes of pH upon charge–discharge (Fig. 11a, b and e–j) or tracking a pH-triggered shift of potential for the redox process[268] (Fig. 11c and d). The former is suitable for AZIBs, whereas the latter is more common for testing proton batteries or especially for organic redox-active compounds (Fig. 11c).[269] Note that pure Zn^{2+} intercalation does not induce strong pH dependence, as it does not produce H-containing products during the electrochemical reaction.

A study on a $Zn|VO_x$[119] aqueous system demonstrated that the redox peaks shift negatively with the solution pH in accordance with H^+ participation in the reaction (eqn (13) and Fig. 11d):

$$\mathrm{VO}_x + a\mathrm{H}^+ + a\mathrm{e}^- \rightarrow \mathrm{H}_a\mathrm{VO}_x \tag{13}$$

In addition, pH variation of the electrolyte proved the H^+ participation in the electrochemical reaction of MnO_2 electrodes in AZIBs.[45,271]

More often for AZIBs, the H^+ involvement is studied by *operando* pH monitoring, which can be realized using various cell designs (Fig. 11e–g). The simplest design includes a beaker cell or other big-volume cell design[100,270,272–274] with an electrode placed close to one of the electrodes of interest (Fig. 11e and h). This method is quite simple and can be used in most laboratories as pH-sensitive electrodes and pH meters are readily available. Optionally, micro or macro electrodes can be used, and electrolyte convection may be introduced depending on the experimental design. One example is given in Fig. 11h, which shows the pH evolution upon charge–discharge for a $Zn|MnO_2$ cell in a beaker-type cell.

To achieve conditions closer to those of a conventional battery protocol (*i.e.*, a small amount of electrolyte, close-packed cell), several groups have used T-shape cells with a pH-sensitive electrode location either perpendicular to the cathode|anode (Fig. 11f and i)[38] or on the active material side (Fig. 11g and j).[101] Overall, the various designs of pH monitoring provide valuable data when investigating charge-storage mechanisms in AZIBs. The phase change of the active material, associated with proton-assisted reactions and dissolution–precipitation phenomena, can also be monitored by measuring the pH during prolonged electrochemical cycling tests.[274]

E-QCM (Electrochemical quartz crystal microbalance) is a powerful tool for distinguishing the charge carrier in an insertion-type electrode. The QCM principle is based on measuring the changes in frequency of a quartz crystal resonator, which reflects mass changes according to the Sauerbrey equation ($\Delta f = -K\Delta m$), where K is determined by the resonant frequency, density and shear modulus of quartz. In this regard, monitoring Δf during an electrochemical experiment on a metalized quartz-crystal electrode allows extracting mass changes (Fig. 12a). Ideally, the derivative of mass with respect to charge, dm/dq would allow the extraction of molar equivalent mass of the inserted ion, M/z. Hence, various scenarios emerge for a ZIB depending on the active material, electrolyte, and solvent used (Fig. 12b). The solo proton and Zn^{2+} insertion would lead to 1.0 and 32.7 g $mole^{-1}$, respectively. However, intercalation of solvated species would result in higher values, *e.g.* 41.7 for $Zn(H_2O)^{2+}$. Furthermore, the pH-driven deposition of ZBS would lead to a severe mass increase depending on experimental conditions. As it is not a direct electrochemical process but rather one induced by pH change there is no universal theoretical mass increase; the experiment usually shows apparent M/z values ranging between a hundred and several thousand. As we describe below, all these scenarios

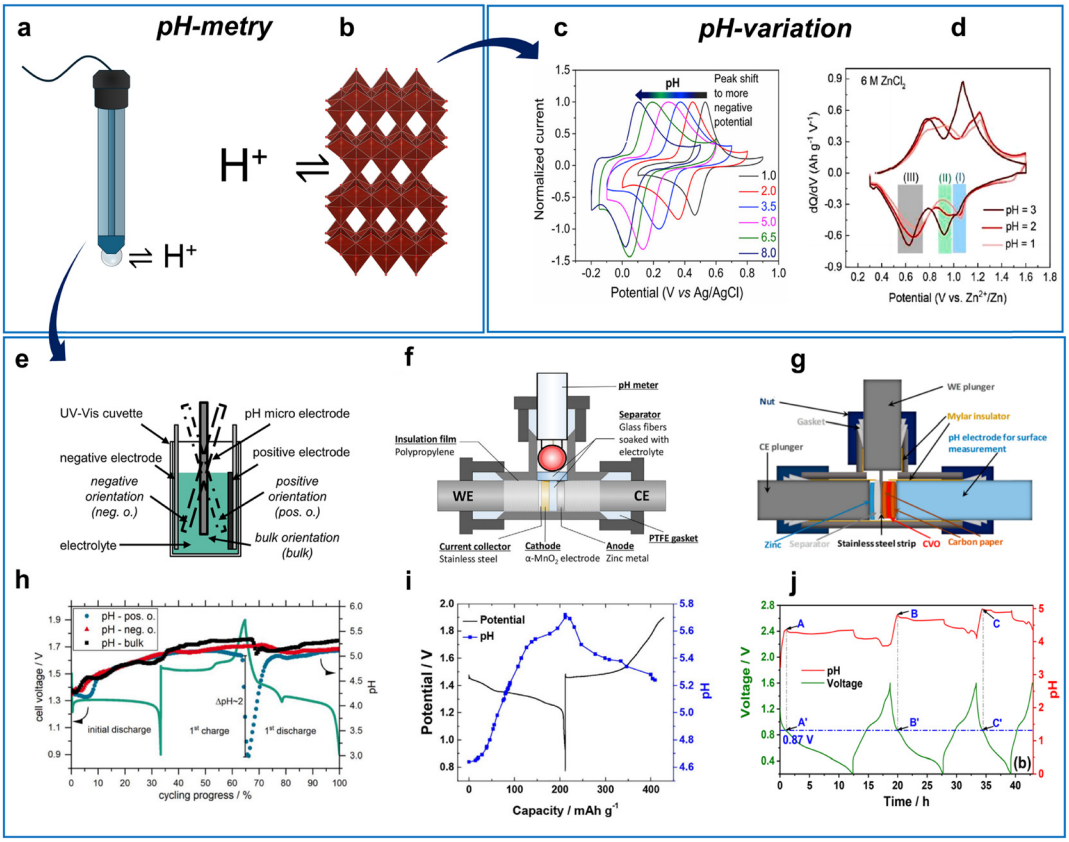

Fig. 11 Study on H^+ participation in AZIBs. (a) Schematic illustration of H^+ exchange at pH electrode membrane and (b), host electrode. (c) pH-dependent voltammetry for H^+ (de)insertion in polymers containing a quinone part. Reproduced with permission from ref. 269. Copyright 2021, Elsevier. (d) pH-dependent differential capacity plots for VO_x in $ZnCl_2$ solutions. Reproduced with permission from ref. 119. Copyright 2021, Elsevier. (e) Cuvette/beaker cell configuration for pH measurements. Reproduced with permission from ref. 270. Copyright 2020, IOP Publishing. (f), (g) T-shape cell configurations for pH measurements with different electrode arrangements. (f) Reproduced with permission from ref. 38. Copyright 2016, John Wiley & Sons. (g) Adapted with permission from ref. 101. Copyright 2020, American Chemical Society. (h) pH evolution in Zn|MnO_2 cell shown in (e). Reproduced with permission from ref. 270. Copyright 2020, IOP Publishing. (i) pH evolution in Zn|MnO_2 cell shown in (f). Reproduced with permission from ref. 38. Copyright 2016, John Wiley & Sons. (j) pH evolution in Zn|V_2O_5 cell shown in (g). Adapted with permission from ref. 101. Copyright 2020, American Chemical Society.

and their simultaneous occurrence (*e.g.*, co-insertion of two species) were reported in the literature.

E-QCM studies were performed for various vanadium oxide-based compounds.[275,277,278] It was found that V_2O_5 undergoes H^+ intercalation followed by precipitation of zinc hydroxy perchlorate $Zn_4(OH)_7ClO_4$ upon discharge, and presumably Zn^{2+} and H^+ co-insertion at lower potentials.[277] In a recent work on a K–Mn–V-oxide ($K_{1.92}Mn_{0.54}V_2O_5{\cdot}H_2O$), the material was tested in both aqueous and nonaqueous Zn^{2+}-electrolytes.[275] The reduction in aqueous electrolyte led to a strong mass increase ($\approx$100–400 g mol^{-1}, Fig. 12c). Such a significant increase, especially at lower potentials, indicated the formation of zinc hydroxide triflate – the event caused by H^+ intercalation or H^+/Zn^{2+} intercalation. What's more interesting is that the experiment performed in acetonitrile-based electrolyte demonstrated values of 29–30 g mol^{-1} – which are quite close to the theoretical desolvated Zn^{2+} intercalation mass (Fig. 12d). Thus, Zn^{2+} was shown to intercalate into the oxide framework, but only in a limited amount – the resulting capacity was $\approx$60 mA h g^{-1} compared to over 300 mA h g^{-1} in aqueous electrolyte. Thus, again, the results support the limited ability of vanadium oxides to store Zn^{2+} ions and highlight the dominant contribution of H^+ as a charge carrier when the electrolyte is an aqueous zinc salt providing protons through Zn^{2+}/H_2O equilibria (hydrolysis).

The most popular ZIB system, Zn–MnO_2, was extensively studied using QCM over the last 4 years.[276,279–282] Every work from this list reported the formation of basic zinc salts, which was evident from the severe mass increase, usually ranging from $\approx$100 g mol^{-1} to several thousand, both during the first and subsequent cycles. Depending on the cycle number and type of MnO_2 used, the ZBS precipitation was caused by material dissolution[276] or H^+/H_3O^+ insertion.[280,281] The ZBS precipitation was usually observed at the lower reduction peak at a curve inflection point (Fig. 12e). The charge led to its dissolution and subsequent deposition of MnO_2, $ZnMn_2O_4$, and $ZnMn_3O_7{\cdot}nH_2O$ as possible re-deposition products. What's interesting, little evidence was collected in such studies towards Zn^{2+} de/insertion, showing the dominant role of protonation and deposition/dissolution chemistry, at least for fresh and slightly cycled electrodes.

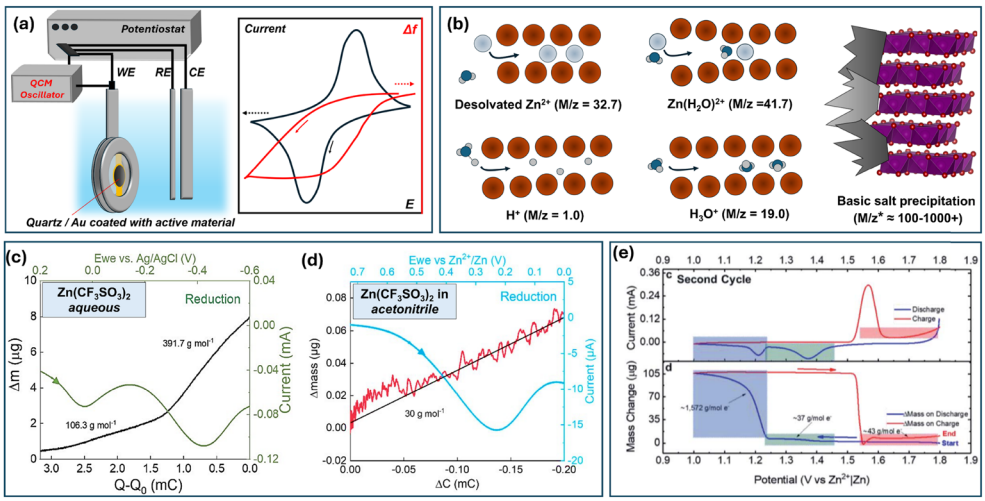

Fig. 12 (a) Schema of an E-QCM experiment with a simple ion-insertion material. (b) Intercalation of various species reported in E-QCM ZIB experiments and ZBS precipitation as processes defining mass changes. Mass changes during reduction of Mn–V-based oxide in (c) aqueous and (d) non-aqueous Zn^{2+}-electrolytes. Adapted with permission from ref. 275. Copyright 2025, John Wiley & Sons. (e) CV and mass change for a MnO_2-based electrode during the 2nd cycle. Adapted with permission from ref. 276. Copyright 2021, Royal Society of Chemistry.

Besides vanadium and manganese oxides, various inorganic and organic compounds were studied. Investigation of Ti_3C_2 MXene revealed that the inserting ion may change depending on electrolyte concentration: 1 M aqueous $ZnCl_2$ electrolyte demonstrated solely Zn^{2+} behavior while using 7 M $ZnCl_2$ led to the co-intercalation of H_3O^+ species due to highly increased acidity of the concentrated electrolyte.[283] Reports on layered TiS_2 hosts showed a high sensitivity of the mechanism to the surface state.[284,285] While TiS_2 was demonstrated to accept hydrated $Zn^{2+}(H_2O)$ species in the interlayer, the creation of a TiO_2–TiS_2 heterostructure promoted desolvation, leading to Zn^{2+} insertion.[284] Another report on TiS_2 demonstrated that exposing (011) facets favors the insertion of H_3O^+ instead of $Zn(H_2O)^{2+}$.[285]

Organic systems, mostly quinone-based were also studied by E-QCM techniques, highlighting Zn^{2+} or Zn^{2+}/H^+ associated charge storage mechanism.[286–288] Interestingly, the poly(benzoquinonyl sulfide) behavior indicated that the triflate anion also participates in the reaction along with Zn^{2+} species.[288] Such behavior should always be taken into account for polymer electrodes, which are much more prone to accepting anions and solvent molecules upon contact with electrolyte solutions and exhibit mixed cationic and anionic transport.[289]

Besides mass monitoring, more information can be gained using EQCM-D (Quartz Crystal Microbalance with Dissipation Monitoring), which helps investigate porous electrodes and viscoelastic properties.[290,291] Overall, the E-QCM is a powerful technique for studying battery electrodes, which require careful analysis. Considering the inserting ions, the analysis should account for the possibility of solvated species (*e.g.*, H_3O^+ and $Zn(H_2O)^{2+}$), anion de/insertion, and water dynamics, as various molecules can be inserted/extracted during an electrochemical process.

3.2. Water- and proton-assisted conversion reactions

Although the field of AZIB research has experienced tremendous growth in recent years, especially in the search for new materials and performance-oriented studies, understanding the reaction mechanisms remains challenging in many cases. This challenge largely stems from the numerous reactions with water, H^+, and OH^-, which often lead to phase changes or unwanted dissolution of the electrode materials. In this section, we discuss the associated structural changes of active materials in AZIBs.

3.2.1. MnO_2: an ongoing debate. Zn|MnO_2 systems were studied for decades as primary and secondary batteries in alkaline and mildly acidic media.[24,292,293] Primary alkaline Zn|MnO_2 cells are well-established commercial products with a large annual production volume. The interest in creating a rechargeable Zn|MnO_2 battery is not surprising; fairly inexpensive MnO_2 has a theoretical capacity of 308 mA h g^{-1} utilizing a one-electron reaction and 616 mA h g^{-1} with a two-electron reaction. Additionally, the variety of MnO_2 polymorphs is attractive for materials design (Fig. 13a).

Interest in AZIBs was retriggered by the study of α-MnO_2 in a mildly acidic zinc electrolyte, for which the Zn|MnO_2 cell using $ZnSO_4$ electrolyte showed stable behavior over 100 cycles,[37] although similar mildly acidic Zn|MnO_2 cells were already demonstrated in 1986.[24] First, it was argued that the reaction mechanism involves (de)introduction of Zn^{2+} from/into the MnO_2 structure (Fig. 13e). Further studies confirmed the incorporation of zinc into γ-MnO_2, revealing various discharge products such as spinel $ZnMn_2O_4$ or layered Zn_yMnO_2 (Fig. 13b).[46] Other studies have proposed (de)insertion of Zn^{2+} ions as the main mechanism for charge storage in $ZnMn_2O_4$ spinels.[215,297]

Later, many studies rationalized that the reaction mechanism is much more complex than a simple (de)intercalation or (de)insertion of Zn^{2+}.[38,44,106,294,295,298,299] Many groups have observed the formation of basic zinc salts (for example, zinc hydroxide on discharged MnO_2 electrodes) and its dissolution upon charging (Fig. 13c).[38,44,106,294,295,298,299] Notably, this observation contradicts the abovementioned simple mechanisms

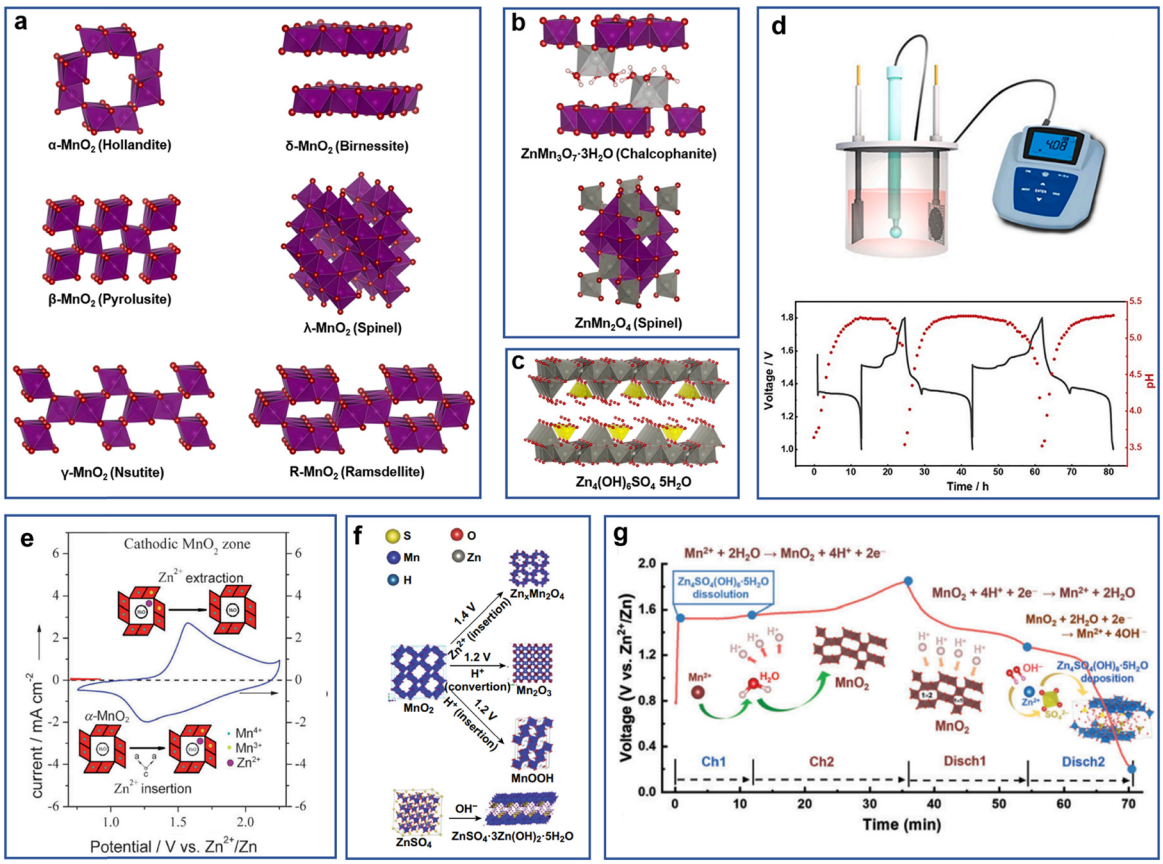

Fig. 13 MnO_2 polymorphs, their conversion products in aqueous ZIBs, and proposed mechanisms. (a) Most typical MnO_2 polymorphs used for ZIB studies. (b) Zn–Mn–O compounds often found after Zn|MnO_2 cycling. (c) Zinc hydroxide sulfate $Zn_4(OH)_6SO_4{\cdot}xH_2O$, a typical discharge by-product. (d) pH changes upon MnO_2 (dis)charge. Reproduced with permission from ref. 294. Copyright 2022, Elsevier. (e) Proposed Zn^{2+} (de)insertion mechanism. Reproduced with permission from ref. 37. Copyright 2011, John Wiley & Sons. (f) Proposed mixed mechanism. Adapted with permission from ref. 295. Copyright 2019, American Chemical Society. (g) Proposed dissolution-deposition mechanism. Reproduced with permission from ref. 296. Copyright 2023, John Wiley & Sons.

because the formation of ZHS and the significant change in pH could not occur if the insertion of Zn^{2+} is the only electrochemical reaction. Therefore, MnO_2-based electrodes consume protons during reduction and then release them upon oxidation. This behavior was measured directly by tracking the pH change during cell operation (Fig. 13d).[38,270,294,300] Various reactions have been proposed to explain the proton consumption: the formation of MnOOH by H^+,[42,295,301] MnO_2/Mn^{2+} deposition/dissolution,[106,294,296,299] and a mixed insertion/deposition/dissolution mechanism.[44,45,298,302–304]

The simplest proton insertion implies the formation of a well-known MnOOH:

$$MnO_2 + H^+ + e^- \rightarrow MnOOH \quad (14)$$

This mechanism was verified by comprehensive studies using HRTEM, XRD, and ^1H NMR analysis.[42,305] Other studies have suggested that co-insertion of Zn^{2+} and H^+ leads to the sequential formation of $ZnMn_2O_4$ and MnOOH depending on the depth of discharge (Fig. 13f).[295,301] However, the formation of MnOOH was not detected, but the H^+ insertion was assumed by the presence of zinc hydroxide sulfate.[104] In addition, the $ZnMn_2O_4$ was found to be irreversibly accumulated on the MnO_2 surface after prolonged cycling.[104]

The fading of capacity in many works was attributed to Mn^{2+}-producing dissolution, particularly caused by disproportionation of manganese in the (+3) state; such as in

$$ZnMn_2O_4 + 4H^+ \rightleftharpoons Zn^{2+} + MnO_2 + Mn^{2+} + 2H_2O \quad (15)$$

To suppress such disproportionation, the additive Mn^{2+} was introduced to the electrolyte, which enabled stable cycling behavior to be achieved in many works.[294,299,306,307] The effect of the Mn^{2+} additive appeared to be more complex: Mn^{2+} is oxidized to form electrodeposited MnO_2 on charge (which is a well-known reaction for industrially produced electrolytic manganese dioxide, EMD):

$$Mn^{2+} + 2H_2O \rightleftharpoons MnO_2 + 4H^+ + 2e^- \quad (16)$$

Other investigations on Zn|MnO_2 cells with different polymorphs demonstrated that the charge storage is dominated by the dissolution–deposition reaction mechanism while (de)intercalation of Zn^{2+} and H^+ has a minor contribution

(Fig. 13g).[296,299] The proposed dissolution–deposition mechanism included:

• Reductive dissolution of MnO_2 (discharge):

$$MnO_2 + 4H^+ + 2e^- \rightarrow Mn^{2+} + 2H_2O \quad (17)$$

• Formation of a basic zinc salt due to decreased H^+ concentration and, consequently, increased OH^- concentration (discharge):

$$4Zn^{2+} + 4H_2O + SO_4^{2-} + 6OH^- \rightarrow Zn_4(OH)_6SO_4{\cdot}4H_2O \quad (18)$$

• MnO_2 deposition in birnessite form (charge):

$$Mn^{2+} + 2H_2O \rightleftharpoons MnO_2\ (\text{birnessite}) + 4H^+ + 2e^- \quad (19)$$

• Dissolution of zinc basic salt due to the generation of H^+ upon MnO_2 electrodeposition:

$$Zn_4(OH)_6SO_4{\cdot}4H_2O + 6H^+ = 4Zn^{2+} + 10H_2O + SO_4^{2-} \quad (20)$$

Thus, pristine MnO_2 material is mainly active during the initial cycles, whereas electrochemical oxidation of Mn^{2+} leads to layered birnessite-type MnO_2, which is spontaneously deposited on the cathode surface. In principle, MnO_2 can be directly electrodeposited in the cell without any initial manganese oxide.[298] It was shown that BZS-based electrodes are available as a precursor to facilitate the *in situ* formation of MnO_2-based electrodes by electrodeposition.[298] The proposed mechanism included two steps during the charge–discharge process: $Mn^{2+} \rightleftharpoons ZnMn_2O_4 \rightleftharpoons$ layered Zn-birnessite.

Operando X-ray absorption near-edge spectroscopy (XANES) and extended X-ray absorption fine structure (EXAFS) studies of α-MnO_2 in three different electrolytes ($ZnSO_4$, $Zn(CF_3SO_3)_2$, and $Zn(CH_3COO_2)$) demonstrated that the reaction mechanism in all three cases is dissolution–deposition rather than (de)intercalation of Zn^{2+}.[106] The reduction induces the formation of Mn^{2+} ions upon discharge, whereas a considerable fraction of MnO_2 remained unreacted. On charge, the dissolved Mn^{2+} is oxidized, although the chemical state is not identical to that of the initial MnO_2 structure but more likely transforms into a layered structure $ZnMn_3O_7{\cdot}3H_2O$. No considerable amount of Mn(III) compounds was detected, which may be the result of disproportionation to Mn^{2+} and Mn^{4+}. Another study by the same group[304] showed extensive investigation of the first cycles of charge–discharge for Zn/α-MnO_2 using *operando* XRD, *operando* XAS, and *ex situ* Raman as well as other methods. They revealed a multi-stage dissolution–conversion charge-storage mechanism, including Zn^{2+} insertion and MnO_2 dissolution/deposition reactions. Namely, the high-voltage plateau was attributed to the conversion of MnO_2 to a poorly crystalline Zn–Mn–O compound with a locally layered structure, whereas the lower-voltage plateau was found to correspond to a proton-consuming MnO_2 dissolution process responsible for BZS deposition.

A recent study on β-MnO_2 using *operando* X-ray techniques (XRD, XAS, and X-ray nano-tomography) revealed several features of the dissolution–deposition mechanism (Fig. 14).[47] It was shown that no new Mn-containing phase was formed

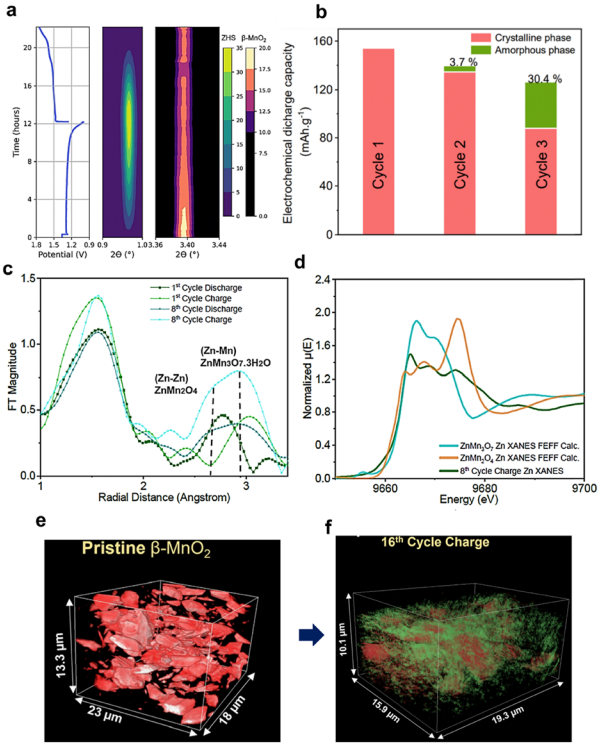

Fig. 14 *Operando* XRD and *ex situ* XAS results of Zn|β-MnO_2 cycling. (a) Discharge–charge profile and corresponding precipitation/dissolution of BZS and fading of MnO_2 peak intensity. (b) Estimated relative capacity contributions by amorphous and crystalline phases. (c) EXAFS analysis (Zn) of charged and discharged states at the 1st and 8th cycles. (d) Comparison of experimental data (8th cycle) and calculated reference spectra for Zn K-edge. (e and f) X-ray synchrotron tomography showing amorphization of MnO_2 after cycling. Reproduced from ref. 47 with permission from the Royal Society of Chemistry. Copyright 2023.

during MnO_2 reduction. The first discharge caused dissolution to Mn^{2+} and ZHS precipitation while maintaining the β-MnO_2 active material (Fig. 14a). The Mn and Zn K-edge XAS results revealed the formation of amorphous Zn–Mn–O compounds such as chalcophanite ($ZnMn_3O_7{\cdot}3H_2O$) and spinel ($ZnMn_2O_4$) structures (Fig. 14b–d).[47]

Amorphization was further supported by 3D synchrotron X-ray nano-tomography data after 16 cycles (Fig. 14e and f.). The results indicated that cyclability is not limited by the initial presence of MnO_2 but is governed by the reversible formation and reaction of Zn–Mn–O compounds through the dissolution–deposition mechanism.

It is likely that the deposition–dissolution of MnO_2 and other manganese phases is dependent on the solvation and adsorption of Mn^{2+} ion, that may explain higher capacity fluctuations in sulfate-based electrolyte than that of triflate-system.[187]

Electrolytic MnO_2 (EMD) has been reported to be an active cathode material for AZIBs, which is enabled by multi-step reactions, including both Zn^{2+} (de)insertion and disproportionation/dissolution reactions.[303] During discharge, EMD was found to form spinel-type $ZnMn_2O_4$ and tunnel-type Zn_xMnO_2; the latter was unstable at a certain state of discharge and disproportionated to Mn^{2+} ions accompanied by an increase

in the pH of the electrolyte triggering the formation of BZS. Interestingly, Mn^{2+} in solution was detected only in the low-voltage region, which is contradictory to the above *operando* study in which Mn^{2+} dissolution was proposed for the entire potential range.[106]

3.2.2. MnO_2: Mechanism generalization. Despite the different reported mechanisms for MnO_2 cathode materials, it is important to note that their electrochemical results are similar for MnO_2 polymorphs, for which the initial conditions are different in terms of particle size, morphology, polymorph, or electrolyte composition (Fig. 15a). This includes the aforementioned double plateau with a specific "inflection point" during discharge and a very similar charge curve. To answer the question of how materials with different structures (layered, tunnel, or close-packed) exhibit similar behavior, several groups conducted comparative studies of MnO_2 polymorphs under long-term cycling conditions.[44–46]

A recent study[44] compared seven types of MnO_2 polymorphs (α-, β-, γ-, ε-, δ-, λ-, and R-MnO_2) over prolonged cycling. The initial discharge capacity showed dispersed data between 40 and 160 mA h g^{-1} for various polymorphs. Some cases exhibited an increase in capacity with cycling, whereas others resulted in fluctuating performance. Regardless of the types of MnO_2, the resulting charge–discharge profiles became identical for the tested MnO_2 polymorphs, with the capacity ranging between 120 and 180 mA h g^{-1} (Fig. 15b). This performance similarity was explained by Mn^{2+} dissolution caused by disproportionation followed by the formation of electrochemically active birnessite. The slow degradation was related to the formation of Mn_3O_4 and barely active $ZnMn_2O_4$ spinel during cycling.

Another study experimentally compared four types of MnO_2 polymorphs (α, β, γ, and δ) in aqueous 1 M $ZnSO_4$ electrolyte.[45] The difference in the charge–discharge behavior was seen only at the first cycle with a single plateau for α- and β-MnO_2 and two plateaus for γ- and δ-MnO_2. Further cycling led to similar behavior and almost identical charge–discharge profiles (Fig. 15a). The specific capacities for all the electrodes were within the range of 200–230 mA h g^{-1}, which is similar to the results of another comparative study.[44] The extensively cycled electrode (200 cycles) clearly showed that $ZnMn_2O_4$ is one of the major reaction products, whereas unreacted initial phases and Mn_2O_3 were also detected as minor products. Moreover, Raman

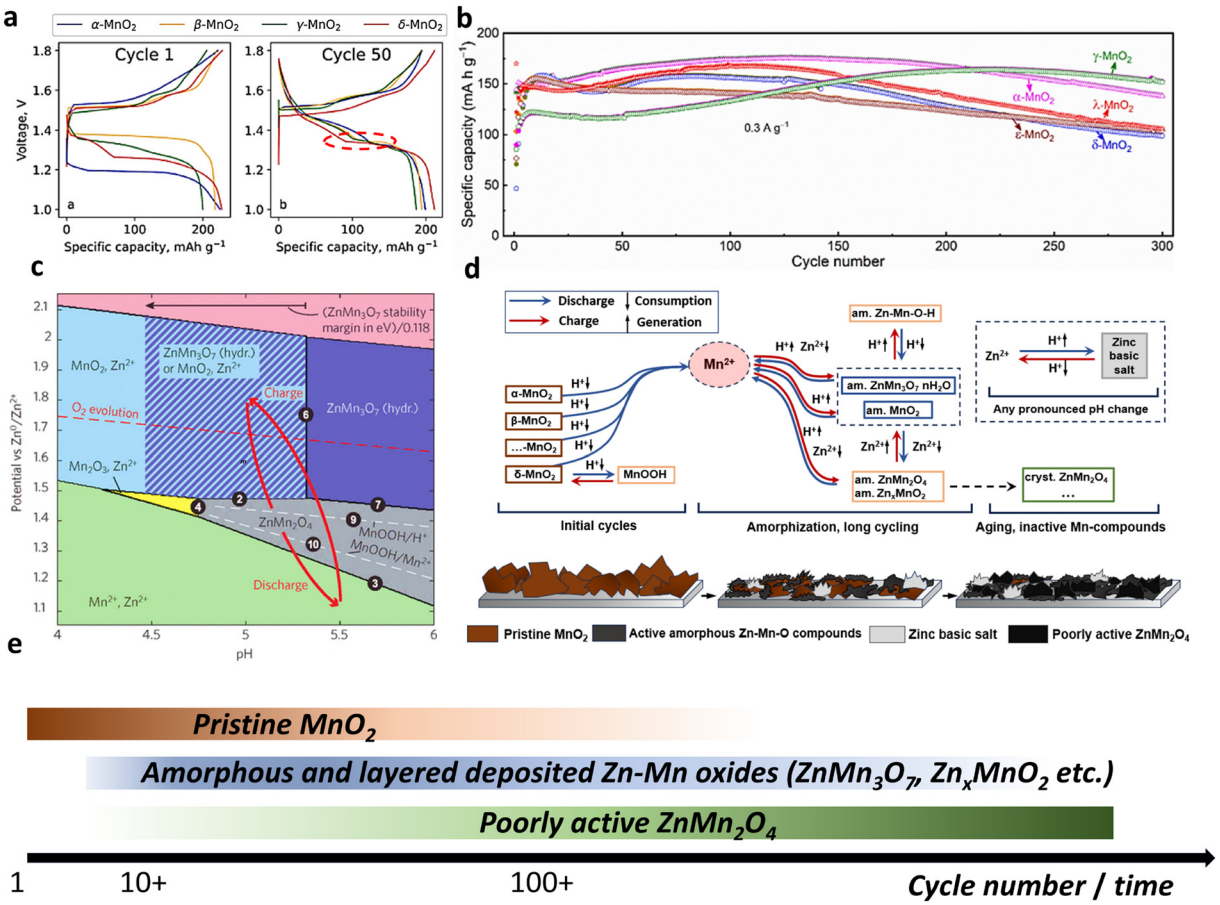

Fig. 15 Behavior of various MnO_2 polymorphs and generalized mechanism of Zn|MnO_2 batteries. (a) Charge–discharge profiles for four different polymorphs at 1st and 50th cycles. Reproduced with permission from ref. 45. Copyright 2022, Elsevier. (b) Long-term cyclability of 5 different polymorphs over 300 cycles. Reproduced with permission from ref. 44. Copyright 2022, Elsevier. (c) Pourbaix diagram for Zn–Mn–O system according to ref. 302. Adapted with permission from ref. 302. Copyright 2022, American Chemical Society. (d) Generalized mechanism of Zn–MnO_2 batteries. (e) Timescale of compounds stability in Zn–MnO_2 cells.

analysis of the cycled electrodes showed a very weak signal or the absence of the initial pristine materials and some broad peaks, suggesting an amorphous MnO_2 deposit on the surface of the cathode. The strong dependence of anodic and cathodic processes on pH revealed the effect of H^+ on charge and discharge, namely, Mn^{3+} disproportion, formation of BZS, and anodic oxidation of Mn^{2+}, all of which are pH-dependent reactions. The similarity in the behavior of various polymorphs was attributed to the gradual dissolution and re-deposition of active materials, leading to a mixture of compounds ($Zn_4(OH)_6SO_4{\cdot}xH_2O$, $ZnMn_2O_4$, Mn_2O_3, amorphous MnO_2, *etc.*). Therefore, regardless of the starting polymorph materials, similar reactions triggered by the participation of H^+ and the formation of similar compounds dominate the overall electrochemical behavior in a mildly acidic aqueous solution.

Recent work has rationalized the aforementioned reactions by building a refined Mn–Zn–H_2O Pourbaix diagram, plotted using both experimental and theoretical data, with a Zn|MnO_2 aqueous cell (Fig. 15c).[302] Namely, the diagram predicts boundaries for Mn(IV)/Mn(III)/Mn(II) transitions depending on the pH. As MnO_2 is reduced, thermodynamics governs the formation of the $ZnMn_2O_4$ spinel in the pH range of 5–6. An alternative form of trivalent manganese, MnOOH, was predicted to have a very narrow stability range. Further reduction of $ZnMn_2O_4$ resulted in pH-dependent dissolution, resulting in the release of aqueous Zn^{2+} and Mn^{2+} ions. As the pH shifted to higher values (>5) due to buffering of BZS, the more stable form of Mn(IV) became hydrated $ZnMn_3O_7$ (chalcophanite), not MnO_2. As a consequence, Mn^{2+} or $ZnMn_2O_4$ is likely to be oxidized to form layered $ZnMn_3O_7$ upon charge. The researchers further validated their postulation by adjusting the pH of the electrolyte to 2.5, which did not result in the formation of chalcophanite, whereas a pH of 4.0 favored $ZnMn_3O_7$ deposition.[302]

To summarize the aforementioned *operando*,[47,106,303,304] comparative,[44–46] and theory-based studies,[103,302] a general understanding of the mechanism for the aqueous Zn|MnO_2 cells appears as follows. The MnO_2 (polymorph) active materials dissolve to form Mn^{2+} upon the first discharge (reaction (17), Fig. 15d). This dissolution is supported by the consumption of protons and, therefore, leads to the formation of basic zinc salts (eqn (18)) almost immediately after the start of discharge.[47,308,309] Although δ-MnO_2 exhibits a slightly different behavior, accepting H^+ to form MnOOH during the initial few cycles,[305] it eventually follows the same tendency as other MnO_2 polymorphs that show dissolution of Mn^{2+}. Thereafter, during the subsequent charge, the Mn^{2+} in the electrolyte solution is oxidized to MnO_2 (reaction (19)). However, the MnO_2 formed after the charge is not the original MnO_2 but amorphous MnO_2 or amorphous layered zinc–manganese oxide. The low-crystalline deposit may vary depending on the conditions and is sometimes referred to as birnessite or, in later studies, as having a structure like layered $ZnMn_3O_7{\cdot}3H_2O$:[47]

$$Zn^{2+} + 3Mn^{2+} + 10H_2O \rightarrow ZnMn_3O_7{\cdot}3H_2O + 14H^+ + 6e^- \quad (21)$$

Some studies indicate that the deposit has a vernadite structure.[310] Depending on the conditions, the low-crystalline deposit is sedimented on the surface of the cathode after several cycles (sometimes tens of cycles), depending on the operation condition of the cells (Fig. 15e).[45,47,106] This activation typically results in two voltage plateaus. In the high-voltage region, for which the BZS is not present, (de)zincification is the main process to form amorphous oxides[103,303,304] such as Zn_xMnO_2 or $ZnMn_2O_4$. As the active material transforms into the new active amorphous deposit, the resulting electrochemical performance is governed by the formed new phases as the new active material, such that the electrode performance becomes, in many cases, independent of the material properties of the original cathode active material. Furthermore, the lower voltage plateau is accompanied by BZS formation, and its deposition appears as an inflection point on the discharge curve ($\approx$1.35 V).[46,309,311] Concurrently with the growth of BZS, the Mn^{2+} concentration increases in the electrolyte,[303,312] which is due to the proton-assisted dissolution of oxide phases to form Mn^{2+}:

$$ZnMn_2O_4 + 8H^+ + 2e^- \rightarrow Zn^{2+} + 2Mn^{2+} + 4H_2O \quad (22)$$

Thus, the insertion of Zn^{2+}/H^+ at higher voltage and deposition/precipitation of Zn–Mn–O phases at the lower voltage plateau are responsible for the charge-storage mechanism of the cycle-induced new cathode active materials. This indicates that the cyclability is limited by the reversibility of the amorphous Zn–Mn–O phase.[47] Eventually, the amorphous phase tends to transform into crystalline $ZnMn_2O_4$, which becomes thermodynamically stable as the pH shifts to higher values during cycling (Fig. 15c).[302,313] Therefore, it is concluded that $ZnMn_2O_4$ accumulation is kinetically sluggish but thermodynamically favorable above pH 5, and the $ZnMn_2O_4$ spinel is a dominant ''dead'' form manganese compound, which impedes capacity retention and is associated with capacity decay.[44,47,313,314]

To summarize, the performance of Zn|MnO_2 cells is determined by (1) the insertion of Zn^{2+}/H^+ into electrochemically deposited amorphous Mn–O or Zn–Mn–O compounds in the high-voltage region and (2) proton-assisted dissolution/deposition involving the Mn^{2+} process in the lower-voltage range. The service life of a positive electrode can be described in three areas: (1) amorphization of the original MnO_2, (2) steady-state cycling, and (3) accumulation of electro-inactive products. Therefore, the electrolyte composition, pH, additives, and the substrate (current collector) appear to be more important for the design and optimization of Zn|MnO_2 and addressing complex amorphization–deposition phenomena in AZIBs than the engineering of MnO_2 crystalline and defect structures.

3.2.3. Transformations of vanadium-based materials. The variety of available oxidation states of vanadium within the electrochemical stability window of water and the rich chemistry of vanadium oxide materials have attracted significant attention for their application toward cathode materials for AZIBs. In addition to the oxide-based systems, the vanadium redox chemistry can be extended to phosphates, chalcogenides,

or Prussian blue analogues to increase the specific capacity. However, many charge or discharge reactions involve interaction with water, which converts the original electrode material into new types of active materials.

Although many metal vanadates are suitable for use as cathode materials for AZIBs, the actual redox-active phase may be different from the original material due to reactions involving an aqueous environment during the initial cycles. Recently, it was reported that oxidation of $K_2V_3O_8$ up to 1.9 V *vs.* Zn^{2+}/Zn led to the formation of amorphous vanadium oxide, presumably V_2O_5 (Fig. 16a).[100] After that, a conversion reaction progressed during discharge, demonstrating a protonation-associated process: $V_2O_5 + 4H^+ + 4e \rightleftharpoons 2VOOH + H_2O$. Another type of V-based oxide, CaV_4O_9, was transformed into amorphous $V_2O_5{\cdot}nH_2O$ after oxidation in a mildly acidic Zn^{2+} electrolyte.[315] The related transformation resulted from the electrochemical displacement of Ca^{2+} ions by water molecules when the cell was charged to 1.6 V.

This tendency, water-associated formation of $V_2O_5{\cdot}nH_2O$ and other vanadium-based oxide materials, is not limited to metal vanadates. Investigation of NASCION-type $Na_3V_2(PO_4)_3$ in aqueous zinc triflate solution demonstrated the formation of V_2O_5, VO_2, and $Zn_3V_2O_8$ upon charge–discharge cycling.[247] This eventually resulted in a decrease in the average charge and discharge voltage as the redox potential of VO_x is lower than that of $Na_3V_2(PO_4)_3$. Interestingly, the use of a highly

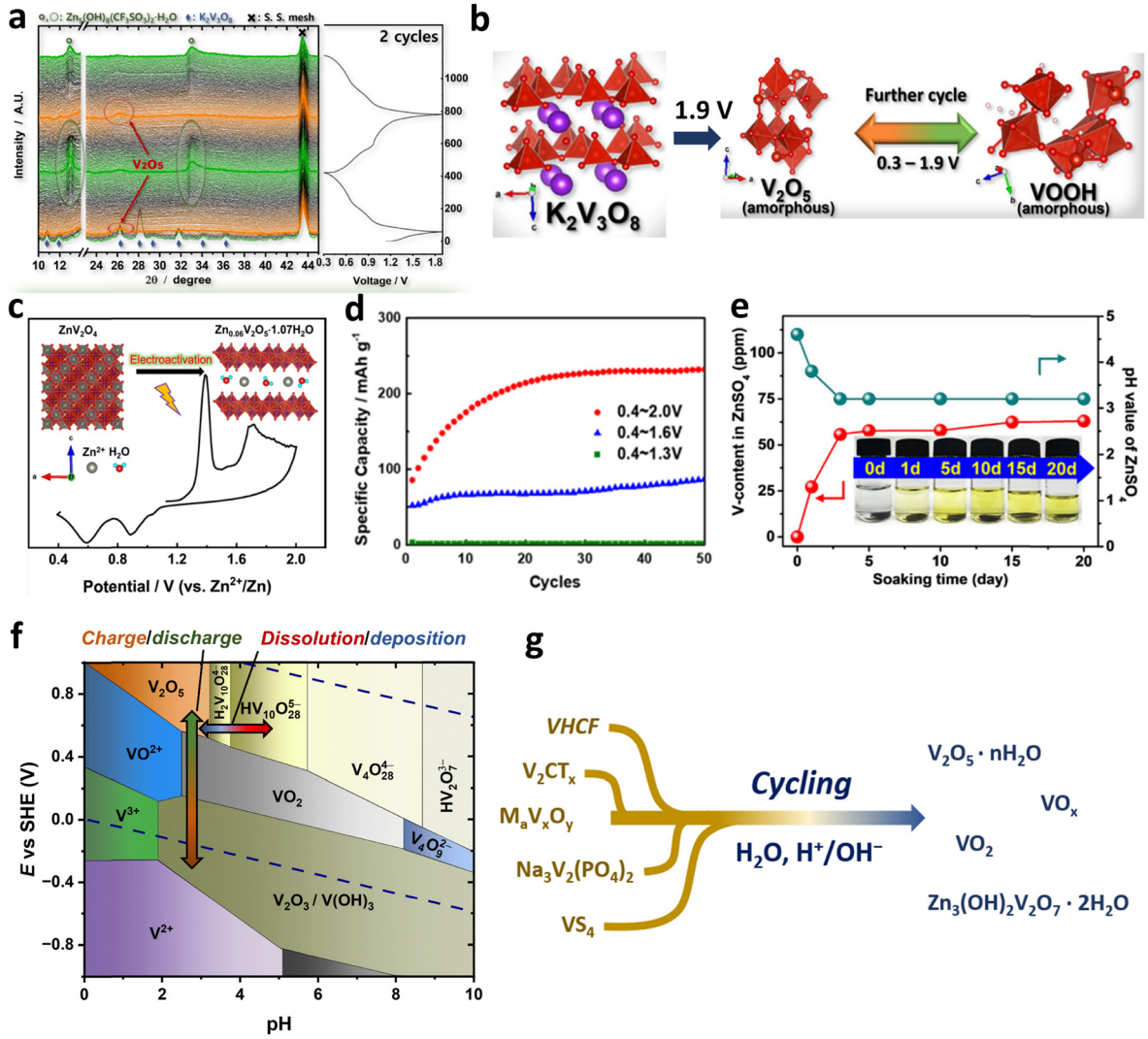

Fig. 16 Transformations of vanadium-based electrodes in aqueous ZIBs. (a) *Operando* XRD of $K_2V_3O_8$-based electrode showing conversion to amorphous V_2O_5 and (b), corresponding schematic representation of proton-associated V_2O_5/VOOH redox upon charge–discharge. Reproduced with permission from ref. 100. Copyright 2023, Elsevier. (c) Electrochemically-driven conversion of ZnV_2O_4 spinel to layered vanadium oxide, Zn-inserted $V_2O_5{\cdot}H_2O$, and (d) corresponding specific capacity increase associated with $ZnV_2O_4/V_2O_5{\cdot}H_2O$ transformation. Adapted with permission from ref. 316. Copyright 2022, American Chemical Society. (e) Vanadium concentration and pH during long term α-V_2O_5 soaking in 2 M $ZnSO_4$. Adapted with permission from ref. 317. Copyright 2021, American Chemical Society (f) Pourbaix diagram for vanadium species, $c(V) = 0.1$ M;[318,319] arrows indicate charge–discharge processes of V_2O_5/VO_x and dissolution/deposition phenomena triggered by pH change. (g) Examples of electrochemical transformation of vanadium-containing electrodes upon charge–discharge in aqueous electrolytes.[247,274,315,316,320–322]

concentrated hybrid electrolyte with sodium ions, 10 M $NaClO_4$ + 0.4 M $Zn(CF_3SO_3)_2$, enabled not only stabilization but also suppressed the decomposition of the electrolyte.

Liu *et al.*[320] demonstrated the formation of nano-sized vanadium oxide (VO_x) during the electrochemical oxidation of V_2C MXene. The VO_x deposit grew on the top of the MXene material, and by controlling the potential, the MXene substrate could be preserved to serve as a 2D conductive layer for the grown nano VO_x. Li *et al.*[321] reported V_2C MXene conversion to V_2O_5 by electrochemical cycling. The conversion eventually increased the capacity, with the phase transition being referred to as ''activation''. Vanadium tetrasulfide (VS_4) was recently found to convert into zinc pyrovanadate ($Zn_3(OH)_2V_2O_7{\cdot}2H_2O$) during the initial charge–discharge cycles.[322] However, unlike the above examples of VO_x formation, the conversion process was associated with an initial discharge involving the reaction with water molecules rather than the charging process. After several cycles, the resulting CV pattern represented two pairs of redox peaks at 0.6 and 1.0 V, which are typically observed for vanadium oxides and vanadate-based compounds.[201,235,263–265]

A spinel compound, ZnV_2O_4, was transformed into Zn-inserted $V_2O_5{\cdot}H_2O$ upon electrochemical oxidation (Fig. 16c).[316] Although the spinel phase was almost inactive, the newly formed vanadium oxide exhibited a prominent increase in capacity up to 230 mA h g^{-1} depending on the potential range used (Fig. 16d).

A phase change associated with water can result not only in a completely different type of material but also in the transformation of one oxide into another. The electrochemical oxidation of VO_2 above 1.4 V (*vs.* Zn^{2+}/Zn) was demonstrated to form $V_2O_5{\cdot}1.75H_2O$ xerogel with a high specific capacity (610 mA h g^{-1} at 0.1 A g^{-1}).[323] The formed $V_2O_5{\cdot}1.75H_2O$ possessed low crystallinity and exhibited a simultaneous H^+ and Zn^{2+} (de)insertion mechanism. As in many previous cases, the transformation was accompanied by water consumption and protolytic reaction:

$$2VO_2 + 2.75H_2O \rightarrow V_2O_5{\cdot}1.75H_2O + 2e^- + 2H^+ \quad (23)$$

Another example is the transformation of α-V_2O_5 to hydrated $V_2O_5{\cdot}1.75H_2O$.[317] The revealed mechanism of the transformation involved the partial dissolution of vanadium oxide to decavanadate $[V_{10}O_{26}(OH)_2]^{4-}$ species in solution, which eventually transformed into $Zn_3(OH)_2V_2O_7{\cdot}2H_2O$ and $V_2O_5{\cdot}1.75H_2O$. The dissolution progressed even without electrochemical treatment, mainly in the first 5 days (Fig. 16e):

$$5V_2O_5 + 3H_2O \rightarrow [V_{10}O_{26}(OH)_2]^{4-} + 4H^+ \quad (24)$$

The formation of VO_x from solution can be used as a tool for electrode construction. Recently, highly disordered electrodeposited vanadium oxide was studied as a cathode material for AZIBs.[324] Electrodeposition was performed using a $VOSO_4$-containing solution in cyclic voltammetry mode, resulting in a highly stable VO_x electrode. The deposit achieved a high areal capacity of 5 mA h cm^{-2} and remarkable stability over 5000 cycles.

In a recent study, vanadium hexacyanoferrate (VHCF) was revealed to undergo phase transformations to zinc hexacyanoferrate and amorphous vanadium oxide VO_x.[274] The intermediate of such transformations was also decavanadate:

$$10\ VO^{2+} + 18H_2O \rightarrow V_{10}O_{27}(OH)^{5-} + 35H^+ + 10e^- \quad (25)$$

Combining all the above examples of phase transformations for vanadium-containing active materials, we can summarize the following common tendencies: (1) vanadium-containing electrodes tend to react with water to form vanadium oxides ($V_2O_5{\cdot}nH_2O$, VO_2, VO_x) or layered $Zn_3(OH)_2V_2O_7{\cdot}2H_2O$ during cycling. Such reactions are usually initiated by extending the charge cutoff voltage (or, more precisely, extending the oxidation state of V to 5^+ on charge). (2) The deposited vanadium oxide (VO_x) often possesses an amorphous/nanosized nature, which makes it difficult to identify formed phases in terms of structure, composition, and chemical states. Usually, the associated reactions are accompanied by changes in pH because water, protons, and hydroxide ions participate in the reaction, which results in the formation of new oxo- and hydroxo-vanadium compounds. (3) Relatively closed-packed phases with vanadium atoms often tend to form open or layered structures. (4) The phase transformation usually progresses through dissolution–precipitation rather than direct solid-state phase transition. The most likely intermediates are decavanadates ions, as the most stable V^{5+} form in mildly acidic media.

The Pourbaix diagram is helpful in understanding such transformations (Fig. 16f) because vanadium tends to dissolve from many materials and form new compounds after reacting with water. This is especially valid for vanadium (+5) compounds: according to the diagram, V_2O_5 is not stable above pH 3.5, where V(+5) forms stable dissolved species. These species are mainly decavanadates because they are thermodynamically favorable for the typical pH of most Zn electrolyte solutions used (pH 3–6). Considering that many electrochemical reactions induce pH change, the cyclic pH variation may create conditions for multiple dissolution–precipitation cycles, eventually contributing to phase transformation and deposition of the $V_2O_5{\cdot}nH_2O$ or some amorphous mixture of oxides. This provides a hint as to why so many completely different V-based materials, in turn, show an almost identical double CV peak shape after cycling, which does not belong to the original cathode material but to newly formed oxides (Fig. 16g). Such behavior is similar to the MnO_2 mechanism when the originally different materials transform into similar mixtures with low-crystalline Zn–Mn–O phases.

Such transformations cannot always be defined as undesirable or favorable. In many cases, such ''activation'' is beneficial for electrochemical performance in terms of capacity and cyclability. In other cases, such as for phosphate compounds, such reactions lower the discharge voltage and degrade the stability and must be suppressed to achieve stable behavior.[247]

4. Generalized transformations of transition-metal active materials

As follows from the consideration of the electrochemistry of manganese oxides and vanadium-containing compounds in aqueous zinc electrolytes, many proton-activated reactions

occur in an aqueous environment, including various precipitation–dissolution phenomena. Analysis of the available literature indicates that such phenomena are not limited to the aforementioned compounds but include other manganese materials such as phosphates or hexacyanoferrates and cobalt-and nickel-containing materials (Fig. 17a).[325–332] For instance, as vanadium hexacyanoferrate (VHCF) transforms into VO_x and ZnHCF upon cycling,[274] manganese hexacyanoferrate particularly transforms in MnO_x, as evident from the Raman signal accompanied by the appearance of MnO_2-related features on discharge curves.[332] Manganese phosphates[327,331] have been shown to decompose during charge–discharge, producing a MnO_2 layer on the electrode surface. Interestingly, cycling was used deliberately to create an appropriate surface oxide layer with enhanced performance in a recent work.[331]

Cobalt and nickel compounds, mostly chalcogenides, have been extensively studied as electrodes in AZIBs and Zn hybrid batteries, often using alkaline electrolytes.[325–330,335,336] Similar to MnO_x and VO_x generated from Mn- and V-containing materials, cobalt and nickel materials result in $CoOOH/Co(OH)_2$ and $NoOOH/Ni(OH)_2$ acting as redox-active materials for proton storage.[328–330]

Thus, there are obvious similarities in the behavior of many transition-metal-based materials in AZIBs caused by the transformation of the original into new redox-active species. The general transformation for most transition-metal-containing compounds consists of several steps (Fig. 17b). The transition-metal ion (M^{n+}) is leached due to the non-zero solubility of the active material into the solution or due to electrode polarization (oxidation or reduction). For V-ion compounds, the intermediate ions are likely decavanadates ($V_{10}O_{26}(OH)_2^{4-}/V_{10}O_{27}(OH)^{5-}$), whereas for Mn-, Co-, and Ni- containing materials, it would be Mn^{2+}, Co^{2+}, and Ni^{2+}.

Then, metal ions interact with water, resulting in hydroxide or oxide formation. Depending on the potential, concentration, and pH, the deposition would proceed *via* a chemical or electrochemical route, generating a new oxide- or hydroxide-based compound, often in amorphous form. The chemical route may correspond to a hydrolysis reaction, *e.g.*:

$$V_{10}O_{27}(OH)^{5-} + 2H_2O = 5V_2O_5 \downarrow + 5OH^- \quad (26)$$

The electrochemical route would be electrochemical oxidation as for the deposition of MnO_2, $ZnMn_2O_4$, or Co/Ni hydroxides:

$$Co^{2+} + 2H_2O = CoOOH + e^- + 3H^+ \quad (27)$$

As such reactions include the participation of protons or hydroxide ions, the possibility and rate are highly dependent on

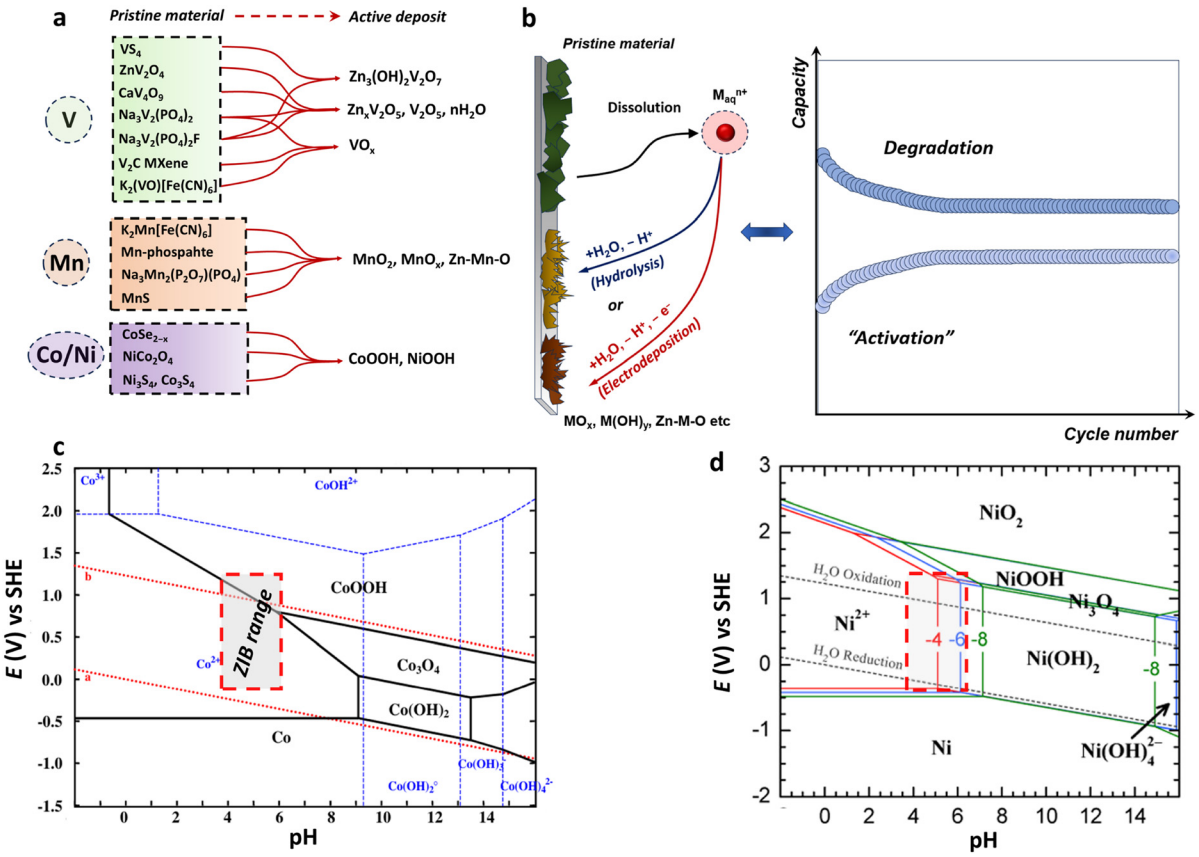

Fig. 17 Transformations of transition metal-based materials in aqueous zinc batteries. (a) Examples of electrode material transformation into new electroactive compounds upon battery operation or prior to testing.[247,274,315,316,320–322,325–331] (b) Generalized scheme of transformation as dissolution-deposition process and corresponding degradation or activation behavior. (c) Co-H_2O Pourbaix diagram. Reproduced with permission from ref. 333. Copyright 2008, Elsevier. (d) Ni-H_2O Pourbaix diagram. Adapted with permission from ref. 334. Copyright 2017, American Chemical Society.

pH, especially the local pH, which may vary during cycling. In addition, the dissolution–precipitation process depends on the solubility of the species, which, in turn, can be affected by the electrolyte concentration (*e.g.*, by salting out in highly concentrated electrolytes). Thus, dissolution can be slowed down, and redeposition can occur directly on the surface of the active material, which is called ''activation'' (Fig. 17b). The case of dissolution without deposition on the current collector or carbon would lead to capacity decay. Therefore, it is of great importance to study the active material after cycling in case there is any evidence of ''activation'', which, in combination with CV or voltage-shape changes, can be indicators of the phase-transformation phenomena.

In the simplest way, the deposit is formed according to the Pourbaix diagram. As seen for manganese (Fig. 15c), vanadium (Fig. 16f), cobalt (Fig. 17c), and nickel (Fig. 17d), the operation range of AZIBs overlaps with various oxide/hydroxide deposition regions. Hence, the new deposits start acting as electroactive materials, which are available only when they are deposited on the conductive part of the cell. The precise compositions of deposits may differ from the predicted M–H_2O diagram because the presence of Zn^{2+} ions may be favorable for Zn-metal-oxide formation such as in the case of manganese-oxide phases. Nevertheless, the understanding of their formation through dissolution–precipitation routes appears to be general for most activation phenomena in the literature.

We suppose that the general driving force behind such activation–redeposition–amorphization phenomena is the thermodynamic stability of oxide- and hydroxide-based phases with strong M–O bonds compared to phosphates, hexacyanoferrates, and similar complex compounds. Water, which easily participates in many reactions and provides H^+ due to ionic equilibria, acts as a reagent and a mediator of such transitions. We should note that a vast number of studies on activation phenomena lack analysis of extensively cycled electrodes and electrolytes, and hence, the redeposition and formation of oxides upon initial activation are extremely underreported in the literature and often are not properly studied in performance-oriented publications. The examples shown in Fig. 17a cover only a limited number of reported phenomena.

Another conclusion, which we draw from the considered literature, is the limited possibility for creating multiple redox centers in a single framework to boost zinc storage, such as an approach to increase the specific capacity of Prussian blue analogues by adding cobalt or vanadium atoms to the lattice. The specific capacity can indeed be increased *via* so-called activation;[241] however, that increase is a result of phase separation[274] due to proton- and water-assisted reactions in which at least two distinct phases and not two redox ''sites'' of one framework act as active materials. Thus, instead of zinc storage, proton storage occurs in the deposited oxide or hydroxide. It should be noted that the activation phenomena of various electrodes in various cases are not entirely detrimental for achieving high capacity and good cyclability. More detailed investigation of the cycled electrode is necessary to critically determine which processes represent ''activation'' and what is the real active material after many cycles. Because the discussed process requires water, it is of high interest to compare the behavior of AZIBs with that of their nonaqueous counterparts, where redeposition phenomena are prohibited or limited.

5. Key differences between aqueous and non-aqueous ZIBs

One of the main advantages of nonaqueous systems is the applicability of a broader electrochemical stability window, which is also available for ZIBs. Thus, many organic solvents allow high-voltage cathodes, and, more importantly, the stability of the Zn anode is secured by eliminating the parasitic HER. A comparison of the appearance of a Zn electrode in $Zn(OTf)_2$/DMSO electrolyte and $ZnSO_4/H_2O$ electrolyte after 100 cycles of deposition–stripping is shown in Fig. 18a and b.[337] Multiple cycling (or long conditioning) of zinc metal in conventional aqueous zinc sulfate solution results in H_2 evolution, and the DMSO-based electrolyte ensures stable behavior. Such an electrolyte was employed in Zn|δ-MnO_2 batteries, showing good capacity retention for 1000 cycles.[337] Although the HER on Zn is relatively slow, the resulting rate is critical for aqueous cell swelling and failure (Fig. 18c). Li *et al.*[338] compared the behavior of $K_{1.6}Mn_{1.2}Fe(CN)_6$ (MnHCF) in aqueous $Zn(ClO_4)_2$ and TEGDME (tetraethylene glycol dimethyl ether)-based electrolytes (Fig. 18d and e). The tetraglyme-based cell enabled evidently better cyclability and capacity retention, allowing thousands of cycles.

Regarding cathodes, non-aqueous electrolytes usually result in moderate capacities of approximately 50–150 mA h g^{-1} (Fig. 18f–h), which is far lower than the values obtained in aqueous systems. For instance, various studies on MnO_2[31,337,341] revealed a smooth discharge profile without inflection, delivering a specific capacity in the range of 60–160 mA h g^{-1}. This result is not surprising, as the abovementioned complex H_2O-assisted dissolution–redeposition–amorphization phenomena are not available for nonaqueous Zn|MnO_2 cells.

The difference between charge-storage ability using aqueous and nonaqueous electrolytes is much more strongly pronounced for vanadium oxides (Fig. 19a–c). For instance, Fig. 19a shows dis/charge profiles of the cathode material, δ-V_2O_5, in aqueous and acetonitrile-based electrolytes, with the capacity in the latter being only ≈25 mA h g^{-1} *vs.* 300–350 mA h g^{-1} for the aqueous cell. Such results are similar to those of the abovementioned E-QCM study on nonaqueous electrolyte, where switching from H^+ or H^+/Zn^{2+} co-insertion to Zn^{2+} insertion in a nonaqueous system reduced the available capacity from ≈300 to 40 mA h g^{-1}.[275] Numerous vanadium oxides and metal vanadates are known to have capacities in the range of 300–450 mA h g^{-1} in AZIBs.[99] However, there are only a few studies on nonaqueous ZIBs with vanadium oxides, with the capacity usually not exceeding ~200 mA h g^{-1}. To explain this gap, first, for general reasons, we must consider (a) kinetic limitations (interface charge transfer or solid-state diffusion) (Fig. 19d) or thermodynamic/structure limitation (the ability to store Zn^{2+} ions).

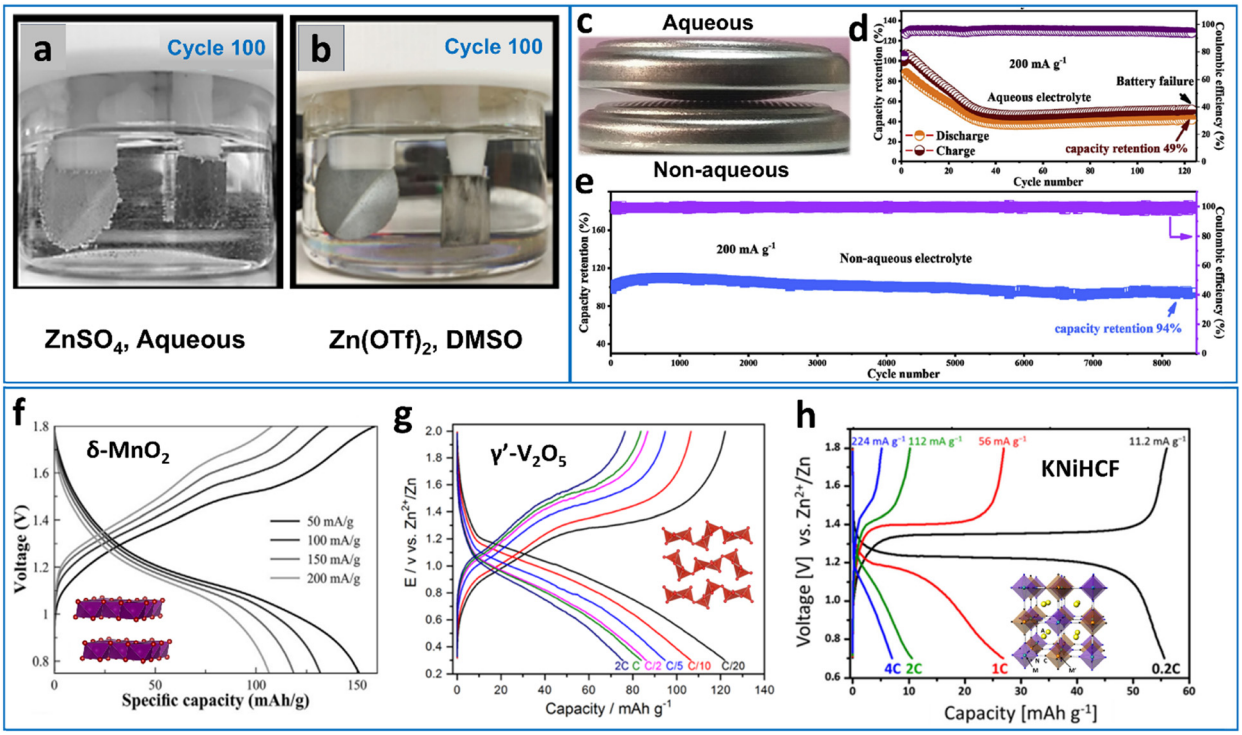

Fig. 18 Non-aqueous ZIBs. Hydrogen evolution after 100 cycles for (a) 2 M $ZnSO_4/H_2O$ and (b) 0.25 M $Zn(OTf)_2$/DMSO. Reproduced with permission from ref. 337. Copyright 2021, Elsevier. (c) Zn|KMnFeHCF cells after cycling using $Zn(ClO_4)_2$ aqueous- and tetraglyme-based electrolyte and corresponding cyclability plots for (d), aqueous and (e), nonaqueous electrolyte. Reproduced with permission from ref. 338. Copyright 2020, Elsevier. Charge–discharge profiles for nonaqueous ZIBs using (f) δ-MnO_2. Reproduced with permission from ref. 337. Copyright 2021, Elsevier. (g) γ′-V_2O_5 Adapted with permission from ref. 339. Copyright 2022, American Chemical Society. (h) KNiHCF Reproduced with permission from ref. 340. Copyright 2017, Elsevier.

Kundu *et al.*[32] studied $V_3O_7{\cdot}H_2O$ electrodes in both aqueous and nonaqueous electrolytes using *operando* XRD and electrochemical impedance spectroscopy (EIS) at various temperatures. Although they observed solid-solution-like changes in the XRD patterns for both electrolytes, the nonaqueous electrolyte allowed a capacity of only ~60 mA h g^{-1}, surprisingly lower than that obtained in the aqueous system (~375 mA h g^{-1}). A large difference in the activation energy of the interfacial charge transfer (19.47 kJ mol^{-1} in H_2O *vs.* 75.34 kJ mol^{-1} in CH_3CN) was proposed as evidence of the desolvation limitation at the interface which is the limiting factor for the nonaqueous Zn-ion storage.

In contrast, several studies have decisively shown that H^+ (arising from Zn^{2+}/H_2O electrolyte) did contribute to the capacity along with Zn^{2+}. For instance, Liu *et al.*[101] comprehensively studied δ-V_2O_5 ($Ca_{0.34}V_2O_5$) using XRD in both aqueous $Zn(OTf)_2$, nonaqueous CH_3CN-based $Zn(OTf)_2$ electrolyte, and aqueous H_2SO_4 solution. Both Zn^{2+} and H^+ were shown to be introduced *via* a solid-solution pathway. In addition, pH monitoring revealed Zn^{2+}/H^+ co-insertion behavior with a Zn^{2+}/H^+ exchange feature implying that at some potentials, Zn^{2+} intercalation can cause H^+ deintercalation and *vice versa*. A recent study on pH monitoring in V_2O_5 has supported the co-insertion of H^+ and Zn^{2+}, where the H^+ contribution strongly depends on the pH of the electrolyte.[64] Additionally, a large number of AZIB articles showing high capacities of vanadium oxide and few reports on nonaqueous ZIBs with acceptable properties indirectly support the capacity being boosted by proton (co)insertion in AZIBs and moderate or limited ability to store Zn^{2+} ions in a VO_x host for nonaqueous electrolytes (Fig. 19c).

Manganese- and vanadium-based oxide compounds are not the only material families that behave differently in nonaqueous media. Metal phosphates were found to be inferior in nonaqueous electrolytes, as reported for sodium vanadium fluoride phosphate and layered $VOPO_4$[86,342] (Fig. 19b and c). Park and Manthiram[86] found that the guest ion is H^+ rather than Zn^{2+} in $Na_3V_2(PO_4)_2F_3$, which explains the low capacity in nonaqueous cells, similar to the behavior of vanadium oxides. From this viewpoint, phosphate-based compounds need to be further investigated to clarify the reaction mechanism in nonaqueous ZIBs.

In contrast to metal oxides, metal hexacyanoferrates and metal sulfides demonstrate comparable charge-storage ability in both aqueous and nonaqueous solutions (Fig. 19c). As discussed earlier, metal hexacyanoferrates (MHCFs) have been actively studied in AZIBs with capacities reaching ~60–100 mAh g^{-1}.[238–243] The use of nonaqueous electrolytes usually results in capacities of 50–90 mA h g^{-1},[28,338,340,343] which are close to the values obtained in MHCF-based AZIBs. Such relatively low values are explained by the high molecular weight of the MHCF formula unit, rationalizing the delivery of capacity of 80–90 mA h g^{-1} provided the only Fe redox pair is active. Although some MHCFs were shown to overcome the one-electron limit in aqueous media by introducing

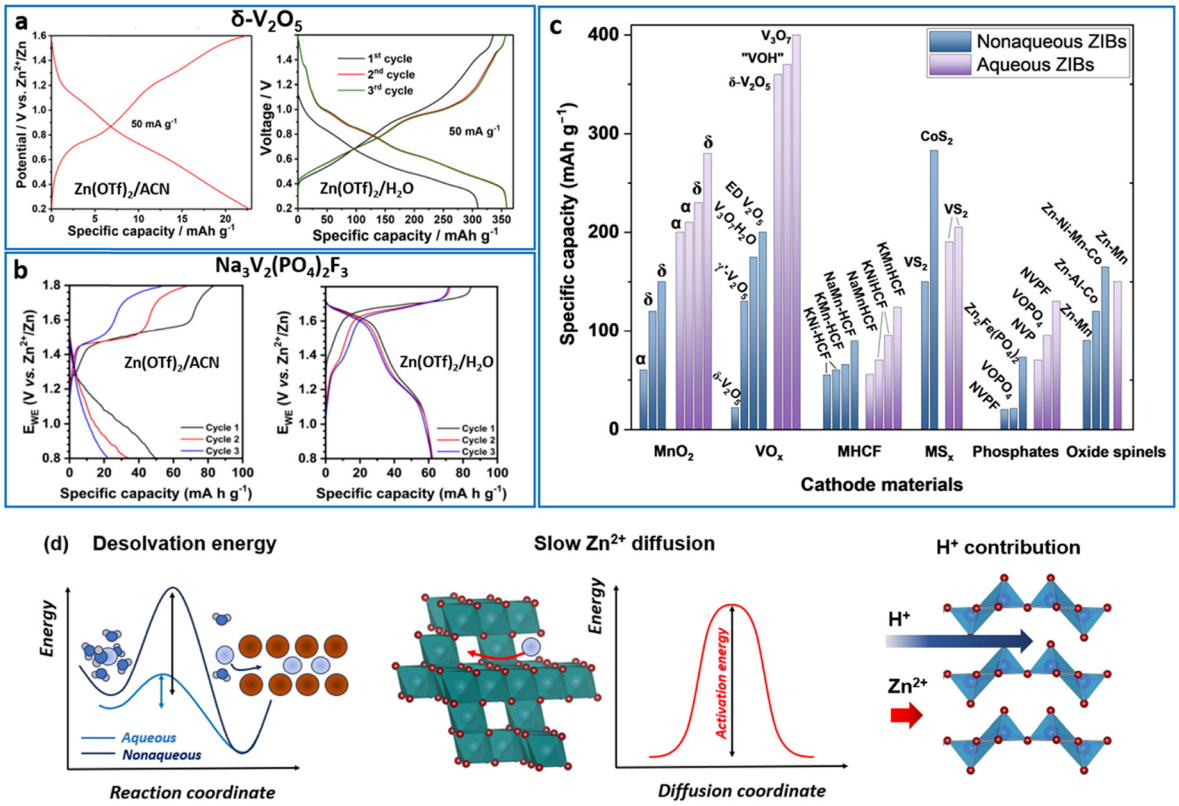

Fig. 19 Aqueous *vs.* non-aqueous ZIBs. (a) Voltage profiles of δ-V_2O_5 in acetonitrile and water-based electrolytes. Adapted with permission from ref. 101. Copyright 2020, American Chemical Society. (b) Voltage profiles of $Na_3V_2(PO_4)_2F_3$ in acetonitrile and water-based electrolytes. Adapted with permission from ref. 86. Copyright 2020, American Chemical Society. (c) Specific capacities achieved for different material families in nonaqueous and aqueous electrolytes.[28–32,41,45,86,101,106,199,215,229,246,332,337–352] (d) Different reasons for inferior charge storage in nonaqueous ZIBs.

Co[353] or V[241] in the HCF framework, the true reason for such activation is most likely associated with phase separation and formation of oxides due to reactions with water.[274,332] As such reactions are prohibited in nonaqueous media, overcoming the theoretical limit of ~90 mA h g^{-1} for nonaqueous MHCF-based ZIBs is hardly achievable.

Metal sulfides, in contrast to metal oxides, have demonstrated high and comparable capacities both in aqueous and organic-based electrolytes[344,345,351,352] (Fig. 19c). Zhang *et al.*[345] demonstrated a prominent capacity of 283 mA h g^{-1} for CoS_2 in $Zn(OTf)_2$/acetonitrile electrolyte. The capacity was achieved not by cobalt but by sulfide/disulfide anionic redox. No XRD peak shift was observed, whereas irreversible changes in the structure were detected from Zn^{2+} intercalation into the electrode material, likely leading to a poorly crystalline new phase. The other group used 0.5 M $Zn(OTf)_2$/TMP electrolyte that enabled a long-lasting Zn|VS_2 cell with a capacity of ~140 mA h g^{-1}.[344] The structural analysis indicated irreversible changes occurring along with Zn^{2+} insertion/extraction, as evidenced by XRD. As the work was primarily focused on optimizing Zn electrode|electrolyte stability, no detailed information on the VS_2 redox type was provided. The (de)intercalation behavior of Zn^{2+} was suggested in aqueous Zn|VS_2 batteries by observing reversible shifts in XRD patterns and other analyses.[352] The capacity did not greatly exceed the observed values in the nonaqueous system[344] with minor or no proton contribution to the VS_2/Zn^{2+} electrochemistry.

Finally, oxide spinel compounds have been reported as promising cathode materials for both aqueous and nonaqueous ZIBs both in terms of capacity and high operation voltage.[30,199,215] This finding appears to be in disagreement with the degradation phenomena in the aqueous Zn|MnO_2 system, for which the capacity of the cell fades concurrently with the formation of the $ZnMn_2O_4$ phase and Zn–Mn–O spinel that are poorly active. On the other hand, Zhang *et al.*[215] used non-stoichiometric $ZnMn_2O_4$ spinel with Mn deficiency in the lattice in aqueous zinc triflate electrolyte. Interestingly, unlike for most MnO_2 polymorphs, a double-plateau discharge profile, typical for dissolution–redeposition MnO_2 phenomena, was not observed. The same electrode also demonstrated a moderate capacity (90 mA h g^{-1}) in an acetonitrile-based electrolyte. Another group reported nonaqueous ZIBs using $ZnAl_xCo_{2-x}O_4$[30] and $ZnNi_xMn_xCo_{2-2x}O_4$[199] spinels. Using $ZnAl_xCo_{2-x}O_4$ allowed a capacity of 120 mA h g^{-1} at 0.1C in a $Zn(OTf)_2$ solution in acetonitrile. The Zn–Ni–Mn–Co spinel was shown to have an even higher capacity, reaching ~180 mA h g^{-1}, enabled by Ni and Co redox pairs. Both systems demonstrated some issues with the CE being ~90%–95% even after 100 cycles. An amine base additive, 200 ppm of 1,4-diazabicyclo [2.2.2]octane (DABCO), was used for Zn–Ni–Mn–Co spinel to make it feasible by suppressing electrolyte oxidation.[199]

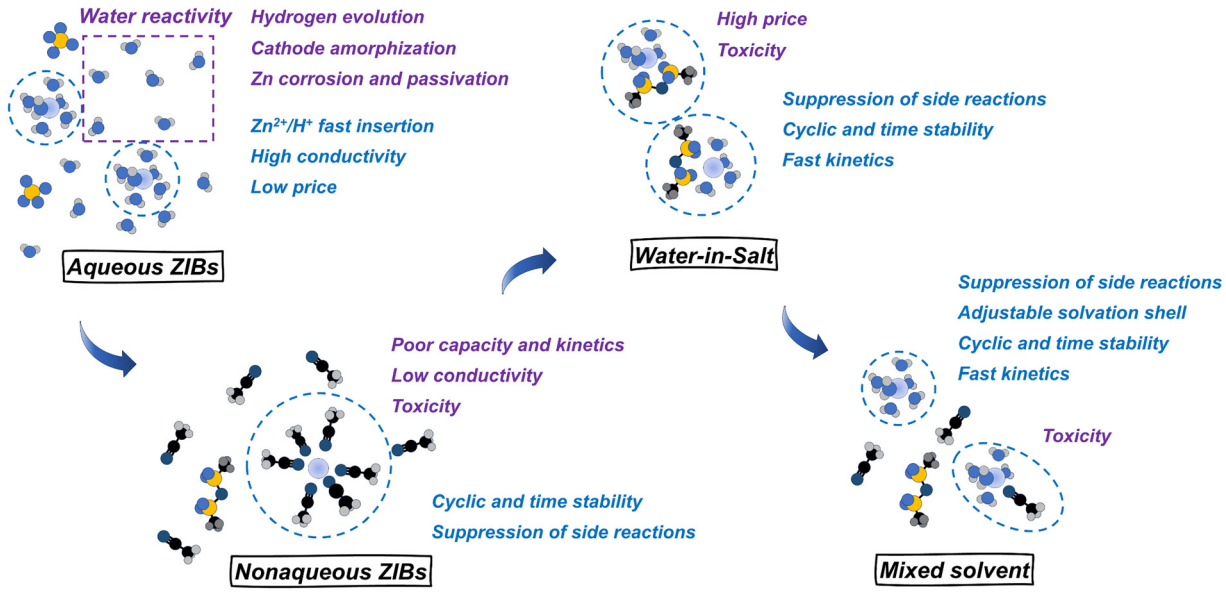

Fig. 20 Research development on rechargeable Zn-ion batteries electrolytes.

However, despite the high potential and reasonable capacity in reported spinel work, this direction for nonaqueous ZIBs has not yet gained much attention and development. In addition to composition and defect management, all the aforementioned studies have addressed nanoparticle materials (12–20 nm for Zn–Mn, 10–25 nm for Zn–Al–Co, and 10–100 nm Zn–Ni–Mn–Co). The Zn–Al–Co and Zn–Ni–Mn–Co spinels were prepared by citric sol–gel technique, whereas the nano-sized $ZnMn_2O_4$/C spinel composite was obtained by ammonia-induced Zn^{2+}, Mn^{2+} precipitation followed by 180 °C heating. Exploiting even 50-nm small $ZnMn_2O_4$ particles could achieve only ~30 mA h g^{-1} because of the slow Zn^{2+} diffusion into the spinel structure. For spinel oxides to be active in nonaqueous ZIBs, several factors should be treated and optimized thoroughly: the use of an appropriate synthetic route to obtain nanomaterials with a high surface area and particle size not exceeding 30–50 nm to overcome slow divalent diffusion limitation; the use of composites with nanocarbon to mitigate conductivity and interparticle contact issues; and finding an appropriate electrolyte or electrolyte additive to suppress side reactions at high potentials.

In summary, various types of materials behave differently in aqueous and non-aqueous ZIBs (Fig. 19c and d). The oxide- and phosphate-based materials possess obviously inferior charge-storage ability towards Zn^{2+} compared to H^+, which is the reason for the typically poor performance in nonaqueous electrolytes. In addition, kinetic reasons such as lower desolvation energy or higher diffusion rates boost high capacities in such frameworks in aqueous environments. Finally, the ability of water to accept or donate protons and dissolve various species enables deposition–dissolution reactions. In contrast, some metal sulfides, metal hexacyanoferrates, and spinels show similar capacities both in aqueous and non-aqueous electrolytes and demonstrate the ability to accept Zn^{2+}; however, much more elaboration is required to improve the long-term electrode performance.

6. Conclusions and perspective

The role of water in AZIBs is much deeper and more complex than merely acting as a highly polar solvent. As has been intensively studied in the last few years, water is involved in many processes at the cathode and anode. Some of these processes are useful for achieving high performance of AZIBs, whereas others are harmful.

The beneficial processes include capacity boosting by H^+ intercalation or co-intercalation in vanadium-oxide electrodes and the high-capacity deposition–dissolution chemistry of MnO_2-Mn^{2+}, which is supported by Zn^{2+}-H_2O acid–base chemistry. From one point of view, Zn^{2+}-H_2O equilibria enable versatile ion-hybrid batteries with dual Zn^{2+}/H^+ roles. For this reason, aqueous zinc-ion batteries outperform their nonaqueous counterparts as well as Ca- and Mg-ion batteries, which are difficult to work with. However, the high water activity and low potential stability window are responsible for many undesirable reactions, such as zinc corrosion, which limits battery life and stimulates dendrite formation, dissolution of cathode materials, and amorphization.

Thus, there lies a question: which direction of ZIB development is beneficial in terms of battery performance and which direction of research is crucial for process understanding? For practice, one would desire to merge the high capacities and promising kinetics/power of AZIBs with the high stability and absence of various side reactions of non-aqueous ZIBs. Thus, various approaches to control the water activity[354] may be used when selecting the appropriate electrolyte (Fig. 20).

A well-known approach for decreasing the water activity and decelerating and suppressing side reactions is using highly concentrated water-in-salt electrolytes.[355] Although such systems show promising performance, their scalability and applicability remain unclear as the salts used are usually expensive and the use of high concentrations raises price and toxicity issues. Another approach involves the use of mixed solvents, *e.g.*, (H_2O-PC); here, water enables hydration or some proton-donating properties beneficial for kinetics; however, its low concentration and interaction with an organic co-solvent decreases the activity and eliminates many harmful side reactions.[35,36,146,147,174] The potential downside of such a system might be organic solvent toxicity but, eventually, it would depend on the solvent type used.

From the applied science view, we propose that the combined solvent approach holds the most promise, such as the use of organic-aqueous based mixed electrolytes to limit water activity and suppress corrosion and other undesired processes while benefiting from the H_2O-driven capacity boost by H^+-intercalation or H_2O-solvated Zn^{2+} intercalation. At the same time, the mixed solvent-based electrolyte is inherently less expensive than WiS electrolyte due to the use of reasonable amounts of salts. From a fundamental perspective, studies on AZIBs require a broader use of research approaches and studies related to dissolved species and dissolution–deposition processes, particularly extensive use of UV-vis spectroscopy and *operando* pH monitoring. Due to the highly dynamic oxide–hydroxide chemistry, amorphization processes should be studied in detail, and comprehensive post-cycled electrode characterization is needed to identify the real active phase(s) and understand the cycling mechanism for prolonged cycling.

Author contributions

Yauhen Aniskevich: writing – original draft, visualization, validation, methodology, investigation, formal analysis, data curation, conceptualization. Seung-Taek Myung: writing – review & editing, validation, methodology, investigation, funding acquisition, data curation, conceptualization.

Data availability

No primary research results, software or code have been included and no new data were generated or analysed as part of this review.

Conflicts of interest

There are no conflicts to declare.

Acknowledgements

This research was supported by the International Research & Development Program of the National Research Foundation of Korea (NRF) funded by the Ministry of Science and ICT of Korea (NRF-2020R1A6A1A03043435, NRF-2022M3H4A1A04096478, NRF-2023R1A2C2003210, and NRF-2022H1D3A2A02092011).

References

1 Y. Liang, C. Z. Zhao, H. Yuan, Y. Chen, W. Zhang, J. Q. Huang, D. Yu, Y. Liu, M. M. Titirici, Y. L. Chueh, H. Yu and Q. Zhang, *InfoMat*, 2019, **1**, 6–32.
2 Z. Zhu, T. Jiang, M. Ali, Y. Meng, Y. Jin, Y. Cui and W. Chen, *Chem. Rev.*, 2022, **122**, 16610–16751.
3 M. Walter, M. V. Kovalenko and K. V. Kravchyk, *New J. Chem.*, 2020, **44**, 1677–1683.
4 J. W. Choi and D. Aurbach, *Nat. Rev. Mater.*, 2016, **1**, 1–16.
5 Y. Liang, H. Dong, D. Aurbach and Y. Yao, *Nat. Energy*, 2020, **5**, 646–656.
6 J. Y. Hwang, S. T. Myung and Y. K. Sun, *Chem. Soc. Rev.*, 2017, **46**, 3529–3614.
7 N. Yabuuchi, K. Kubota, M. Dahbi and S. Komaba, *Chem. Rev.*, 2014, **114**, 11636–11682.
8 S. W. Kim, D. H. Seo, X. Ma, G. Ceder and K. Kang, *Adv. Energy Mater.*, 2012, **2**, 710–721.
9 K. Kubota, M. Dahbi, T. Hosaka, S. Kumakura and S. Komaba, *Chem. Record*, 2018, **18**, 459–479.
10 T. Hosaka, K. Kubota, A. S. Hameed and S. Komaba, *Chem. Rev.*, 2020, **120**, 6358–6466.
11 M. A. Schroeder, L. Ma, G. Pastel and K. Xu, *Curr. Opin. Electrochem.*, 2021, **29**, 100819.
12 P. Canepa, G. Sai Gautam, D. C. Hannah, R. Malik, M. Liu, K. G. Gallagher, K. A. Persson and G. Ceder, *Chem. Rev.*, 2017, **117**, 4287–4341.
13 R. Y. Wang, B. Shyam, K. H. Stone, J. N. Weker, M. Pasta, H. W. Lee, M. F. Toney and Y. Cui, *Adv. Energy Mater.*, 2015, **5**, 1401869.
14 M. M. Huie, D. C. Bock, E. S. Takeuchi, A. C. Marschilok and K. J. Takeuchi, *Coord. Chem. Rev.*, 2015, **287**, 15–27.
15 M. E. Arroyo-De Dompablo, A. Ponrouch, P. Johansson and M. R. Palacín, *Chem. Rev.*, 2020, **120**, 6331–6357.
16 G. A. Elia, K. V. Kravchyk, M. V. Kovalenko, J. Chacón, A. Holland and R. G. A. Wills, *J. Power Sources*, 2021, **481**, 228870.
17 L. E. Blanc, D. Kundu and L. F. Nazar, *Joule*, 2020, **4**, 771–799.
18 N. Zhang, X. Chen, M. Yu, Z. Niu, F. Cheng and J. Chen, *Chem. Soc. Rev.*, 2020, **49**, 4203–4219.
19 X. Jia, C. Liu, Z. G. Neale, J. Yang and G. Cao, *Chem. Rev.*, 2020, **120**, 7795–7866.
20 Q. Li, J. Zhang, L. Zhong, F. Geng, Y. Tao, C. Geng, S. Li, B. Hu and Q. H. Yang, *Adv. Energy Mater.*, 2022, **12**, 2201734.
21 Y. Aniskevich, J. H. Yu, J. Y. Kim, S. Komaba and S. T. Myung, *Adv. Energy Mater.*, 2024, **14**, 2304300.
22 B. Yong, D. Ma, Y. Wang, H. Mi, C. He and P. Zhang, *Adv. Energy Mater.*, 2020, **10**, 2002354.
23 Y. Shang and D. Kundu, *Curr. Opin. Electrochem.*, 2022, **33**, 100954.

24 T. Yamamoto and T. Shoji, *Inorg. Chim. Acta*, 1986, **117**, L27–L28.
25 E. Gocke, W. Schramm, P. Dolscheid and R. Schöllhorn, *J. Solid State Chem.*, 1987, **70**, 71–81.
26 N. S. Venkata Narayanan, B. V. Ashokraj and S. Sampath, *J. Colloid Interface Sci.*, 2010, **342**, 505–512.
27 T. J. Simons, M. Salsamendi, P. C. Howlett, M. Forsyth, D. R. Macfarlane and C. Pozo-Gonzalo, *ChemElectroChem*, 2015, **2**, 2071–2078.
28 A. L. Lipson, S. D. Han, S. Kim, B. Pan, N. Sa, C. Liao, T. T. Fister, A. K. Burrell, J. T. Vaughey and B. J. Ingram, *J. Power Sources*, 2016, **325**, 646–652.
29 P. Senguttuvan, S. D. Han, S. Kim, A. L. Lipson, S. Tepavcevic, T. T. Fister, I. D. Bloom, A. K. Burrell and C. S. Johnson, *Adv. Energy Mater.*, 2016, **6**, 1600826.
30 C. Pan, R. G. Nuzzo and A. A. Gewirth, *Chem. Mater.*, 2017, **29**, 9351–9359.
31 S. D. Han, S. Kim, D. Li, V. Petkov, H. D. Yoo, P. J. Phillips, H. Wang, J. J. Kim, K. L. More, B. Key, R. F. Klie, J. Cabana, V. R. Stamenkovic, T. T. Fister, N. M. Markovic, A. K. Burrell, S. Tepavcevic and J. T. Vaughey, *Chem. Mater.*, 2017, **29**, 4874–4884.
32 D. Kundu, S. Hosseini Vajargah, L. Wan, B. Adams, D. Prendergast and L. F. Nazar, *Energy Environ. Sci.*, 2018, **11**, 881–892.
33 H. Qiu, X. Du, J. Zhao, Y. Wang, J. Ju, Z. Chen, Z. Hu, D. Yan, X. Zhou and G. Cui, *Nat. Commun.*, 2019, **10**, 5374.
34 J.-Q. Huang, X. Guo, X. Lin, Y. Zhu and B. Zhang, *Research*, 2019, **2019**, 2635310.
35 Y. Dong, L. Miao, G. Ma, S. Di, Y. Wang, L. Wang, J. Xu and N. Zhang, *Chem. Sci.*, 2021, **12**, 5843–5852.
36 C. Li, R. Kingsbury, A. S. Thind, A. Shyamsunder, T. T. Fister, R. F. Klie, K. A. Persson and L. F. Nazar, *Nat. Commun.*, 2023, **14**, 3067.
37 C. Xu, B. Li, H. Du and F. Kang, *Angew. Chem.*, 2012, **124**, 957–959.
38 B. Lee, H. R. Seo, H. R. Lee, C. S. Yoon, J. H. Kim, K. Y. Chung, B. W. Cho and S. H. Oh, *ChemSusChem*, 2016, **9**, 2948–2956.
39 R. Trócoli and F. L. Mantia, *ChemSusChem*, 2015, **8**, 481–485.
40 D. Kundu, B. D. Adams, V. Duffort, S. H. Vajargah and L. F. Nazar, *Nat. Energy*, 2016, **1**, 16119.
41 G. Li, Z. Yang, Y. Jiang, C. Jin, W. Huang, X. Ding and Y. Huang, *Nano Energy*, 2016, **25**, 211–217.
42 H. Pan, Y. Shao, P. Yan, Y. Cheng, K. S. Han, Z. Nie, C. Wang, J. Yang, X. Li, P. Bhattacharya, K. T. Mueller and J. Liu, *Nat. Energy*, 2016, **1**, 16039.
43 F. Wang, O. Borodin, T. Gao, X. Fan, W. Sun, F. Han, A. Faraone, J. A. Dura, K. Xu and C. Wang, *Nat. Mater.*, 2018, **17**, 543–549.
44 Y. Liao, H. C. Chen, C. Yang, R. Liu, Z. Peng, H. Cao and K. Wang, *Energy Storage Mater.*, 2022, **44**, 508–516.
45 U. Siamionau, Y. Aniskevich, A. Mazanik, O. Kokits, G. Ragoisha, J. H. Jo, S. T. Myung and E. Streltsov, *J. Power Sources*, 2022, **523**, 231023.
46 B. Sambandam, V. Mathew, S. Kim, S. Lee, S. Kim, J. Y. Hwang, H. J. Fan and J. Kim, *Chem*, 2022, **8**, 924–946.
47 V. R. Kankanallu, X. Zheng, D. Leschev, N. Zmich, C. Clark, C. H. Lin, H. Zhong, S. Ghose, A. M. Kiss, D. Nykypanchuk, E. Stavitski, E. S. Takeuchi, A. C. Marschilok, K. J. Takeuchi, J. Bai, M. Ge and Y. C. K. Chen-Wiegart, *Energy Environ. Sci.*, 2023, **16**, 2464–2482.
48 H. Alt, H. Binder, G. Klempert, A. Köhling and G. Sandstede, *J. Appl. Electrochem.*, 1972, **2**, 193–200.
49 H. Alt, H. Binder, A. Köhling and G. Sandstede, *Electrochim. Acta*, 1972, **17**, 873–887.
50 A. G. Macdiarmid, S.-L. Mu, N. L. D. Somasiri and W. Wu, *Mol. Cryst. Liq. Cryst.*, 1985, **121**, 187–190.
51 K. Koshika, N. Sano, K. Oyaizu and H. Nishide, *Chem. Commun.*, 2009, 836–838.
52 K. Koshika, N. Sano, K. Oyaizu and H. Nishide, *Macromol. Chem. Phys.*, 2009, **210**, 1989–1995.
53 Q. Zhao, W. Huang, Z. Luo, L. Liu, Y. Lu, Y. Li, L. Li, J. Hu, H. Ma and J. Chen, *Sci. Adv.*, 2018, **4**, eaao1761.
54 Z. Guo, Y. Uanyuan Ma, X. Dong, J. Ianhang Huang, Y. Onggang Wang and Y. Xia, *Angew. Chem.*, 2018, **130**, 11911–11915.
55 Z. Song, L. Miao, H. Duan, L. Ruhlmann, Y. Lv, D. Zhu, L. Li, L. Gan and M. Liu, *Angew. Chem., Int. Ed.*, 2022, **61**, e202208821.
56 Z. Li, J. Tan, Y. Wang, C. Gao, Y. Wang, M. Ye and J. Shen, *Energy Environ. Sci.*, 2023, **16**, 2398–2431.
57 J. Cui, Z. Guo, J. Yi, X. Liu, K. Wu, P. Liang, Q. Li, Y. Liu, Y. Wang, Y. Xia and J. Zhang, *ChemSusChem*, 2020, **13**, 2160–2185.
58 V. Verma, S. Kumar, W. Manalastas and M. Srinivasan, *ACS Energy Lett.*, 2021, **6**, 1773–1785.
59 X. Ji and L. F. Nazar, *Nat. Sustainability*, 2024, **7**, 98–99.
60 M. Li, Z. Li, X. Wang, J. Meng, X. Liu, B. Wu, C. Han and L. Mai, *Energy Environ. Sci.*, 2021, **14**, 3796–3839.
61 C. Nie, G. Wang, D. Wang, M. Wang, X. Gao, Z. Bai, N. Wang, J. Yang, Z. Xing and S. Dou, *Adv. Energy Mater.*, 2023, **13**, 2300606.
62 A. Bayaguud, Y. Fu and C. Zhu, *J. Energy Chem.*, 2022, **64**, 246–262.
63 L. Wang, J. Yan, Y. Hong, Z. Yu, J. Chen and J. Zheng, *Sci. Adv.*, 2023, **9**, eadf4589.
64 C. Lee, Y. Hong, D. Kim, Y. Lim, J. W. Choi and S. Chung, *Adv. Funct. Mater.*, 2023, **33**, 2303763.
65 J. H. Jo, Y. Aniskevich, J. Kim, J. U. Choi, H. J. Kim, Y. H. Jung, D. Ahn, T. Y. Jeon, K. S. Lee, S. H. Song, H. Kim, G. Ragoisha, A. Mazanik, E. Streltsov and S. T. Myung, *Adv. Energy Mater.*, 2020, **10**, 2001595.
66 J. Shin, J. Lee, Y. Park and J. W. Choi, *Chem. Sci.*, 2020, **11**, 2028–2044.
67 X. Zhang, J. P. Hu, N. Fu, W. Bin Zhou, B. Liu, Q. Deng and X. W. Wu, *InfoMat*, 2022, **4**, e12306.
68 H. J. Kim, S. Kim, K. Heo, J.-H. Lim, H. Yashiro, S.-T. Myung, H. J. Kim, S. Kim, K. Heo, S.-T. Myung, J.-H. Lim and H. Yashiro, *Adv. Energy Mater.*, 2023, **13**, 2203189.

69 V. Mathew, B. Sambandam, S. Kim, S. Kim, S. Park, S. Lee, M. H. Alfaruqi, V. Soundharrajan, S. Islam, D. Y. Putro, J. Y. Hwang, Y. K. Sun and J. Kim, *ACS Energy Lett.*, 2020, **5**, 2376–2400.
70 J. O. Bockris, Z. Nagy and D. Drazic, *J. Electrochem. Soc.*, 1973, **120**, 30.
71 M. Schlesinger and M. Paunovic, *Modern Electroplating: Fifth Edition*, John Wiley and Sons, 2010.
72 N. Sorour, W. Zhang, E. Ghali and G. Houlachi, *Hydrometallurgy*, 2017, **171**, 320–332.
73 Y. D. Gamburg and G. Zangari, *Theory and Practice of Metal Electrodeposition*, Springer, New York, 2011.
74 A. Agnew and R. Paterson, *J. Chem. Soc., Faraday Trans. 1*, 1978, **74**, 2885–2895.
75 J. T. Hinatsu, V. D. Tran and F. R. Foulkes, *J. Appl. Electrochem.*, 1992, **22**, 215–223.
76 S. D. Han, N. N. Rajput, X. Qu, B. Pan, M. He, M. S. Ferrandon, C. Liao, K. A. Persson and A. K. Burrell, *ACS Appl. Mater. Interfaces*, 2016, **8**, 3021–3031.
77 Y. Zhang and M. Muhammed, *Hydrometallurgy*, 2001, **60**, 215–236.
78 C. Liu, X. Xie, B. Lu, J. Zhou and S. Liang, *ACS Energy Lett.*, 2021, **6**, 1015–1033.
79 C. Jana, G. Ohanessian and C. Clavaguéra, *Theor. Chem. Acc.*, 2016, **135**, 141.
80 P. Vanysek, *CRC Hand Book Chem. Phys.*, 1993, 5–92.
81 A. Moezzi, A. McDonagh, A. Dowd and M. Cortie, *Inorg. Chem.*, 2013, **52**, 95–102.
82 S. Cousy, N. Gorodylova, L. Svoboda and J. Zelenka, *Chem. Pap.*, 2017, **71**, 2325–2334.
83 A. Moezzi, M. Cortie and A. M. McDonagh, *Eur. J. Inorg. Chem.*, 2013, 1326–1335.
84 A. Moezzi, M. B. Cortie and A. M. McDonagh, *Dalton Trans.*, 2013, **42**, 14432–14437.
85 C. S. Cordeiro, G. G. C. Arizaga, L. P. Ramos and F. Wypych, *Catal. Commun.*, 2008, **9**, 2140–2143.
86 M. J. Park and A. Manthiram, *ACS Appl. Energy Mater.*, 2020, **3**, 5015–5023.
87 B. Beverskog and I. Puigdomenech, *Corros. Sci.*, 1997, **39**, 107–114.
88 H. L. Clever, M. E. Derrick and S. A. Johnson, *J. Phys. Chem. Ref. Data*, 1992, **21**, 941–1004.
89 X. Wang, J. Li, G. K. Das, S. Johanie, C. Vernon and R. Shaw, *J. Solid State Chem.*, 2020, **290**, 121483.
90 M. Ohnishi, I. Kusachi and S. Kobayashi, *Can. Mineral.*, 2007, **45**, 1511–1517.
91 F. C. Hawthorne and E. Sokolova, *Can. Mineral.*, 2002, **40**, 939–946.
92 L. A. Groat, *Am. Mineral.*, 1996, **81**, 238–243.
93 A. Gordeeva, Y. J. Hsu, I. Z. Jenei, P. H. B. Brant Carvalho, S. I. Simak, O. Andersson and U. Haüssermann, *ACS Omega*, 2020, **5**, 17617–17627.
94 L. S. Germann, R. E. Dinnebier, X. Liu, Y. Dong and W. Li, *Z. Anorg. Allg. Chem.*, 2016, **642**, 255–259.
95 N. Thomas and M. Rajamathi, *J. Colloid Interface Sci.*, 2011, **362**, 493–496.
96 T. Biswick, W. Jones, A. Pacuła and E. Serwicka, *J. Solid State Chem.*, 2006, **179**, 49–55.
97 A. Ziba, A. Pacuła, E. M. Serwicka and A. Drelinkiewicz, *Fuel*, 2010, **89**, 1961–1972.
98 M. Liu, P. Wang, W. Zhang, H. He, G. He, S. Xu, L. Yao and T. S. Miller, *Energy Storage Mater.*, 2024, **67**, 103248.
99 J. Ding, H. Gao, D. Ji, K. Zhao, S. Wang and F. Cheng, *J. Mater. Chem. A*, 2021, **9**, 5258–5275.
100 H. J. Kim, J. H. Jo, J. Y. Kim, J. Jeong, J. H. Park, H. G. Jung, K. Y. Chung, M. G. Kim, N. Lee, K. S. Sohn, Y. Aniskevich, E. Streltsov and S. T. Myung, *Energy Storage Mater.*, 2023, **55**, 105–116.
101 X. Liu, H. Euchner, M. Zarrabeitia, X. Gao, G. A. Elia, A. Groß and S. Passerini, *ACS Energy Lett.*, 2020, **5**, 2979–2986.
102 P. Oberholzer, E. Tervoort, A. Bouzid, A. Pasquarello and D. Kundu, *ACS Appl. Mater. Interfaces*, 2019, **11**, 674–682.
103 N. J. Herrmann, H. Euchner, A. Groß and B. Horstmann, *Adv. Energy Mater.*, 2024, **14**, 2302553.
104 X. Gao, H. Wu, W. Li, Y. Tian, Y. Zhang, H. Wu, L. Yang, G. Zou, H. Hou and X. Ji, *Small*, 2020, **16**, 1905842.
105 Z. Tang, W. Chen, Z. Lyu and Q. Chen, *Energy Mater. Adv.*, 2022, **2022**, 9765710.
106 D. Wu, L. M. Housel, S. T. King, Z. R. Mansley, N. Sadique, Y. Zhu, L. Ma, S. N. Ehrlich, H. Zhong, E. S. Takeuchi, A. C. Marschilok, D. C. Bock, L. Wang and K. J. Takeuchi, *J. Am. Chem. Soc.*, 2022, **144**, 23405–23420.
107 S. Deng, Z. Tie, F. Yue, H. Cao, M. Yao and Z. Niu, *Angew. Chem., Int. Ed.*, 2022, **134**, e202115877.
108 F. Wan, L. Zhang, X. Dai, X. Wang, Z. Niu and J. Chen, *Nat. Commun.*, 2018, **9**, 1656.
109 G. Singh, C. R. Tang, A. Nicoll, J. Torres, L. M. Housel, L. Wang, K. J. Takeuchi, E. S. Takeuchi and A. C. Marschilok, *J. Phys. Chem. C*, 2023, **127**, 3940–3951.
110 C. Wang, S. Wei, S. Chen, D. Cao and L. Song, *Small Methods*, 2019, **3**, 1900495.
111 M. Tamilselvan, T. V. M. Sreekanth, K. Yoo and J. Kim, *J. Ind. Eng. Chem.*, 2021, **93**, 176–185.
112 Y. Dong, M. Jia, Y. Wang, J. Xu, Y. Liu, L. Jiao and N. Zhang, *ACS Appl. Energy Mater.*, 2020, **3**, 11183–11192.
113 J. S. Park, J. H. Jo, Y. Aniskevich, A. Bakavets, G. Ragoisha, E. Streltsov, J. Kim and S. T. Myung, *Chem. Mater.*, 2018, **30**, 6777–6787.
114 Z. Li, S. Ganapathy, Y. Xu, Z. Zhou, M. Sarilar and M. Wagemaker, *Adv. Energy Mater.*, 2019, **9**, 1900237.
115 L. A. Hernandez-Alvarado, L. S. Hernandez, J. M. Miranda and O. Dominguez, *Anti-Corros. Methods Mater.*, 2009, **56**, 114–120.
116 L. Zhang, I. A. Rodríguez-Pérez, H. Jiang, C. Zhang, D. P. Leonard, Q. Guo, W. Wang, S. Han, L. Wang and X. Ji, *Adv. Funct. Mater.*, 2019, **29**, 1902653.
117 L. Li, S. Liu, W. Liu, D. Ba, W. Liu, Q. Gui, Y. Chen, Z. Hu, Y. Li and J. Liu, *Nanomicro Lett.*, 2021, **13**, 34.
118 M. Cui, N. Ma, H. Lei, Y. Liu, W. Ling, S. Chen, J. Wang, H. Li, Z. Li, J. Fan and Y. Huang, *Angew. Chem., Int. Ed.*, 2023, **62**, e202303845.

119 Q. Pan, R. Dong, H. Lv, X. Sun, Y. Song and X. X. Liu, *Chem. Eng. J.*, 2021, **419**, 129491.
120 Q. Cui, K. Yu, N. Zhang and Z. Zhu, *Appl. Surf. Sci.*, 2008, **254**, 3517–3521.
121 P. Yu, J. Wang, X. Gan, Z. Guo, L. Huang and Z. Song, *Batter Supercaps*, 2023, **6**, e202300010.
122 W. Sun, V. Küpers, F. Wang, P. Bieker and M. Winter, *Angew. Chem., Int. Ed.*, 2022, **61**, e202207353.
123 X. Liu, Q. Han, Q. Ma, Y. Wang and C. Liu, *Small*, 2022, **18**, 2203327.
124 X. Liu, G. Xu, Q. Zhang, S. Huang, L. Li, X. Wei, J. Cao, L. Yang and P. K. Chu, *J. Power Sources*, 2020, **463**, 228223.
125 R. A. Robinson and R. S. Jones, *J. Am. Chem. Soc.*, 1936, **58**, 959–961.
126 R. H. Stokes and B. J. Levien, *J. Am. Chem. Soc.*, 1946, **68**, 333–337.
127 Lutfullah, H. S. Dunsmore and R. Paterson, *J. Chem. Soc., Faraday Trans. 1*, 1976, **72**, 495–503.
128 Z. Cai, Y. Ou, J. Wang, R. Xiao, L. Fu, Z. Yuan, R. Zhan and Y. Sun, *Energy Storage Mater.*, 2020, **27**, 205–211.
129 J. Zhao, Z. Lv, S. Wang, Z. Chen, Z. Meng, G. Li, C. Guo, T. Liu and J. Hui, *Small Methods*, 2023, **7**, 2300731.
130 H. J. Kim, S. Kim, S. Kim, S. Kim, K. Heo, J. H. Lim, H. Yashiro, H. J. Shin, H. G. Jung, Y. M. Lee and S. T. Myung, *Adv. Mater.*, 2024, **36**, 2308592.
131 J. Xiao, *Science*, 2019, **366**, 426–427.
132 T. Foroozan, S. Sharifi-Asl and R. Shahbazian-Yassar, *J. Power Sources*, 2020, **461**, 228135.
133 Y. S. Hong, N. Li, H. Chen, P. Wang, W. L. Song and D. Fang, *Energy Storage Mater.*, 2018, **11**, 118–126.
134 B. Lee, E. Paek, D. Mitlin and S. W. Lee, *Chem. Rev.*, 2019, **119**, 5416–5460.
135 M. Tribbia, J. Glenneberg, G. Zampardi and F. La Mantia, *Batter. Supercaps*, 2022, **5**, e202100381.
136 Z. Zhao, P. Li, Z. Zhang, H. Zhang and G. Li, *Chem. Eng. J.*, 2023, **454**, 140435.
137 L. N. Bengoa, P. Pary, P. R. Seré, M. S. Conconi and W. A. Egli, *J. Mater. Eng. Perform.*, 2018, **27**, 1103–1108.
138 M. Zhang, H. Hua, P. Dai, Z. He, L. Han, P. Tang, J. Yang, P. Lin, Y. Zhang, D. Zhan, J. Chen, Y. Qiao, C. C. Li, J. Zhao and Y. Yang, *Adv. Mater.*, 2023, **35**, 2208630.
139 Y. Lyu, J. A. Yuwono, P. Wang, Y. Wang, F. Yang, S. Liu, S. Zhang, B. Wang, K. Davey, J. Mao and Z. Guo, *Angew. Chem., Int. Ed.*, 2023, **62**, e202303011.
140 K. Roy, A. Rana, J. N. Heil, B. M. Tackett and J. E. Dick, *Angew. Chem., Int. Ed.*, 2024, **63**, e202319010.
141 K. Roy, A. Rana, T. K. Ghosh, J. N. Heil, S. Roy, K. J. Vannoy, B. M. Tackett, M. Chen and J. E. Dick, *Adv. Energy Mater.*, 2024, **14**, 2303998.
142 H. Yang, Y. Yang, W. Yang, G. Wu and R. Zhu, *Energy Environ. Sci.*, 2024, **17**, 1975–1983.
143 H. Li, L. Yang, S. Zhou, J. Li, Y. Chen, X. Meng, D. Xu, C. Han, H. Duan and A. Pan, *Adv. Funct. Mater.*, 2024, **34**, 2313859.
144 K. Ouyang, S. Chen, W. Ling, M. Cui, Q. Ma, K. Zhang, P. Zhang and Y. Huang, *Angew. Chem.*, 2023, **135**, e202311988.
145 W. Zhang, Y. Dai, R. Chen, Z. Xu, J. Li, W. Zong, H. Li, Z. Li, Z. Zhang, J. Zhu, F. Guo, X. Gao, Z. Du, J. Chen, T. Wang, G. He and I. P. Parkin, *Angew. Chem., Int. Ed.*, 2023, **62**, e202212695.
146 F. Ming, Y. Zhu, G. Huang, A. H. Emwas, H. Liang, Y. Cui and H. N. Alshareef, *J. Am. Chem. Soc.*, 2022, **144**, 7160–7170.
147 L. Miao, R. Wang, S. Di, Z. Qian, L. Zhang, W. Xin, M. Liu, Z. Zhu, S. Chu, Y. Du and N. Zhang, *ACS Nano*, 2022, **16**, 9667–9678.
148 J. Zhao, Y. Li, X. Peng, S. Dong, J. Ma, G. Cui and L. Chen, *Electrochem. Commun.*, 2016, **69**, 6–10.
149 Z. Khan, D. Kumar and X. Crispin, *Adv. Mater.*, 2023, **35**, 2300369.
150 J. Wang, J. X. Tian, G. X. Liu, Z. Z. Shen and R. Wen, *Small Methods*, 2023, **7**, 2300392.
151 S. Watzele, J. Fichtner, B. Garlyyev, J. N. Schwämmlein and A. S. Bandarenka, *ACS Catal.*, 2018, **8**, 9456–9462.
152 S. Trasatti, *J. Electroanal. Chem. Interfacial Electrochem.*, 1972, **39**, 163–184.
153 Y. Kim, Y. Park, M. Kim, J. Lee, K. J. Kim and J. W. Choi, *Nat. Commun.*, 2022, **13**, 2371.
154 C. Liu, Z. Luo, W. Deng, W. Wei, L. Chen, A. Pan, J. Ma, C. Wang, L. Zhu, L. Xie, X. Y. Cao, J. Hu, G. Zou, H. Hou and X. Ji, *ACS Energy Lett.*, 2021, **6**, 675–683.
155 P. Ruan, X. Chen, L. Qin, Y. Tang, B. Lu, Z. Zeng, S. Liang and J. Zhou, *Adv. Mater.*, 2023, **35**, 2300577.
156 L. Wang, S. Zhou, K. Yang, W. Huang, S. Ogata, L. Gao and X. Pu, *Adv. Sci.*, 2024, **11**, 2307667.
157 J. Lai, H. Zhang, K. Xu and F. Shi, *J. Am. Chem. Soc.*, 2024, **146**, 22257–22265.
158 H. Zhao, Q. Fu, X. Luo, X. Wu, S. Indris, M. Bauer, Y. Wang, H. Ehrenberg, M. Knapp and Y. Wei, *Energy Storage Mater.*, 2022, **50**, 464–472.
159 Q. Zhang, Y. Ma, Y. Lu, Y. Ni, L. Lin, Z. Hao, Z. Yan, Q. Zhao and J. Chen, *J. Am. Chem. Soc.*, 2022, **144**, 18435–18443.
160 M. Fu, H. Yu, S. Huang, Q. Li, B. Qu, L. Zhou, G. C. Kuang, Y. Chen and L. Chen, *Nano Lett.*, 2023, **23**, 3573–3581.
161 X. Yu, M. Chen, Z. Li, X. Tan, H. Zhang, J. Wang, Y. Tang, J. Xu, W. Yin, Y. Yang, D. Chao, F. Wang, Y. Zou, G. Feng, Y. Qiao, H. Zhou and S. G. Sun, *J. Am. Chem. Soc.*, 2024, **146**, 17103–17113.
162 L. Ma, Q. Li, Y. Ying, F. Ma, S. Chen, Y. Li, H. Huang and C. Zhi, *Adv. Mater.*, 2021, **33**, 2007406.
163 J. Han, H. Euchner, M. Kuenzel, S. M. Hosseini, A. Groß, A. Varzi and S. Passerini, *ACS Energy Lett.*, 2021, **6**, 3063–3071.
164 M. Liu, W. Yuan, G. Ma, K. Qiu, X. Nie, Y. Liu, S. Shen and N. Zhang, *Angew. Chem.*, 2023, **135**, e202304444.
165 Y. Liu, Y. Li, X. Huang, H. Cao, Q. Zheng, Y. Huo, J. Zhao, D. Lin, B. Xu, Y. Liu, Y. Li, X. Huang, H. Cao, Q. Zheng, Y. Huo, D. Lin, J. Zhao and B. Xu, *Small*, 2022, **18**, 2203061.
166 Y. Tan, D. Chen, T. Yao, Y. Zhang, C. Miao, H. Yang, Y. Wang, L. Li, V. Kotsiubynskyi, W. Han and L. Shen, *Adv. Sci.*, 2024, **11**, 2407410.
167 Z. Cao, H. Zhang, B. Song, D. Xiong, S. Tao, W. Deng, J. Hu, H. Hou, G. Zou, X. Ji, Z. Cao, H. Zhang, D. Xiong, S. Tao,

W. Deng, J. Hu, H. Hou, G. Zou and X. Ji, *Adv. Funct. Mater.*, 2023, **33**, 2300339.
168 Y. Xiang, Y. Zhong, P. Tan, L. Zhou, G. Yin, H. Pan, X. Li, Y. Jiang, M. Xu and X. Zhang, *Small*, 2023, **19**, 2302161.
169 D. Lei, W. Shang, L. Cheng, W. Kaiser, P. Banerjee, S. Tu, O. Henrotte, J. Zhang, A. Gagliardi, J. Jinschek, E. Cortés, P. Müller-Buschbaum, A. S. Bandarenka, M. Z. Hussain and R. A. Fischer, *Adv. Energy Mater.*, 2024, **14**, 2403030.
170 B. Li, S. Liu, Y. Geng, C. Mao, L. Dai, L. Wang, S. C. Jun, B. Lu, Z. He and J. Zhou, *Adv. Funct. Mater.*, 2024, **34**, 2214033.
171 Y. He, R. Zhang, P. Zou, R. W. Chu, R. Lin, K. Xu and H. L. Xin, *J. Am. Chem. Soc.*, 2025, **147**, 6427–6438.
172 X. Cai, W. Tian, Z. Zhang, Y. Sun, L. Yang, H. Mu, C. Lian and H. Qiu, *Adv. Mater.*, 2024, **36**, 2307727.
173 G. Bergman, N. Bruchiel-Spanier, O. Bluman, N. Levi, S. Harpaz, F. Malchick, L. Wu, M. Sonoo, M. S. Chae, G. Wang, D. Mandler, D. Aurbach, Y. Zhang, N. Shpigel and D. Sharon, *J. Mater. Chem. A*, 2024, **12**, 14456–14466.
174 L. Cao, D. Li, E. Hu, J. Xu, T. Deng, L. Ma, Y. Wang, X. Q. Yang and C. Wang, *J. Am. Chem. Soc.*, 2020, **142**, 21404–21409.
175 G. Ma, L. Miao, Y. Dong, W. Yuan, X. Nie, S. Di, Y. Wang, L. Wang and N. Zhang, *Energy Storage Mater.*, 2022, **47**, 203–210.
176 D. Wang, R. Li, J. Dong, Z. Bai, N. Wang, S. X. Dou and J. Yang, *Angew. Chem., Int. Ed.*, 2025, **64**, e202414117.
177 Q. Ma, R. Gao, Y. Liu, H. Dou, Y. Zheng, T. Or, L. Yang, Q. Li, Q. Cu, R. Feng, Z. Zhang, Y. Nie, B. Ren, D. Luo, X. Wang, A. Yu and Z. Chen, *Adv. Mater.*, 2022, **34**, 2207344.
178 S. Yang, G. Wu, J. Zhang, Y. Guo, K. Xue, Y. Zhang, Y. Zhu, T. Li, X. Zhang and L. Zhou, *Adv. Sci.*, 2024, **11**, 2403513.
179 J. Wan, R. Wang, Z. Liu, L. Zhang, F. Liang, T. Zhou, S. Zhang, L. Zhang, Q. Lu, C. Zhang and Z. Guo, *ACS Nano*, 2023, **17**, 1610–1621.
180 I. Al Kathemi, Z. Slim, F. Igoa Saldaña, A. C. Dippel, P. Johansson, M. Odziomek and R. Bouchal, *ACS Nano*, 2025, **19**, 6388–6398.
181 D. Gomez Vazquez, T. P. Pollard, J. Mars, J. M. Yoo, H. G. Steinrück, S. E. Bone, O. V. Safonova, M. F. Toney, O. Borodin and M. R. Lukatskaya, *Energy Environ. Sci.*, 2023, **16**, 1982–1991.
182 R. Bouchal, I. Al Kathemi and M. Antonietti, *Small*, 2024, **20**, 2309556.
183 X. Yang, Q. Zhou, S. Wei, X. Guo, P. J. Chimtali, W. Xu, S. Chen, Y. Cao, P. Zhang, K. Zhu, H. Shou, Y. Wang, X. Wu, C. Wang and L. Song, *Small Methods*, 2024, **8**, 2301115.
184 F. Zhao, Z. Jing, X. Guo, J. Li, H. Dong, Y. Tan, L. Liu, Y. Zhou, R. Owen, P. R. Shearing, D. J. L. Brett, G. He and I. P. Parkin, *Energy Storage Mater.*, 2022, **53**, 638–645.
185 Y. Chen, F. Gong, W. Deng, H. Zhang and X. Wang, *Energy Storage Mater.*, 2023, **58**, 20–29.
186 X. Fan, L. Chen, Y. Wang, X. Xu, X. Jiao, P. Zhou, Y. Liu, Z. Song and J. Zhou, *Nanomicro Lett.*, 2024, **16**, 270.
187 H. Yang, D. Chen, R. Zhao, G. Li, H. Xu, L. Li, X. Liu, G. Li, D. Chao and W. Han, *Energy Environ. Sci.*, 2023, **16**, 2910–2923.
188 V. Vanoppen, L. Zhang, E. J. Berg and X. Hou, *ACS Mater. Lett.*, 2024, **6**, 4881–4888.
189 Q. Luo, K. Wang, D. Chen, K. Wang, Z. Sun, W. Xu, J. Li, Y. Wang, Q. Guo, J. Liao, Z. Deng, J. Hu and S. Xiong, *Adv. Energy Mater.*, 2025, 2405169.
190 T. A. Nigatu, H. K. Bezabh, S. K. Jiang, B. W. Taklu, Y. Nikodimos, S. C. Yang, S. H. Wu, W. N. Su, C. C. Yang and B. J. Hwang, *Electrochim. Acta*, 2023, **443**, 141883.
191 L. Cao, D. Li, T. Pollard, T. Deng, B. Zhang, C. Yang, L. Chen, J. Vatamanu, E. Hu, M. J. Hourwitz, L. Ma, M. Ding, Q. Li, S. Hou, K. Gaskell, J. T. Fourkas, X. Q. Yang, K. Xu, O. Borodin and C. Wang, *Nat. Nanotechnol.*, 2021, **16**, 902–910.
192 D. Xie, Y. Sang, D. H. Wang, W. Y. Diao, F. Y. Tao, C. Liu, J. W. Wang, H. Z. Sun, J. P. Zhang and X. L. Wu, *Angew. Chem., Int. Ed.*, 2023, **62**, e202216934.
193 L. Deng, X. Xie, W. Song, A. Pan, G. Cao, S. Liang and G. Fang, *Chem. Eng. J.*, 2024, **488**, 151104.
194 D. Aurbach and Y. Gofer, *J. Electrochem. Soc.*, 1991, **138**, 3529–3536.
195 L. Ma, M. A. Schroeder, O. Borodin, T. P. Pollard, M. S. Ding, C. Wang and K. Xu, *Nat. Energy*, 2020, **5**, 743–749.
196 Q. Pang, H. Zhao, R. Lian, Q. Fu, Y. Wei, A. Sarapulova, J. Sun, C. Wang, G. Chen and H. Ehrenberg, *J. Mater. Chem. A*, 2020, **8**, 9567–9578.
197 V. Renman, D. O. Ojwang, M. Valvo, C. P. Gómez, T. Gustafsson and G. Svensson, *J. Power Sources*, 2017, **369**, 146–153.
198 M. S. Chae, J. W. Heo, S. C. Lim and S. T. Hong, *Inorg. Chem.*, 2016, **55**, 3294–3301.
199 C. Pan, R. Zhang, R. G. Nuzzo and A. A. Gewirth, *Adv. Energy Mater.*, 2018, **8**, 1800589.
200 S. Zuo, J. Liu, W. He, S. Osman, Z. Liu, X. Xu, J. Shen, W. Jiang, J. Liu, Z. Zeng and M. Zhu, *J. Phys. Chem. Lett.*, 2021, **12**, 7076–7084.
201 X. Shan, S. Kim, A. M. M. Abeykoon, G. Kwon, D. Olds and X. Teng, *ACS Appl. Mater. Interfaces*, 2020, **12**, 54627–54636.
202 F. Wang, L. E. Blanc, Q. Li, A. Faraone, X. Ji, H. H. Chen-Mayer, R. L. Paul, J. A. Dura, E. Hu, K. Xu, L. F. Nazar and C. Wang, *Adv. Energy Mater.*, 2021, **11**, 2102016.
203 L. Wang, K.-W. Huang, J. Chen and J. Zheng, *Sci. Adv.*, 2019, **5**, eaax4279.
204 M. D. Chung, J. H. Seo, X. C. Zhang and A. M. Sastry, *J. Electrochem. Soc.*, 2011, **158**, A371.
205 M. A. Kamenskii, S. N. Eliseeva, E. G. Tolstopjatova, A. I. Volkov, D. V. Zhuzhelskii and V. V. Kondratiev, *Electrochim. Acta*, 2019, **326**, 134969.
206 S. Takai, K. Yoshioka, H. Iikura, M. Matsubayashi, T. Yao and T. Esaka, *Solid. State Ion.*, 2014, **256**, 93–96.
207 S. B. Tang, M. O. Lai and L. Lu, *Mater. Chem. Phys.*, 2008, **111**, 149–153.
208 E. Andrukaitis and I. Hill, *J. Power Sources*, 2004, **136**, 290–295.
209 N. Kuwata, M. Nakane, T. Miyazaki, K. Mitsuishi and J. Kawamura, *Solid State Ion.*, 2018, **320**, 266–271.

210 G. Hasegawa, N. Kuwata, Y. Tanaka, T. Miyazaki, N. Ishigaki, K. Takada and J. Kawamura, *Phys. Chem. Chem. Phys.*, 2021, **23**, 2438–2448.
211 P. M. Panchmatia, A. R. Armstrong, P. G. Bruce and M. S. Islam, *Phys. Chem. Chem. Phys.*, 2014, **16**, 21114–21118.
212 F. D. A. Silva, F. Huguenin, S. M. De Lima and G. J. F. Demets, *Inorg. Chem. Front.*, 2014, **1**, 495–502.
213 E. Potiron, A. Le Gal La Salle, A. Verbaere, Y. Piffard and D. Guyomard, *Electrochim. Acta*, 1999, **45**, 197–214.
214 J. Xie, K. Kohno, T. Matsumura, N. Imanishi, A. Hirano, Y. Takeda and O. Yamamoto, *Electrochim. Acta*, 2008, **54**, 376–381.
215 N. Zhang, F. Cheng, Y. Liu, Q. Zhao, K. Lei, C. Chen, X. Liu and J. Chen, *J. Am. Chem. Soc.*, 2016, **138**, 12894–12901.
216 R. Si, S. Yi, H. Liu, F. Yu, W. Bao, C. Guo and J. Li, *Chem. – Eur. J.*, 2023, **29**, e202300409.
217 C. Morando, P. Cofrancesco and C. Tealdi, *Mater. Today Commun.*, 2020, **25**, 101478.
218 X. Yao, C. Li, R. Xiao, J. Li, H. Yang, J. Deng and M. S. Balogun, *Small*, 2022, **18**, 2204534.
219 S. Li, Y. Liu, X. Zhao, Q. Shen, W. Zhao, Q. Tan, N. Zhang, P. Li, L. Jiao, X. S. Qu Li, Y. Liu, X. Zhao, Q. Shen, W. Zhao, Q. Tan, P. Li, X. Qu, N. Zhang and L. Jiao, *Adv. Mater.*, 2021, **33**, 2007480.
220 Z. Wu, C. Lu, F. Ye, L. Zhang, L. Jiang, Q. Liu, H. Dong, Z. Sun and L. Hu, *Adv. Funct. Mater.*, 2021, **31**, 2106816.
221 L. Hu, Z. Wu, C. Lu, F. Ye, Q. Liu and Z. Sun, *Energy Environ. Sci.*, 2021, **14**, 4095–4106.
222 M. Z. A. Munshi, W. H. Smyrl and C. Schmidtke, *Solid State Ion.*, 1991, **47**, 265–270.
223 J. Lai, H. Zhu, X. Zhu, H. Koritala and Y. Wang, *ACS Appl. Energy Mater.*, 2019, **2**, 1988–1996.
224 W. Shi, B. Yin, Y. Yang, M. B. Sullivan, J. Wang, Y. W. Zhang, Z. G. Yu, W. S. V. Lee and J. Xue, *ACS Nano*, 2021, **15**, 1273–1281.
225 W. Liang, D. Rao, T. Chen, R. Tang, J. Li and H. Jin, *Angew. Chem., Int. Ed.*, 2022, **61**, e202207779.
226 F. Ming, H. Liang, Y. Lei, S. Kandambeth, M. Eddaoudi and H. N. Alshareef, *ACS Energy Lett.*, 2018, **3**, 2602–2609.
227 N. Zhang, Y. Dong, M. Jia, X. Bian, Y. Wang, M. Qiu, J. Xu, Y. Liu, L. Jiao and F. Cheng, *ACS Energy Lett.*, 2018, **3**, 1366–1372.
228 S. Deng, Z. Yuan, Z. Tie, C. Wang, L. Song and Z. Niu, *Angew. Chem., Int. Ed.*, 2020, **59**, 22002–22006.
229 J. Zheng, C. Liu, M. Tian, X. Jia, E. P. Jahrman, G. T. Seidler, S. Zhang, Y. Liu, Y. Zhang, C. Meng and G. Cao, *Nano Energy*, 2020, **70**, 104519.
230 G. Yoo, B. R. Koo and G. H. An, *Chem. Eng. J.*, 2022, **434**, 134738.
231 J. Chen, B. Xiao, C. Hu, H. Chen, J. Huang, D. Yan and S. Peng, *ACS Appl. Mater. Interfaces*, 2022, **14**, 28760–28768.
232 C. Xia, J. Guo, P. E. Li, X. Zhang, N. Husam Alshareef, C. Xia, J. Guo, D. Li, X. X. Zhang and H. N. Alshareef, *Angew. Chem.*, 2018, **130**, 4007–4012.
233 L. F. Zhou, X. W. Gao, T. Du, H. Gong, L. Y. Liu and W. Bin Luo, *J. Alloys Compd.*, 2022, **905**, 163939.
234 F. Gao, B. Mei, X. Xu, J. Ren, D. Zhao, Z. Zhang, Z. Wang, Y. Wu, X. Liu and Y. Zhang, *Chem. Eng. J.*, 2022, **448**, 137742.
235 L. Zhang, L. Miao, B. Zhang, J. Wang, J. Liu, Q. Tan, H. Wan and J. Jiang, *J. Mater. Chem. A*, 2020, **8**, 1731–1740.
236 S. H. Hwang, S. D. Seo and D. W. Kim, *J. Mater. Chem. A*, 2022, **10**, 10638–10650.
237 Y. Cheng, L. Luo, L. Zhong, J. Chen, B. Li, W. Wang, S. X. Mao, C. Wang, V. L. Sprenkle, G. Li and J. Liu, *ACS Appl. Mater. Interfaces*, 2016, **8**, 13673–13677.
238 L. Zhang, L. Chen, X. Zhou and Z. Liu, *Sci. Rep.*, 2015, **5**, 18263.
239 G. Zampardi and F. L. Mantia, *Curr. Opin. Electrochem.*, 2020, **21**, 84–92.
240 Y. Xue, X. Shen, H. Zhou, J. Cao, J. Pu, Z. Ji, L. Kong and A. Yuan, *Chem. Eng. J.*, 2022, **448**, 137657.
241 Y. Zhang, Y. Wang, L. Lu, C. Sun and D. Y. W. Yu, *J. Power Sources*, 2021, **484**, 229263.
242 G. Ni, X. Xu, Z. Hao, W. Wang, C. Li, Y. Yang, C. Zhou, L. Qin, W. Chen, X. Yao and J. Cai, *ACS Appl. Energy Mater.*, 2021, **4**, 602–610.
243 L. Zhang, L. Chen, X. Zhou and Z. Liu, *Adv. Energy Mater.*, 2015, **5**, 1400930.
244 X. Li, Z. Chen, Y. Yang, S. Liang, B. Lu and J. Zhou, *Inorg. Chem. Front.*, 2022, **9**, 3986–3998.
245 F. Wang, E. Hu, W. Sun, T. Gao, X. Ji, X. Fan, F. Han, X. Q. Yang, K. Xu and C. Wang, *Energy Environ. Sci.*, 2018, **11**, 3168–3175.
246 L. F. Zhou, X. W. Gao, T. Du, H. Gong, L. Y. Liu and W. Bin Luo, *ACS Appl. Mater. Interfaces*, 2022, **14**, 8888–8895.
247 W. Li, X. Jing, K. Jiang and D. Wang, *ACS Appl. Energy Mater.*, 2021, **4**, 2797–2807.
248 N. Wang, C. Sun, X. Liao, Y. Yuan, H. Cheng, Q. Sun, B. Wang, X. Pan, K. Zhao, Q. Xu, X. Lu, J. Lu, N. Wang, H. Cheng, Q. Sun, K. Zhao, Q. Xu, X. Lu, C. Sun, X. Liao, X. Pan, Y. Yuan, J. Lu and B. Wang, *Adv. Energy Mater.*, 2020, **10**, 2002293.
249 G. Shi, P. Zhao, P. Gao, Y. Xing and B. Shen, *J. Energy Storage*, 2024, **78**, 110057.
250 M. Tian, C. Liu, J. Zheng, X. Jia, E. P. Jahrman, G. T. Seidler, D. Long, M. Atif, M. Alsalhi and G. Cao, *Energy Storage Mater.*, 2020, **29**, 9–16.
251 T. Lv, G. Zhu, S. Dong, Q. Kong, Y. Peng, S. Jiang, G. Zhang, Z. Yang, S. Yang, X. Dong, H. Pang and Y. Zhang, *Angew. Chem., Int. Ed.*, 2023, **62**, e202216089.
252 Y. Tong, X. Li, S. Su, J. Li, J. Fang, B. Liang, J. Hou and M. Luo, *J. Colloid Interface Sci.*, 2022, **606**, 645–653.
253 F. Zhang, X. Sun, M. Du, X. Zhang, W. Dong, Y. Sang, J. Wang, Y. Li, H. Liu and S. Wang, *Energy Environ. Mater.*, 2021, **4**, 620–630.
254 Q. Zong, Y. Zhuang, C. Liu, Q. Kang, Y. Wu, J. Zhang, J. Wang, D. Tao, Q. Zhang and G. Cao, *Adv. Energy Mater.*, 2023, **13**, 2301480.
255 S. Chen, K. Li, K. S. Hui and J. Zhang, *Adv. Funct. Mater.*, 2020, **30**, 2003890.
256 M. Huang, Y. Mai, L. Zhao, X. Liang, Z. Fang and X. Jie, *Electrochim. Acta*, 2021, **388**, 138624.

257 H. Shuai, R. Liu, W. Li, X. Yang, H. Lu, Y. Gao, J. Xu and K. Huang, *Adv. Energy Mater.*, 2023, **13**, 2202992.
258 S. Li, Y. Liu, X. Zhao, K. Cui, Q. Shen, P. Li, X. Qu and L. Jiao, *Angew. Chem., Int. Ed.*, 2021, **60**, 20286–20293.
259 S. Li, C. Huang, L. Gao, Q. Shen, P. Li, X. Qu, L. Jiao and Y. Liu, *Angew. Chem., Int. Ed.*, 2022, **61**, e202211478.
260 H. Liu, J. G. Wang, W. Hua, Z. You, Z. Hou, J. Yang, C. Wei and F. Kang, *Energy Storage Mater.*, 2021, **35**, 731–738.
261 W. Liu, L. Dong, B. Jiang, Y. Huang, X. Wang, C. Xu, Z. Kang, J. Mou and F. Kang, *Electrochim. Acta*, 2019, **320**, 134565.
262 H. Yan, C. Yang, L. Zhao, J. Liu, P. Zhang and L. Gao, *Electrochim. Acta*, 2022, **429**, 141003.
263 H. Huang, X. Xia, J. Yun, C. Huang, D. Li, B. Chen, Z. Yang and W. Zhang, *Energy Storage Mater.*, 2022, **52**, 473–484.
264 F. Gong, Y. Feng, Y. H. Fang, Y. K. Hsu and Y. C. Chen, *ACS Appl. Mater. Interfaces*, 2022, **15**, 18808–18818.
265 S. W. Kim, X. Shan, M. Abeykoon, G. Kwon, D. Olds and X. Teng, *ACS Appl. Mater. Interfaces*, 2021, **13**, 25993–26000.
266 Q. Ni, H. Jiang, S. Sandstrom, Y. Bai, H. Ren, X. Wu, Q. Guo, D. Yu, C. Wu and X. Ji, *Adv. Funct. Mater.*, 2020, **30**, 2003511.
267 M. J. Park, H. Y. Asl and A. Manthiram, *Adv. Mater. Interfaces*, 2021, **8**, 2100878.
268 K. Malaie, F. Scholz, U. Schröder, H. Wulff and H. Kahlert, *Chem. Phys. Chem.*, 2022, **23**, e202200364.
269 L. Zhou, L. Liu, Z. Hao, Z. Yan, X. F. Yu, P. K. Chu, K. Zhang and J. Chen, *Matter*, 2021, **4**, 1252–1273.
270 C. F. Bischoff, O. S. Fitz, J. Burns, M. Bauer, H. Gentischer, K. P. Birke, H.-M. Henning and D. Biro, *J. Electrochem. Soc.*, 2020, **167**, 020545.
271 O. Fitz, F. Wagner, J. Pross-Brakhage, M. Bauer, H. Gentischer, K. P. Birke and D. Biro, *Energy Technol.*, 2023, **11**, 2300723.
272 C. Li, X. Yun, Y. Chen, D. Lu, Z. Ma, S. Bai, G. Zhou, P. Xiao and C. Zheng, *Chem. Eng. J.*, 2023, **477**, 146901.
273 M. Chen, M. Yang, X. Han, J. Chen, P. Zhang and C. P. Wong, *Adv. Mater.*, 2024, **36**, 2304997.
274 O. Kokits, Y. Aniskevich, A. Mazanik, O. Yakimenko, G. Ragoisha, S. T. Myung and E. Streltsov, *Energy Storage Mater.*, 2023, **63**, 103017.
275 S. Sariyer, N. M. Keppetipola, O. Sel and R. Demir-Cakan, *ChemSusChem*, 2025, e202402445.
276 I. A. Rodríguez-Pérez, H. J. Chang, M. Fayette, B. M. Sivakumar, D. Choi, X. Li and D. Reed, *J. Mater. Chem. A*, 2021, **9**, 20766–20775.
277 C. Wang, J. Wang, S. Zhang, M. Li, F. Zeng, L. Tan, F. Liu, J. Wang, L. Huang, H. Lv, C. Zhi and C. Han, *Adv. Energy Mater.*, 2023, **13**, 2302683.
278 Q. Guo, W. Li, X. Li, J. Zhang, D. Sabaghi, J. Zhang, B. Zhang, D. Li, J. Du, X. Chu, S. Chung, K. Cho, N. N. Nguyen, Z. Liao, Z. Zhang, X. Zhang, G. F. Schneider, T. Heine, M. Yu and X. Feng, *Nat. Commun.*, 2024, **15**, 2139.
279 A. O. Efremova, A. I. Volkov, E. G. Tolstopyatova and V. V. Kondratiev, *J. Alloys Compd.*, 2022, **892**, 162142.
280 L. Y. Wu, Z. W. Li, Y. X. Xiang, W. Di Dong, X. D. Qi, Z. X. Ling, Y. H. Xu, H. Y. Wu, M. D. Levi, N. Shpigel and X. G. Zhang, *Small*, 2024, **20**, 2404583.
281 L. Y. Wu, Z. W. Li, Y. X. Xiang, W. Di Dong, H. Y. Wu, Y. H. Xu, Z. X. Ling, M. S. Chae, D. Sharon, N. Shpigel and X. G. Zhang, *ACS Energy Lett.*, 2024, **9**, 5801–5809.
282 Y. Xu, G. Zhang, X. Wang, X. Li, J. Zhang, X. Wu, Y. Yuan, Y. Xi, X. Yang, M. Li, X. Pu, G. Cao, Z. Yang, B. Sun, J. Wang, H. Yang, W. Li, J. Zhang and X. Li, *J. Colloid Interface Sci.*, 2024, **675**, 1–13.
283 B. Gavriel, N. Shpigel, F. Malchik, G. Bergman, M. Turgeman, M. D. Levi and D. Aurbach, *Energy Storage Mater.*, 2021, **38**, 535–541.
284 M. Chen, M. Zhou, Q. Wang, C. Xu, S. Wang, J. Ning, T. Wang, K. Wang and K. Jiang, *Adv. Funct. Mater.*, 2025, **35**, 2414032.
285 M. Chen, X. He, M. Zhou, J. Ning, Z. Zhang, S. Cao, T. Wang, K. Wang and K. Jiang, *Adv. Energy Mater.*, 2024, **14**, 2400724.
286 H. Cui, J. Zhu, R. Zhang, S. Yang, C. Li, Y. Wang, Y. Hou, Q. Li, G. Liang and C. Zhi, *J. Am. Chem. Soc.*, 2024, **146**, 15393–15402.
287 S. Yeşilot, Y. Solmaz, N. Kılıç, B. Unal, O. Sel and R. Demir-Cakan, *ChemElectroChem*, 2024, **11**, e202400212.
288 Y. Zhang, Y. Liang, H. Dong, X. Wang and Y. Yao, *J. Electrochem. Soc.*, 2020, **167**, 070558.
289 G. Inzelt, *Electrochim. Acta*, 2000, **45**, 3865–3876.
290 M. D. Levi, N. Shpigel, S. Sigalov, V. Dargel, L. Daikhin and D. Aurbach, *Electrochim. Acta*, 2017, **232**, 271–284.
291 N. Shpigel, M. D. Levi and D. Aurbach, *Energy Storage Mater.*, 2019, **21**, 399–413.
292 T. B. Reddy, *Linden's Handbook of Batteries*, McGraw-Hill Education, 4th edn, 2011.
293 K. Kordesh and M. Weissenbacher, *J. Power Sources*, 1994, **51**, 61–78.
294 H. Li, H. Yao, X. Sun, C. Sheng, W. Zhao, J. Wu, S. Chu, Z. Liu, S. Guo and H. Zhou, *Chem. Eng. J.*, 2022, **446**, 137205.
295 Y. Huang, J. Mou, W. Liu, X. Wang, L. Dong, F. Kang and C. Xu, *Nanomicro Lett.*, 2019, **11**, 49.
296 Z. Li, Y. Li, X. Ren, Y. Zhao, Z. Ren, Z. Yao, W. Zhang, H. Xu, Z. Wang, N. Zhang, Y. Gu, X. Li, D. Zhu and J. Zou, *Small*, 2023, **19**, 2301770.
297 L. Chen, Z. Yang, H. Qin, X. Zeng and J. Meng, *J. Power Sources*, 2019, **425**, 162–169.
298 S. Zhao, B. Han, D. Zhang, Q. Huang, L. Xiao, L. Chen, D. G. Ivey, Y. Deng and W. Wei, *J. Mater. Chem. A*, 2018, **6**, 5733–5739.
299 X. Guo, J. Zhou, C. Bai, X. Li, G. Fang and S. Liang, *Mater. Today Energy*, 2020, **16**, 100396.
300 O. Fitz, C. Bischoff, M. Bauer, H. Gentischer, K. P. Birke, H. M. Henning and D. Biro, *ChemElectroChem*, 2021, **8**, 3553–3566.
301 W. Sun, F. Wang, S. Hou, C. Yang, X. Fan, Z. Ma, T. Gao, F. Han, R. Hu, M. Zhu and C. Wang, *J. Am. Chem. Soc.*, 2017, **139**, 9775–9778.
302 O. Rubel, T. N. T. Tran, S. Gourley, S. Anand, A. Van Bommel, B. D. Adams, D. G. Ivey and D. Higgins, *J. Phys. Chem. C*, 2022, **126**, 10957–10967.

303 T. N. T. Tran, S. Jin, M. Cuisinier, B. D. Adams and D. G. Ivey, *Sci. Rep.*, 2021, **11**, 20777.
304 D. Wu, S. T. King, N. Sadique, L. Ma, S. N. Ehrlich, S. Ghose, J. Bai, H. Zhong, S. Yan, D. C. Bock, E. S. Takeuchi, A. C. Marschilok, L. M. Housel, L. Wang and K. J. Takeuchi, *J. Mater. Chem. A*, 2023, **11**, 16279–16292.
305 O. Zhanadilov, H. J. Kim, A. Konarov, J. Jeong, J. H. Park, K. Y. Chung, Z. Bakenov, H. Yashiro and S. T. Myung, *Energy Storage Mater.*, 2024, **67**, 103283.
306 S. Islam, M. H. Alfaruqi, V. Mathew, J. Song, S. Kim, S. Kim, J. Jo, J. P. Baboo, D. T. Pham, D. Y. Putro, Y. K. Sun and J. Kim, *J. Mater. Chem. A*, 2017, **5**, 23299–23309.
307 N. Zhang, F. Cheng, J. Liu, L. Wang, X. Long, X. Liu, F. Li and J. Chen, *Nat. Commun.*, 2017, **8**, 405.
308 D. Y. Putro, M. H. Alfaruqi, S. Islam, S. Kim, S. Park, S. Lee, J. Y. Hwang, Y. K. Sun and J. Kim, *Electrochim. Acta*, 2020, **345**, 136189.
309 S. Cui, D. Zhang, G. Zhang and Y. Gan, *J. Mater. Chem. A*, 2022, **10**, 25620–25632.
310 S. Cui, D. Zhang and Y. Gan, *Adv. Energy Mater.*, 2024, **14**, 2302655.
311 H. Chen, C. Dai, F. Xiao, Q. Yang, S. Cai, M. Xu, H. J. Fan, S.-J. Bao, H. Chen, F. Xiao, Q. Yang, S. Cai, M. Xu, S.-J. Bao, C. Dai and H. J. Fan, *Adv. Mater.*, 2022, **34**, 2109092.
312 B. Wu, G. Zhang, M. Yan, T. Xiong, P. He, L. He, X. Xu and L. Mai, *Small*, 2018, **14**, 1703850.
313 H. Yang, W. Zhou, D. Chen, J. Liu, Z. Yuan, M. Lu, L. Shen, V. Shulga, W. Han and D. Chao, *Energy Environ. Sci.*, 2021, **15**, 1106–1118.
314 H. Yang, T. Zhang, D. Chen, Y. Tan, W. Zhou, L. Li, W. Li, G. Li, W. Han, H. J. Fan, D. Chao, H. Yang, D. Chen, Y. Tan, L. Li, G. Li, W. Han, T. Zhang, W. Zhou, W. Li, D. Chao and H. J. Fan, *Adv. Mater.*, 2023, **35**, 2300053.
315 Y. Du, X. Wang, Y. Zhang, H. Zhang, J. Man, K. Liu and J. Sun, *Chem. Eng. J.*, 2022, **434**, 134642.
316 T. H. Wu, K. Y. Ni, B. T. Liu and S. H. Wang, *ACS Appl. Energy Mater.*, 2022, **5**, 10196–10206.
317 K. Zhu, T. Wu and K. Huang, *Chem. Mater.*, 2021, **33**, 4089–4098.
318 Y. Bo Hu, Y. Min Zhang, N. Nan XUE, P. Cheng Hu and L. Hong Zhang, *Trans. Nonferrous Met. Soc. China*, 2022, **32**, 1290–1300.
319 I. Povar, O. Spinu, I. Zinicovscaia, B. Pintilie and S. Ubaldini, *J. Electrochem. Sci. Eng.*, 2019, **9**, 75–84.
320 Y. Liu, Y. Jiang, Z. Hu, J. Peng, W. Lai, D. Wu, S. Zuo, J. Zhang, B. Chen, Z. Dai, Y. Yang, Y. Huang, W. Zhang, W. Zhao, W. Zhang, L. Wang and S. Chou, *Adv. Funct. Mater.*, 2021, **31**, 2008033.
321 X. Li, M. Li, Q. Yang, H. Li, H. Xu, Z. Chai, K. Chen, Z. Liu, Z. Tang, L. Ma, Z. Huang, B. Dong, X. Yin, Q. Huang and C. Zhi, *ACS Nano*, 2020, **14**, 541–551.
322 S. Gao, P. Ju, Z. Liu, L. Zhai, W. Liu, X. Zhang, Y. Zhou, C. Dong, F. Jiang and J. Sun, *J. Energy Chem.*, 2022, **69**, 356–362.
323 K. Zhu, T. Wu and K. Huang, *Energy Storage Mater.*, 2021, **38**, 473–481.
324 Z. Wang, Y. Song, J. Wang, Y. Lin, J. Meng, W. Cui and X. X. Liu, *Angew. Chem., Int. Ed.*, 2023, **62**, e202216290.
325 S. Shen, D. Ma, K. Ouyang, Y. Chen, M. Yang, Y. Wang, S. Sun, H. Mi, L. Sun, C. He and P. Zhang, *Adv. Funct. Mater.*, 2023, **33**, 2304255.
326 S. Xu, S. Fan, W. Ma, J. Fan and G. Li, *Inorg. Chem. Front.*, 2022, **9**, 1481–1489.
327 J. Li, Q. Kuang, G. Wang, Q. Lu, P. Jiang, Q. Fan, Y. Dong and Y. Zhao, *Electrochim. Acta*, 2023, **441**, 141841.
328 Y. Zeng, Z. Lai, Y. Han, H. Zhang, S. Xie, X. Lu, Y. X. Zeng, Z. Z. Lai, Y. Han, H. Z. Zhang, X. H. Lu and S. L. Xie, *Adv. Mater.*, 2018, **30**, 1802396.
329 M. Yin, H. Miao, J. Dang, B. Chen, J. Zou, G. Chen and H. Li, *J. Power Sources*, 2022, **545**, 231902.
330 Y. Tang, X. Li, H. Lv, D. Xie, W. Wang, C. Zhi and H. Li, *Adv. Energy Mater.*, 2020, **10**, 2000892.
331 Y. Zuo, T. Meng, H. Tian, L. Ling, H. Zhang, H. Zhang, X. Sun and S. Cai, *ACS Nano*, 2023, **17**, 5600–5608.
332 G. Ni, Z. Hao, G. Zou, X. Xu, B. Hu, F. Cao and C. Zhou, Sustain, *Energy Fuels*, 2022, **6**, 1353–1361.
333 J. Chivot, L. Mendoza, C. Mansour, T. Pauporté and M. Cassir, *Corros. Sci.*, 2008, **50**, 62–69.
334 L. F. Huang, M. J. Hutchison, R. J. Santucci, J. R. Scully and J. M. Rondinelli, *J. Phys. Chem. C*, 2017, **121**, 9782–9789.
335 J. He, X. Shi, Q. Liu, H. Wu, Y. Yu, X. Lu and Z. Yang, *Small*, 2024, **20**, 2306258.
336 T. Fu, X. Tong, Y. Zhou, D. Wu, D. Xiong, S. Xu, L. Wang and P. K. Chu, *J. Alloys Compd.*, 2022, **918**, 165734.
337 W. Kao-ian, M. T. Nguyen, T. Yonezawa, R. Pornprasertsuk, J. Qin, S. Siwamogsatham and S. Kheawhom, *Mater. Today Energy*, 2021, **21**, 100738.
338 Q. Li, K. Ma, G. Yang and C. Wang, *Energy Storage Mater.*, 2020, **29**, 246–253.
339 A. Bhatia, J. Xu, J. P. Pereira-Ramos, G. Rousse and R. Baddour-Hadjean, *Chem. Mater.*, 2022, **34**, 1203–1212.
340 M. S. Chae, J. W. Heo, H. H. Kwak, H. Lee and S. T. Hong, *J. Power Sources*, 2017, **337**, 204–211.
341 R. D. Corpuz, L. M. De Juan-Corpuz, M. T. Nguyen, T. Yonezawa, H. L. Wu, A. Somwangthanaroj and S. Kheawhom, *Int. J. Mol. Sci.*, 2020, **21**, 3113.
342 V. Verma, S. Kumar, W. Manalastas, J. Zhao, R. Chua, S. Meng, P. Kidkhunthod and M. Srinivasan, *ACS Appl. Energy Mater.*, 2019, **2**, 8667–8674.
343 T. Yimtrakarn, Y. C. Liao, A. S. MV, J. L. Chen, Y. C. Chuang, N. Lerkkasemsan and W. Kaveevivitchai, *Mater. Today Commun.*, 2023, **34**, 105231.
344 A. Naveed, H. Yang, Y. Shao, J. Yang, N. Yanna, J. Liu, S. Shi, L. Zhang, A. Ye, B. He and J. Wang, *Adv. Mater.*, 2019, **31**, 1900668.
345 R. Zhang, C. Pan, R. G. Nuzzo and A. A. Gewirth, *J. Phys. Chem. C*, 2019, **123**, 8740–8745.
346 W. Wang, D. Liu, Y. Jiang, D. Zhang, X. Shen, S. Li, J. Liang and H. Xu, *Chem. Eng. J.*, 2023, **463**, 142309.
347 D. Wang, L. Wang, G. Liang, H. Li, Z. Liu, Z. Tang, J. Liang and C. Zhi, *ACS Nano*, 2019, **13**, 10643–10652.

348 W. Li, C. Xu, X. Zhang, M. Xia, Z. Yang, H. Yan, H. Yu, L. Zhang, W. Shu and J. Shu, *J. Electroanal. Chem.*, 2021, **881**, 114968.
349 Y. Xue, Y. Chen, X. Shen, A. Zhong, Z. Ji, J. Cheng, L. Kong and A. Yuan, *J. Colloid Interface Sci.*, 2022, **609**, 297–306.
350 Z. Li, T. Liu, R. Meng, L. Gao, Y. Zou, P. Peng, Y. Shao and X. Liang, *Energy Environ. Mater.*, 2021, **4**, 111–116.
351 H. Sun, L. Yang, E. Hu, M. Feng, C. Fan, W. Wang, H. Li, X. Wang and Z. Liu, *ACS Appl. Mater. Interfaces*, 2022, **14**, 40247–40256.
352 P. He, M. Yan, G. Zhang, R. Sun, L. Chen, Q. An and L. Mai, *Adv. Energy Mater.*, 2017, **7**, 1601920.
353 L. Ma, S. Chen, C. Long, X. Li, Y. Zhao, Z. Liu, Z. Huang, B. Dong, J. Antonio Zapien and C. Zhi, *Adv. Energy Mater.*, 2019, **9**, 1902446.
354 W. Yang, Y. Yang, H. Yang and H. Zhou, *ACS Energy Lett.*, 2022, **7**, 2515–2530.
355 T. F. Burton, R. Jommongkol, Y. Zhu, S. Deebansok, K. Chitbankluai, J. Deng and O. Fontaine, *Curr. Opin. Electrochem.*, 2022, **35**, 101070.

